Transformation Optics and Metamaterials

The Relativity of Electromagnetic Reality

Vincent Ginis

Transformation Optics and Metamaterials

The Relativity of Electromagnetic Reality

Proefschrift ingediend tot het behalen van de academische graad van
Master in de Ingenieurswetenschappen: Fotonica

by

Vincent Ginis

Promotor: Prof. Dr. Irina Veretennicoff

Advisor: Dr. Ir. Philippe Tassin

Vrije Universiteit Brussel—2 June 2009

Transformation Optics and Metamaterials: The Relativity of Electromagnetic Reality
Vincent Ginis
Vrije Universiteit Brussel, Faculteit Ingenieurswetenschappen

To my grandmother, meterke

Preface

Ironically, the first words that you are reading, are the last ones that I am writing down. These words therefore terminate the work of an entire year, in which I have not regretted a single day my choice to work on transformation optics. Without any doubt, this is the merit of several people that supported and encouraged me in this process. I have thought about this section several times this last year, very well realising how difficult it would be to express my gratitude in just a few sentences. Without any hope of completeness, I will hereby give it a try.

It would not feel right to start with anyone else than my promotor, Irina Veretennicoff, who supported me far beyond the scope of the academical purposes. She knows how to capture the essence of things in an extremely elucidating way. Irina, you are truly the most inspiring person I have ever met.

I could not have dreamt a better supervisor than Philippe Tassin, a true perfectionist. Whenever your calculations get the label "Philippe Tassin approved", chances are great you have not made any error. Philippe, we actively demonstrated the absolute relativity of space and time during the late Skype meetings while you were in Crete. I sincerely hope that we can continue to do this in the future.

I am also indebted to Ben Craps for introducing me to the world of general relativity and for helping me out during my first steps in transformation optics. The same applies for Jan Danckaert and Guy Van der Sande, who were always willing to help me. This brings me to Christof Debaes, who I would like to thank for his very fast interventions whenever I encountered software problems.

I am also very grateful to the members of my jury for having accepted to judge my master thesis.

This work does not only complete the last year of research, it also symbolises the end of five year academic education at the Vrije Universiteit Brussel. Therefore, this seems a good opportunity to thank everyone who contributed in this wonderful experience. The professors, the assistants and the administration for developing a critical spirit in an open-minded environment. But of

iv

Summary

Transformation optics provides a new way of looking at the interaction between light and matter. This recently developed method in electromagnetism is based on the analogy between the macroscopic Maxwell's equations in complex dielectrics and the free-space Maxwell's equations on the background of an arbitrary metric. The implementation of these complex dielectrics requires the use of metamaterials. In this work, we adopt the techniques of transformation optics in order to design two novel optical devices.

First, we use transformation optics for the implementation of optical cavities. Traditionally, optical microcavities are restricted in size due to the wavelike nature of light. This makes it impossible to confine light in a volume whose dimensions are smaller than the wavelength of light. Using transformation optics, we derive four designs for an optical cavity. The first two—a traditional invisibility cloak and a hyperbolic map—do not exhibit subwavelength modes. The third design offers a continuum of subwavelength modes, but is extremely sensitive to material perturbations. In the last design, we eliminate this sensitivity while keeping some of the subwavelength modes. The latter two devices, which are partially made with left-handed materials, have deep subwavelength modes.

The second component that we address is a frequency tuning device. Nowadays, it is quite difficult to achieve accurate frequency shifting of electromagnetic energy. Moreover, this process often generates unwanted sidebands. Therefore, we implement the mechanism of the biggest frequency shifter that exists: the universe. As light is travelling from one place to another in the outer space, the frequency of a photon is changing, since it is subjected to gravitational and cosmological redshifts. We calculate the material properties required to implement these redshifts with dielectrics and propose a frequency shifter based on an analogy to the cosmological redshift. We show that this device, which needs a time-dependent index of refraction, is a perfect frequency shifter.

Samenvatting

Transformatieoptica biedt een nieuwe kijk op de interactie tussen licht en materie. Deze recent ontwikkelde theorie is gebaseerd op de analogie tussen de macroscopische maxwellvergelijkingen in complexe diëlektrica en de maxwellvergelijkingen in de lege ruimte op de achtergrond van een willekeurige metriek. De implementatie van deze diëlektrica vereist het gebruik van metamaterialen. In dit werk wenden we de technieken van transformatieoptica aan om twee nieuwe optische componenten te ontwerpen.

Eerst passen we transformatieoptica toe op de implementatie van optische caviteiten. Traditionele caviteiten zijn steeds beperkt in grootte door het golfkarakter van het licht. Dit fenomeen maakt het onmogelijk om licht op te slaan in een volume met een karakteristieke lengte die kleiner is dan de golflengte van het licht. Met behulp van transformatieoptica ontwerpen we vier optische caviteiten. De eerste twee—de gekende onzichtbaarheidsmantel en een hyperbolische transformatie—hebben geen subgolflengte oplossingen. Het derde ontwerp vertoont een continuüm aan subgolflengte modes, maar is jammer genoeg heel gevoelig aan materiaalperturbaties. In het laatste ontwerp elimineren we deze gevoeligheid terwijl enkele subgolflengte modes bewaard blijven. Deze laatste twee caviteiten, deels gemaakt uit linkshandige materialen, hebben diep subgolflengte modes.

Een tweede component die we bestuderen is een frequentietuner. Momenteel is het vrij moeilijk om nauwkeurig de frequentie van elektromagnetisch golven te veranderen. Bovendien worden er in dit proces vaak ongewenste zijbanden gegenereerd. We passen daarom het mechanisme toe van de grootste frequentieshifter die bestaat: het universum. Licht dat propageert doorheen het heelal heeft geen constante frequentie, vermits het onderworpen is aan zogenaamde gravitationele en kosmologische roodverschuivingen. We berekenen de materiaalparameters die nodig zijn om deze roodverschuivingen te implementeren met behulp van diëlektrica en naar analogie van de kosmologische redshift stellen we een component voor waarmee het mogelijk is om de frequentie te veranderen. We bewijzen dat deze component, dewelke gebruik maakt van een tijdsvariërende brekingsindex, een perfecte frequentieshifter kan zijn.

vi

Résumé

L'optique des transformations fournit une nouvelle manière de regarder l'interaction entre la lumière et la matière. Cette méthode développée récemment dans l'électromagnétisme est basée sur l'analogie entre les équations macroscopiques de Maxwell dans les diélectriques complexes et les équations de Maxwell en espace libre sur le fond d'un métrique arbitraire. La réalisation de ces diélectriques complexes exige l'utilisation des métamatériaux. Dans ce travail de fin d'étude, nous adoptons cette methode afin de concevoir deux composants optiques originaux.

D'abord, nous employons l'optique des transformations pour l'exécution des cavités optiques. Traditionnellement, des microcavités optiques sont limitées dans la taille due à la nature onduleuse de la lumière. Ceci le rend impossible de confiner la lumière en volume dont les dimensions sont plus petites que la longueur d'onde de la lumière. Utilisant l'optique des transformations, nous dérivons quatre conceptions pour une cavité optique. Les deux premiers, un manteau d'invisibilité traditionnel et une carte hyperbolique, ne montrent pas les modes sub-longueur d'onde. La troisième conception offre un continuum de modes sub-longueur d'onde, mais est extrêmement sensible aux perturbations matérielles. Dans la dernière conception, nous avons éliminé cette sensibilité tout en gardant certains des modes sub-longueur d'onde. Les deux derniers dispositifs, qui sont partiellement faits avec les matériaux gauchers, ont des modes profondément sub-longueur d'onde.

Le deuxième composant que nous adressons est un dispositif pour changer la fréquence. Pour l'instant, il est tout à fait difficile de réaliser le décalage précis de fréquence de l'énergie électromagnétique. D'ailleurs, ce processus produit souvent des bandes latérales non désirées. Par conséquent, nous mettons en application le mécanisme du plus grand levier de fréquence qui existe : l'univers. Pendant que la lumière voyage d'un endroit à l'autre dans l'espace extra-atmosphérique, la fréquence d'un photon change, puisqu'elle est soumise au décalage vers le rouge gravitationel et cosmologique. Nous calculons les propriétés des matériaux priées pour mettre en application ces décalages vers le rouge cosmologique avec des diélectriques et pour proposer un levier de fréquence. Nous prouvons que ce dispositif, qui a besoin d'un indice de réfraction dépendant du temps, est un levier parfait de fréquence.

Contents

CHAPTER 1

Prelude

"Time and space. . . It is not nature which imposes them upon us,
it is we who impose them upon nature because we find them convenient." — *Henri Poincaré*

1.1 Context

The fundamental interaction between light and matter enables to generate, manipulate and detect the properties of light. Traditional optical components already achieve this up to a very high degree: optical fibre connections that guide optical signals over long distances, lensing systems for optical imaging, dielectric microcavities to confine electromagnetic energy, or nonlinear devices that enable frequency manipulations are just a few examples.

The advent of *metamaterials*—man-made, subwavelength structures whose electromagnetic interaction can be designed—opens up a new world of possibilities. Whereas traditional materials only interact with light through the electric permittivity, metamaterials can have an effective permittivity *and* permeability different from unity at optical frequencies. Moreover, they offer the possibility to design left-handed materials.

Transformation optics, on the other hand, is a theoretical framework for the design of optical devices that uses the analogy between dielectrics and nontrivial geometries. It imposes constraints on the material's response that can be made using metamaterials. Transformation optics and metamaterials can thus be combined to create components that are science fiction within the framework of traditional optics. The invisibility cloak, the device that renders even the strongest scatterers invisible, is perhaps the best example.

1.2 Motivation

In this thesis, we want to further explore the potential of transformation optics.

Firstly, we will attempt to use the formalism to design an optical cavity. Traditional optical cavities, such as optical microcavities, are limited in size due to the wavelike nature of light. The largest wavelength that can be confined is approximately equal to the characteristic size of the structure and it is thus impossible to make the cavities smaller than the wavelength under consideration. This is exactly what we will try to overcome. Such a cavity with subwavelength dimensions would, e.g., pave the way for miniaturisation in optical data processing.

Secondly, we will asses the techniques of space-time transformation optics in the design of a frequency tuner. The frequency of electromagnetic energy cannot be tuned easily. Very often, unwanted sidebands will appear in the process and the conversion is generally not efficient. An approach using transformation optics might solve some of these problems. A frequency shifter can be readily used for several laser applications or could be applied for all-optical frequency modulation.

The third and perhaps main purpose of this work will be to obtain a deeper understanding of the electromagnetic interaction with matter, looking for fundamental laws and limitations in a world where materials have no constraints.

1.3 Structure

In chapter 2, we will present the reader a brief introduction to the world of metamaterials. Starting from a little history, we will highlight the most important properties of these structures. This chapter also contains the well-known results on the behaviour of light in left-handed materials. We conclude with a discussion on the perfect lens.

In the next chapter, we will give a detailed description of transformation optics. This will include an indespensible introduction to the language of differential geometry. We will also derive the formulae that are used to design the material's permittivity and permeability and we will generalise them for transformations with the background of an anisotropic material. The theory will become clear by considering to examples: the invisibility cloak and the perfect lens.

Dielectric microcavities are currently the state-of-the-art devices to confine light in small regions. We will analyse their modes in the fourth chapter. This will serve two purposes: it will give an idea of the current short comings of these devices, and the used techniques of calculating the modes will be benchmarked with results from the literature.

In the next two chapters we will use transformation optics to design alternatives for these cavities. In chapter 5, we will analyse the confining capabilities of the invisibility cloak and propose a new component. Both devices potentially are cavities, but do not satisfy our demand of *subwavelength confinement*. In chapter 6 we will introduce a device that has infinitely many subwavelength modes. These modes, however, are extremely sensitive to geometrical perturbations. Due to its analogy with the perfect lens, we will name it *the perfect cavity*. We conclude this chapter with

a derived design that still inhibits subwavelength modes and does not suffer from the extreme sensitivity.

In the seventh and last chapter, we will design a frequency shifter. First, we have to generalise the transformation formulae for general space-time geometries. Then we implement two solutions from general relativity that both inhibit a redshift. Although the Schwarzschild solution does not give satisfying results, the Robertson-Walker metric can perfectly be used in the implementation of a frequency shifting device.

CHAPTER 2

Metamaterials

This chapter contains a brief introduction to metamaterials. In the first section, we will explain the underlying physical principles of these materials. Subsequently, we will demonstrate some well-known properties of left-handed materials. We end this chapter with a discussion on the perfect lens, which can image light with subwavelength resolution.

2.1 Introduction

In recent decades, photonics has become a rapidly growing discipline involving different applications, ranging from very fundamental sciences to a broad range of industrial applications. The use of electromagnetic waves at optical frequencies has gained popularity due to the high degree of control, which is obtained by manipulating the light through the interaction with materials. This interaction is described by the *macroscopic Maxwell's equations*

$$\nabla \cdot \mathbf{D}(\mathbf{r}, t) = \rho_{\text{free}}(\mathbf{r}, t), \tag{2.1}$$

$$\nabla \cdot \mathbf{B}(\mathbf{r}, t) = 0, \tag{2.2}$$

$$\nabla \times \mathbf{E}(\mathbf{r}, t) = -\frac{\partial \mathbf{B}(\mathbf{r}, t)}{\partial t}, \tag{2.3}$$

$$\nabla \times \mathbf{H}(\mathbf{r}, t) = \frac{\partial \mathbf{D}(\mathbf{r}, t)}{\partial t} + \mathbf{J}_{\text{free}}(\mathbf{r}, t), \tag{2.4}$$

in combination with constitutive equations that define the material's response

$$\mathbf{D}(\mathbf{r}, \omega) = \epsilon_0 \epsilon(\mathbf{r}, \omega) \mathbf{E}(\mathbf{r}, \omega), \tag{2.5}$$

$$\mathbf{B}(\mathbf{r}, \omega) = \mu_0 \mu(\mathbf{r}, \omega) \mathbf{H}(\mathbf{r}, \omega), \tag{2.6}$$

$$\mathbf{J}_{\text{free}}(\mathbf{r}, \omega) = \epsilon_0 \sigma(\mathbf{r}, \omega) \mathbf{E}(\mathbf{r}, \omega), \tag{2.7}$$

where ϵ_0 and μ_0 are the free-space permittivity and permability, respectively, ϵ and μ correspond to the relative permittivity and permeability, and the electrical conductivity of the material is abbreviated by σ [1]. In these constitutive equations, we have restricted ourselves to a linear, isotropic material, which is sufficient for our purpose. These equations are the result of an overall averaging of the effect of every individual atom inside the material. This *effective medium approach* is certainly valid at optical frequencies since the corresponding wavelength of such electromagnetic waves is orders of magnitude larger than the functional elements: the wavelength of visible light $\lambda_{\text{optical}} \approx 500$ nm is much larger then the characteristic length of an atom = 1Å. The above mentioned ability to manipulate light with materials results from our degree of controlling the constitutive parameters. In naturally occurring materials, however, the magnetic permeability μ is extremely close to unity at optical frequencies and so we are limited to varying the electric permittivity.

Unconstrained by these naturally occurring limitations, Victor Veselago published in 1968 a seminal paper in which he introduced the concept of left-handed media, having simultaneously $\epsilon < 0$ and $\mu < 0$ [2]. These media would experience peculiar properties such as negative refraction—introducing the possibility of a planar lens—and the inversion of the Doppler shift. Due to the purely hypothetical nature of these results, they did not gain a lot of attention in those days.

In 2000, the exploratory efforts of Veselago were revalued when Smith *et al.* realised a left-handed material experimentally [3, 4]. Using a composite material built with an array of tiny metallic structures, negative refraction was observed at microwave frequencies. The ideas behind such a composite structure were delivered by Pendry *et al.* [5]. They introduced the concept of a metamaterial, which is an artificial structured medium in which subwavelength components determine the electromagnetic properties. In short, the function of an individual atom of natural occurring media is replaced by little man-made structures that can be designed with specific characteristics. In the next section, we will discuss the underlying ideas behind these materials and how they are designed. This will necessarily be a brief introduction. The interested reader can find a more elaborate discussion in Refs. [6, 7].

2.2 Metamaterials for Left-Handed Light

2.2.1 Negative Permittivity

Negative permittivities can be found in naturally occurring materials. The dielectric function of a simple metal is given by

$$\epsilon(\omega) = \epsilon_0 \left(1 - \frac{\omega_{\text{p}}^2}{\omega(\omega + i\gamma)} \right). \tag{2.8}$$

The plasma frequency ω_{p} is given by

$$\omega_{\text{p}}^2 = \frac{Ne^2}{m\epsilon_0}, \tag{2.9}$$

where N, e and m represent the density, the charge and the mass of the electrons, respectively. Dissipation is taken into account by the damping rate γ. If the frequency is much lower than

the plasma frequency, the attenuation will be too high and the field will not penetrate into the metal.

In Ref. [5] Pendry *et al.* proposed an array of *thin metallic wires*, shown in Fig. 2.1, that—on average—acts like a plasma with a dispersion relation given by Eq. (2.8). Such a structure has a tunable electron density N_{eff} and electron mass m_{eff}, both depending on the geometrical parameters of the composite structure: the lattice constant a, and the radius of the wires r. Using copper wires with a radius $r = 1.0\,\mu\text{m}$ and a lattice constant $a = 5.0\,\text{mm}$, they achieved a plasma frequency $\omega_{\text{p}} = 2\pi \times 8.2\,\text{GHz}$. Hereby, they realised a negative permittivity with low attenuation in the microwave band.
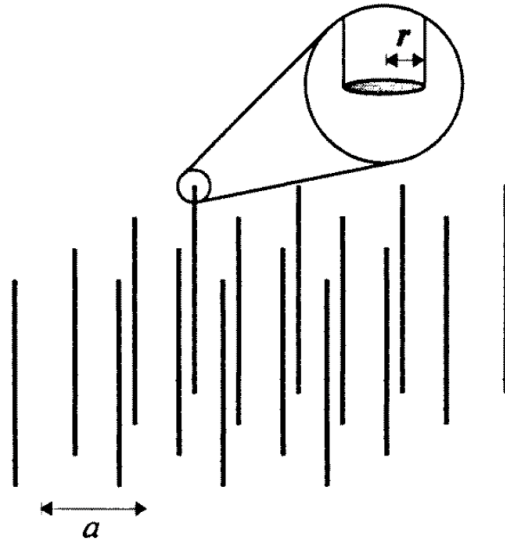
Figure 2.1: A periodic array of thin metallic wires has a dispersion function $\epsilon(\omega)$ of a plasma, in which we can tune the plasma frequency ω_{p} with the geometrical parameters a, the lattice constant, and r, the wire's radius. Reproduced from Ref. [5].

2.2.2 Negative Permeability

Achieving negative permeability is a less straightforward issue. It was again Pendry and his co workers that provided a solution: a square lattice of *split-ring resonators* [8]. To understand the physical principle of these structures, let us first consider an array of closed conducting rings with radius r. A magnetic field component H that is directed perpendicular to the plane of these rings will generate an electromagnetic force in the rings. The current I inside a single ring can be calculated by a traditional LR-circuit analogy:

$$I = -\frac{\phi}{L + iR/\omega},\tag{2.10}$$

where the magnetic flux ϕ is proportional to the applied field: $\phi = \mu_0 \pi r^2 H$. Each individual ring will then generate a magnetic dipole $m = \pi r^2 I$ and a three-dimensional array of these

components will have—on average—a permeability that is given by

$$\mu = 1 - \frac{F\omega^2}{\omega^2 + i\omega\Gamma}, \tag{2.11}$$

where F is a geometry-dependent factor that encodes the compactness of the array and Γ is the damping rate, depending on the resistance of the individual rings. Since F is necessarily much smaller than one, such an array of closed rings would not provide the possibility for negative permeability. By opening the ring with a little gap, the equivalent electrical circuit becomes an *RLC*-circuit, in which we introduce a resonance for the current characteristic. The resulting permeability is given by

$$\mu = 1 - \frac{F\omega^2}{\omega^2 + i\omega\Gamma - \omega_r^2}. \tag{2.12}$$

The resonance frequency is given by $\omega_r = 1/\sqrt{LC}$. The regions with negative permeability are situated around this frequency where, unfortunately, we encounter the biggest absorption peak.
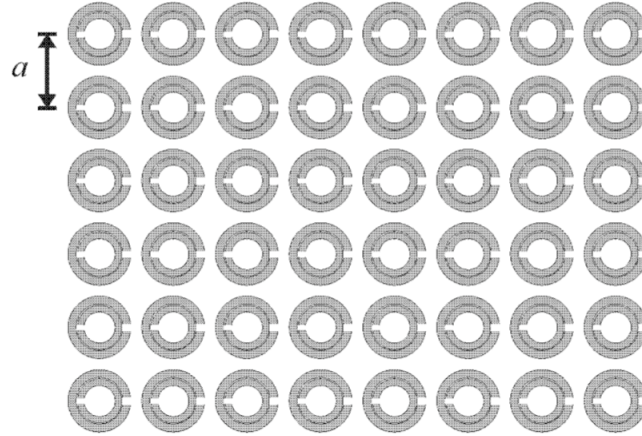
Figure 2.2: An array with lattice constant a of split-ring resonators, that generate negative permeability in a narrow frequency band. The split-rings are combined in pairs—with the gap in different direction—to enhance the symmetry of the structure. Reproduced from Ref. [8].

2.2.3 From Microwaves to Optical Frequencies

The combination of thin wires and split-ring resonators can achieve the purpose of combining ϵ and μ simultaneously negative. One should, however, be careful when combining these structures, since the split-ring resonators will influence the plasma frequency ω_p of the wires. Experimentally, the first demonstration of negative refraction was obtained by measuring the transmitted power as a function of the frequency. In the effective medium approximation and neglecting losses inside the material, we find that the magnitude of the wave vector **k** inside the

material is given by

$$k^2 = \epsilon(\omega)\mu(\omega)\frac{\omega^2}{c^2} \approx \frac{\omega^2 - \omega_p^2}{c^2}\frac{\omega^2 - \omega_b^2}{\omega^2 - \omega_r^2}, \tag{2.13}$$

with $\omega_b = \omega_0\sqrt{1-F}$. We notice therefore a window $\omega_r < \omega < \omega_b$ in which $k^2 > 0$ where propagation is allowed. The transmission spectrum of the experiment is shown in Fig. 2.3. The solid line indicates the transmission when using only split-ring resonators, where the minimum coincides with the region of negative μ. The dashed line shows the transmission spectrum when the thin wires are added. The region with $\mu < 0$ now indicates a maximum due to the combination with $\epsilon < 0$.
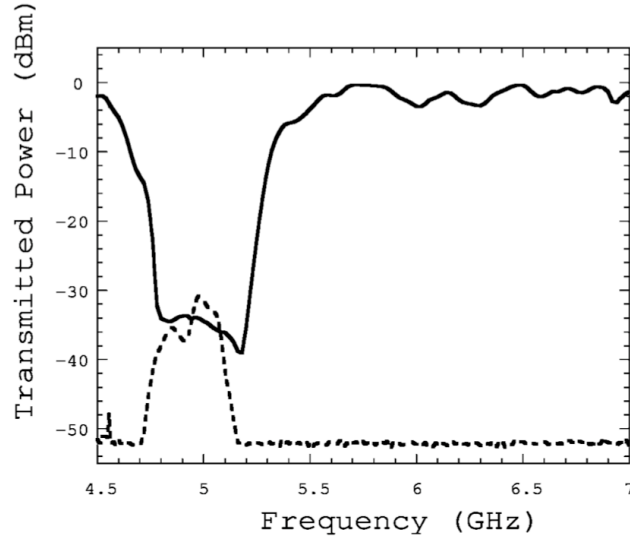
Figure 2.3: The transmission spectrum of a composite material combining split-ring resonators and thin wires. The solid line is the transmission in absence of the thin wires. The dashed line shows the transmission when both components (split-rings and thin wires) are present. Around 4.9 GHz, the composite material has left-handed behaviour. Reproduced from Ref. [3].

In the following years, researchers aimed to increase the operational frequency, which roughly equals $\omega_r = 1/\sqrt{LC}$. At first, this was done by scaling the components: since L and C are proportional to the dimensions, ω_r scales inversely proportional to the dimensions of the functional elements. This linear scaling behaviour unfortunately breaks down when the frequency becomes too high, as the kinetic inductance of the electrons L_e is inversely proportional to the dimensions and becomes dominant over the magnetic inductance L_m [9]. At very high frequencies, the resonance frequency will thus approach a constant.

To push the frequency above 100 THz into the optical regime, several new designs were suggested, the most important being the *cut-wire pairs* and the *fishnets*, both shown in Fig. 2.4. It is quite difficult to obtain simultaneously ϵ and μ negative using the cut-wire structure. The

(a)   (b)
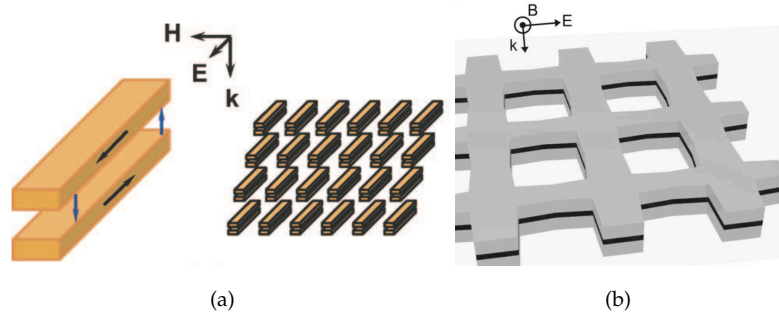
Figure 2.4: New designs to achieve negative permittivity and permeability at optical frequencies. (a) The cut-wires, where the magnetic field, polarised as in indicated will generate negative permeability. Reproduced from Ref. [10]. (b) The fishnet design, where a dielectric layer is sandwiched between two metallic layers. The structure combines electric and magnetic resonances at the same frequencies. Reproduced from Ref. [11].

most promising results have been obtained using fishnets. These structures have achieved left-handedness at infrared and visible wavelengths.

2.3 Electrodynamics of Left-Handed Light

Before we take a closer look at the propagation inside left-handed materials, let us first demystify the origin of the name *left-handed light*. Therefore, consider a plane wave $\mathbf{E} = \mathbf{E}_0 e^{i(\mathbf{k} \cdot \mathbf{r} - \omega t)}$ propagating through a material with negative permittivity and permeability. Maxwell's curl equations (2.3)-(2.4), in combination with the constitutive equations (2.5)-(2.6) then yield

$$\mathbf{k} \times \mathbf{E}_0 = \omega \mu(\omega) \mathbf{H}_0, \tag{2.14}$$

$$\mathbf{k} \times \mathbf{H}_0 = -\omega \epsilon(\omega) \mathbf{E}_0. \tag{2.15}$$

This implies that $\mathbf{E}$, $\mathbf{H}$ and $\mathbf{k}$ form a left-handed basis when ϵ and μ are negative, hence the name left-handed light.

In combination with the fact that $\mathbf{S} = \mathbf{E} \times \mathbf{H}$, which is valid in any material, we find that $\mathbf{k}$ is directed in the opposite direction than Poynting's vector $\mathbf{S}$, which indicates the direction of energy flow.

2.3.1 Negative Index of Refraction

Now we have demonstrated the possibility of fabricating materials whose permittivity and permeability can be simultaneously negative, it is time to have a look at the electrodynamics of these media. Let us first have a look at the index of refraction. This material parameter is defined as

$$n = \pm \sqrt{\frac{\epsilon \mu}{\epsilon_0 \mu_0}}. \tag{2.16}$$

But why should we take the negative root when both ϵ and μ are negative? To understand this we have to approach ϵ, μ and n as complex parameters, taking into account absorption:

$$\frac{\epsilon}{\epsilon_0} = r_\epsilon e^{i\theta}, \tag{2.17}$$

$$\frac{\mu}{\mu_0} = r_\mu e^{i\phi}, \tag{2.18}$$

In a passive material, the imaginary part of these parameters has to be positive, implying that the waves decay with time.* Therefore, both ϕ and θ are angles between $\pi/2$ and π, since the real parts of ϵ and μ are negative. The refractive index n can either be $n_1 = \sqrt{r_\epsilon r_\mu} e^{(\theta+\phi)/2}$, or $n_2 = \sqrt{r_\epsilon r_\mu} e^{(\theta+\phi)/2+\pi}$. Since n_2 has a negative imaginary part, which is not possible in a passive material, we have to define n_1 as the refractive index.

2.3.2 Negative Refraction

The most famous property of a negative index of refraction is probably the associated negative refraction at the interface between a right-handed material and a left-handed material, where the light rays bend *in the wrong way*. This is an immediate consequence of Snell's law:

$$n_1 \sin \theta_i = n_2 \sin \theta_t. \tag{2.19}$$

Provided that this law is still valid for these interface, as proven in [2], we find that θ_t has to be negative when n_2 is negative. The effect is shown in Fig. 2.5.
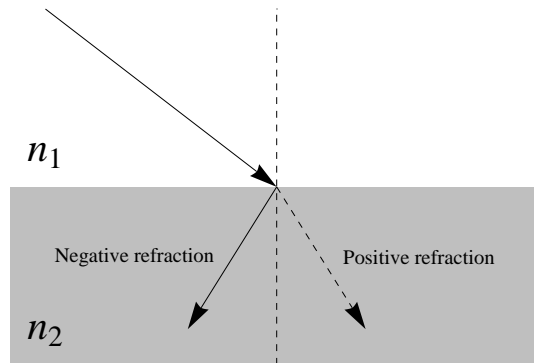
Figure 2.5: An incident light ray is bent in the wrong direction when at the boundary between a left- and a right-handed material with refractive indices n_1 and n_2, respectively. The dashed arrow indicates the traditional direction of a refracted ray.

2.3.3 The Perfect Lens

In his seminal paper, Veselago introduced an interesting application of negative refraction [2]: a planar lens, consisting of a material with $n = -n_0$ between two planar facets. As shown in

---

*When we apply the convention of time variations $e^{-i\omega t}$.

Fig. 2.6, each ray is refracted at the boundaries of the lens. When the object is positioned close enough to the lens—at distance l from the leftmost boundary smaller then the total width of the lens d, it will have an image behind the lens that is situated at a distance $d - l$ from the rightmost boundary. We notice that there will be a second image inside the lens at the first intersection of the rays.

In 2000, Pendry has shown that Veselago's lens has the property of subwavelength imaging [12]. Whereas normal lens systems all have a natural resolution, determined by the wavelength of the light under consideration, this *superlens* images all information in the object, including the evanescent tails. In the next chapter, we will approach this device from a different angle, since we will demonstrate how this superlens can be understood within the framework of transformation optics.
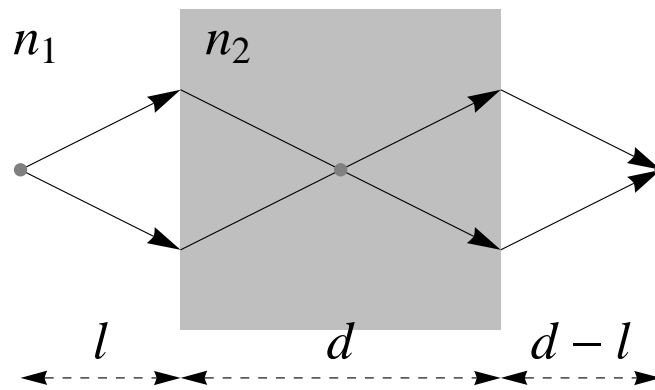
Figure 2.6: A planar device with negative refractive index $n_2 = -n_1$ can function as a lens. Rays that are emitted from an object at distance $l < d$ from the left boundary are refracted two times at the interfaces of the lens and converge back to form an image behind the device. We notice also that a second image is situated inside the lens.

References

[1] J. D. Jackson, *Classical Electrodynamics (3rd edition)*, Wiley, New York, 1999.

[2] V. G. Veselago, "The electrodynamics of substances with simultaneously negative values of ϵ and μ," *Sov. Phys. Usp.* **10**, 509–514, 1968.

[3] D. R. Smith, W. Padilla, D. Vier, S. Nemat-Nasser, and S. Schultz, "Composite medium with simultaneously negative permeability and permittivity," *Phys. Rev. Lett.* **84**, 4184–4187, 2000.

[4] R. A. Shelby, D. R. Smith, and S. Schultz, "Experimental verification of a negative index of refraction," *Science* **292**, 77–79, 2001.

[5] J. B. Pendry, A. J. Holden, D. J. Robbins, and W. J. Stewart, "Low frequency plasmons in thin-wire structures," *J. Phys.: Cond. Matter* **10**, 4785–4809, 1998.

[6] P. Tassin, *Metamaterials for advanced photonic applications: Reconsidering the Classical Laws of Optics*. PhD thesis, Vrije Universiteit Brussel, 2009.

[7] P. W. Milonni, *Fast light, slow light and left-handed light*, Taylor and Francis, New York, 2005.

[8] J. B. Pendry, A. J. Holden, D. J. Robbins, and W. J. Stewart, "Magnetism from conductors and enhanced nonlinear phenomena," *IEEE Trans. Micr. Theory and Techniques* **47**, 2075–2084, 1999.

[9] J. Zhou, T. Koschny, M. Kafesaki, E. N. Economou, J. B. Pendry, and C. M. Soukoulis, "Saturation of the magnetic response of split-ring resonators at optical frequencies," *Phys. Rev. Lett.* **95**, 223902, 2005.

[10] V. M. Shalaev, W. Cai, U. Chettiar, H.-K. Yuan, A. K. Sarychev, V. P. Drachev, and A. V. Kildishev, "Negative index of refraction in optical metamaterials," *Opt. Lett.* **30**, 3356–3358, 2005.

[11] G. Dolling, M. Wegener, C. M. Soukoulis, and S. Linden, "Negative-index metamaterial at 780 nm wavelength," *Opt. Lett.* **32**, 53–55, 2007.

[12] J. B. Pendry, "Negative refraction makes a perfect lens," *Phys. Rev. Lett.* **85**, 3966–3969, 2000.

CHAPTER 3

Transformation Optics

A new paradigm to study the interaction between light and matter. That would be a one-sentence-definition of transformation optics. In this chapter we will spend some more time on this fascinating theory that brought us the invisibility cloak. Although a bit farfetched at first sight, we will start the presentation by introducing some basic concepts of differential geometry, the language of Einstein's general relativity. Their usefullness will become clear in the subsequent section where we will derive the mathematical formalism of transformation optics starting from Maxwell's equations. The implementation of an inivisibility cloak will be an illustrative example to demonstrate how these equations turn into practical realisations of ideas. We will conclude this chapter with an analysis of the invisibility cloak and the perfect lens. Most of the results presented in this chapter are due to the pioneering work of Ulf Leonhardt [1] and John Pendry [2].

3.1 Introduction

Electromagnetic fields perceive a different reality from ours. Usually, we are not aware of this property. When we look in the mirror, e.g., we confide in light to give us a true picture of our face. In some cases, however, light is not such a loyal ally to describe our surroundings. A well-known example hereof takes place above the hot sand of the desert. An unfortunate physicist could be fooled by the illusion of an oasis when he does not keep in mind that there is a difference between his and the photon's reality. This is because light is travelling along the shortest *optical* path.* Therefore, light rays coming from the sky are refracted along the earth's surface towards the observer. Fig. 3.1 clearly shows the difference between the optical and the Euclidean distance between two points *A* and *B*, when the refactive index varies in the vertical direction. However, instead of passively undergoing the tricks of light, we can use these effects to enhance our control over electromagnetic fields. This is the basic idea behind transformation

---

*Actually, light travels along paths with *extremal* optical path length.
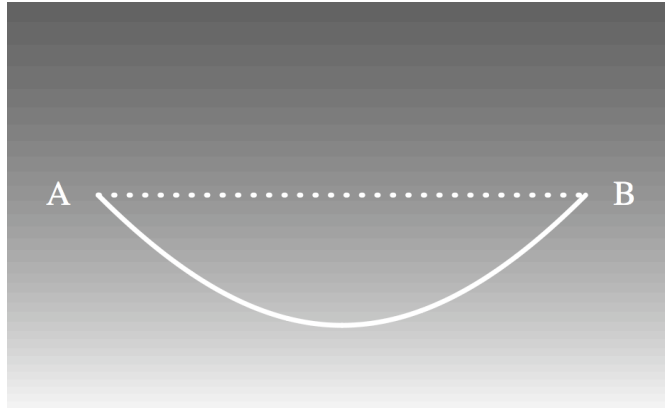
Figure 3.1: The optical path (full line) differs significantly from the Euclidean shortest path (dotted line) between two points in media with an inhomogeneous index of refraction n. The shortest optical path runs through the area with lower n. This phenomenon is responsible for fata morganas above the hot sand (lower n) in the dessert: an observer, positioned in A, would think that the blue colour, coming from the sky in B, originates from the earth's surface, since he perceives it at a different angle. Reproduced from Ref. [1].

optics: controlling the electromagnetic fields by influencing the electromagnetic reality. This reality is co-determined by the constitutive parameters of the medium.

This idea is not new at all. Although the concepts date back to antiquity and can be found in the work of Hero of Alexandria, Fermat is probably the first to define the optical distance in his variational principle: when travelling between two points, light will travel along the path which generates an extremal optical path length (OPL). This quantity is defined as the geometrical length—as we would measure it—multiplied with the refractive index:

$$OPL = \int_A^B n \, dl. \tag{3.1}$$

Physically this formula can be understood as follows: in the 'wave-language', monochromatic light can be characterised by its vacuum wavelength λ_0. In a medium with refractive index n, this wavelength is altered to $\lambda = \lambda_0/n$. In a region with higher n the wavelength will be smaller than in a region with lower n. Now one could imagine that a light ray with a smaller wavelength measures a larger space than a ray corresponding to a larger wavelength, just as you would ask a baby or a T-rex to gauge a hundred meters. Reality is relative to whom is measuring it.

The use of geometrical tools for the description of the propagation of light in media was further elaborated in the previous century. This evolution and corresponding references can be found in Ref. [1]. From these, we want to highlight the work of Plebanski [3], who investigated the scattering of electromagnetic plane waves due to a nontrivial gravitational field, by introducing

Plebanski's constitutive equations, connecting the macroscopic fields $\mathbf{D}$ and $\mathbf{H}$ with $\mathbf{E}$ and $\mathbf{B}$:

$$\mathbf{D}(\mathbf{r}, \omega) = \epsilon_0 \epsilon(\mathbf{r}, \omega) \mathbf{E}(\mathbf{r}, \omega) + \frac{\mathbf{w}(\mathbf{r}, \omega)}{c} \times \mathbf{H}(\mathbf{r}, \omega),$$

$$\mathbf{B}(\mathbf{r}, \omega) = \mu_0 \mu(\mathbf{r}, \omega) \mathbf{H}(\mathbf{r}, \omega) - \frac{\mathbf{w}(\mathbf{r}, \omega)}{c} \times \mathbf{E}(\mathbf{r}, \omega), \tag{3.2}$$

where $\mathbf{w}$ represents the bi-anisotropy vector of the material. This way, he introduced an important conceptual insight: not only the properties of matter, but also the background of space-time can be contained within the constitutive equations.

Although the ideas were hanging around since a long time known, it took until 2006 for transformation optics to appear in the literature. That year, Leonhardt [4] and Pendry *et al.* [2] independently proposed methods for the design of an optical invisibility cloak. The first paper applies a conformal transformation to Helmholtz' equation to derive a refractive index profile $n(x, y)$ that achieves perfect invisibility [4]. The method, however, is only valid within the realm of geometrical optics. The second paper investigates how ϵ and μ change when performing a general coordinate transformation of Maxwell's equations [2]. Both papers use an "electromagnetic space" as a tool to derive material properties in physical space. These concepts will be further clarified in Sec. 3.3.

Although its first and most famous application is the invisibility cloak, transformation optics has proven to allow for very broad range of applications: concentrators [5], beam expanders [6], beam bends [7], beam shifters [8], polarisation splitters and polarisation rotators [9], electromagnetic wormholes [10], a hyperlens [11], a superantenna [12] and many other electromagnetic devices have been suggested. The applicability can be even more extended by the introduction of transformations involving the time-coordinate [13].

The research behind transformation optics gained momentum thanks to the promising advent of metamaterials, based on two effects: firstly, metamaterials lead the optical engineer to dream he is living in a world where everything is possible, secondly, these materials with numerous degrees of freedom demand a general design technique to implement them in optical systems.

3.2 Toolbox Differential Geometry

An unaccelerated object* moves along the geodesics of space-time. What we perceive as the force of gravity is actually the curvature of space-time in the presence of energy and momentum, which alters the geodesics on which we tend to stay. This is how Einstein generalised Newton's theory of gravity to what we now call general relativity [14]. Minkowski space-time from special relativity had to be replaced by a more general, curved space. These curved spaces are the subject of *differential geometry*. Since this mathematical discipline does not belong to the canon of electromagnetic knowledge, we will give a brief introduction to its main concepts. For this introduction, we have been inspired by Refs. [1, 15].

---

*This is by definition an object which is only subject to gravity
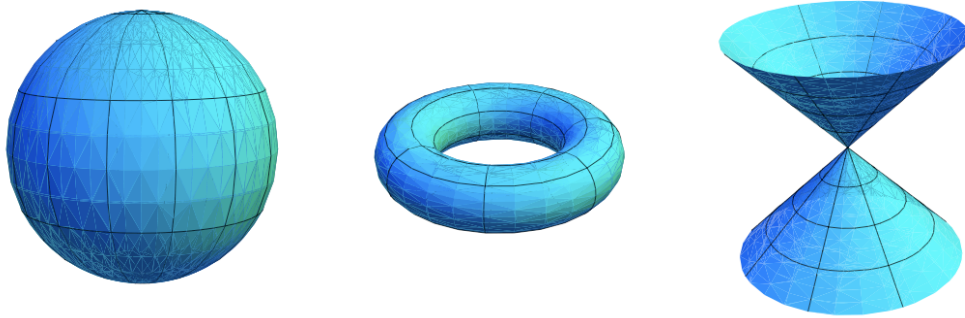
Figure 3.2: Definition of manifolds: a sphere (left) and a torus (middle) locally look like $\mathbb{R}^2$, two cones intersecting at their vertices (right) have one point (the vertex) which does not look like $\mathbb{R}^n$.

3.2.1 Manifolds

Manifolds are very fundamental concepts in mathematics and physics. They represent the generalisation of the well-known n-dimensional Euclidean space and incorporate more complicated sets such as a sphere or a torus. Although not very rigourous, we will define a manifold M as a set which "locally looks like" $\mathbb{R}^n$. A formal definition of what is actually meant with "locally looks like" can be found in Ref. [15]. For our purpose of introducing transformation optics, it is important to have some intuitive feeling of what a manifold actually is. Therefore we give two examples in Fig. 3.2 that are manifolds (sphere, torus) and one that is not (intersecting cones). These manifolds will serve as the background on which we will introduce the following concepts.

3.2.2 Vectors

Vectors are objects from a vector space. We can define them on a manifold. The velocity of a particle, moving on a manifold, is an example of such a vector **V**. It is important to stress that a vector is located at a given point of the manifold and not stretching from one point to another. At each point of the manifold, we can define a tangent space $\mathbf{T}_P$, which is the set of all possible vectors in that point. On this tangent space $\mathbf{T}_P$, we can define a coordinate system by introducing a set of basis vectors $\mathbf{e}_{(i)}$. With respect to this basis, a general vector **V** in the point P can be decomposed as:

$$\mathbf{V} = V^i \mathbf{e}_{(i)}. \tag{3.3}$$

This expression could be somewhat mysterious at first sight, due to the appearance of the indices. When working in a three-dimensional manifold, i can take the values $(1, 2, 3)$, corresponding to the number of basis vectors.* With this equation we also introduce *Einstein's summation*

---

*In the three-dimensional case, we also use the Latin letters $j, k \ldots$ as an index, four-dimensional manifolds (such as Minkowski's space-time) use Greek indices $\mu, \nu \ldots$
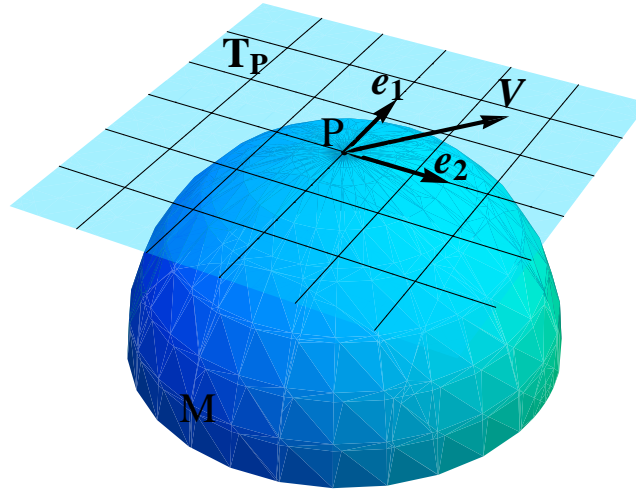
Figure 3.3: A vector **V** associated with a point P of a manifold M lives in the tangent space
$\mathbf{T}_P$ and can be decomposed with respect to basis vectors $\mathbf{e}_1$ and $\mathbf{e}_2$, according to Eq. (3.3).

convention: an expression with a repeated index appearing as an upper and a lower index
(superscript and subscript) implies a summation over this index. Such an index is called a
dummy index. An index which is not summed over (and by definition is appearing at both
sides of an equation) is a free index, implying that the equation is valid for every possible value
of that index $(1, 2, 3)$. This convention enables us to abreviate our expressions. Eq. (3.3) should
thus be read as

$$\mathbf{V} = V^1 \mathbf{e}_1 + V^2 \mathbf{e}_2 + V^3 \mathbf{e}_3. \tag{3.4}$$

The brackets around the i of the basis vectors in Eq. (3.3) are there to remind us that we are
summing over a set of vectors instead of the components a vector. The norm of a vector, e.g.,
can easily be written as

$$\|\mathbf{V}\| = V^i V_i = V^1 V_1 + V^2 V_2 + V^3 V_3. \tag{3.5}$$

Eq. (3.3) clearly demonstrates that a vector has an existence independent of a coordinate system.
A coordinate system acts as a means to introduce the components of that vector, which is quite
uselful in practical calculations. For the sake of generality, we will therefore define a vector as
a geometrical entity in a point P of a manifold M, which lives in the tangent space $\mathbf{T}_P$ and is
characterised by components with an upper index i.

3.2.3 One-forms and Tensors

In Eq. (3.5), we introduced V_i. These are components with a lower index, corresponding to
a one-form (or dual vector). Just like vectors, dual vectors are associated with a point P of a
manifold M and have an existence independent of a coordinate system. The collection of all

dual vectors in a point P defines the dual vector space $\mathbf{T}^*_P$. In this space we can equivalently define basis dual vectors $\boldsymbol{\theta}^{(i)}$, such that a general dual vector $\boldsymbol{\omega}$ can be written as:

$$\boldsymbol{\omega} = \omega_i \boldsymbol{\theta}^{(i)}. \tag{3.6}$$

We can approach these dual vectors now from a different point of view: by introducing an additional equation between both sets of basis vectors $\mathbf{e}_{(i)}$ and $\boldsymbol{\theta}^{(j)}$:

$$\mathbf{e}_{(i)}\boldsymbol{\theta}^{(j)} = \delta_i^j. \tag{3.7}$$

then we can regard a dual vector as a linear map from the vector space $\mathbf{T}_P$ to the real numbers:

$$\boldsymbol{\omega}(\mathbf{V}) = \omega_i \boldsymbol{\theta}^{(i)} V^j \mathbf{e}_{(j)} = \omega_i V^j \delta_i^j = \omega_i V^i. \tag{3.8}$$

This concept can be generalised to a multilinear map from a set of k vectors and r dual vectors to $\mathbb{R}$. Keeping in mind Einstein's summation convention, we know this object should be looking like:

$$\mathbf{T} = T^{i_1 i_2 \ldots i_r}{}_{j_1 j_2 \ldots j_k} \mathbf{e}_{(i_1)} \otimes \mathbf{e}_{(i_2)} \ldots \mathbf{e}_{(i_r)} \otimes \boldsymbol{\theta}^{(j_1)} \otimes \boldsymbol{\theta}^{(j_2)} \ldots \boldsymbol{\theta}^{(j_k)}, \tag{3.9}$$

since it should contract with k objects with a lower index and r objects with a upper index. Eq. (3.9) defines the components of the tensor of rank (r, k) as a function of the basis vectors and dual vectors. This expression contains the *tensor product* operation $\otimes$, that defines a product between a (k, l) tensor $\mathbf{T}$ and a (m, n) tensor $\mathbf{S}$ by

$$\mathbf{T} \otimes \mathbf{S}(\boldsymbol{\omega}^{(1)} \ldots \boldsymbol{\omega}^{(k+m)}, \mathbf{V}^{(1)} \ldots \mathbf{V}^{(l+n)}) = \mathbf{T}(\boldsymbol{\omega}^{(1)} \ldots \boldsymbol{\omega}^{(k)}, \mathbf{V}^{(1)} \ldots \mathbf{V}^{(l)}) \times \mathbf{S}(\boldsymbol{\omega}^{(k+1)} \ldots \boldsymbol{\omega}^{(k+m)}, \mathbf{V}^{(l+1)} \ldots \mathbf{V}^{(l+n)}). \tag{3.10}$$

3.2.4 Transformation Laws

An important property of these above mentioned mathematical objects is how their components change under a general coordinate transformation. Therefore we can consider two sets of coordinate systems denoted by $\{x^i\}$ and $\{x^{i'}\}$. We can then choose to work with the coordinate basis for $\mathbf{T}_P$ and define [15]

$$\mathbf{e}_{(i)} = \frac{\partial}{\partial x^i}, \tag{3.11}$$

$$\boldsymbol{\theta}^{(i)} = \mathrm{d}x^i. \tag{3.12}$$

The coordinate bases of the different coordinate systems $\{x^i\}$ and $\{x^{i'}\}$ are then related by the chain rule

$$\mathbf{e}_{(i')} = \frac{\partial x^i}{\partial x^{i'}} \mathbf{e}_{(i)}, \tag{3.13}$$

$$\boldsymbol{\theta}^{(i')} = \frac{\partial x^{i'}}{\partial x^i} \boldsymbol{\theta}^{(i)}. \tag{3.14}$$

Note that we are using Einstein's summation convention. To visualise this a bit more, we can introduce the transformation tensors $\Lambda^i_{i'}$ and $\Lambda^{i'}_i$ by

$$\Lambda^i_{\;i'} = \frac{\partial x^i}{\partial x^{i'}} \tag{3.15}$$

$$\Lambda^{i'}_{\;i} = \frac{\partial x^{i'}}{\partial x^i} \tag{3.16}$$

One can now derive the transformation law for the components of a vector $\mathbf{V}$ or a dual vector ω when going from one coordinate system $\{x^i\}$ to another $\{x^{i'}\}$:

$$\mathbf{V} = V^i \mathbf{e}_{(i)} = V^{i'} \mathbf{e}_{(i')}, \tag{3.17}$$

$$V^{i'} = \Lambda^{i'}_{\;i} V^i, \tag{3.18}$$

and

$$\boldsymbol{\omega} = \omega_i \boldsymbol{\theta}^{(i)} = \omega_{i'} \boldsymbol{\theta}^{(i')}, \tag{3.19}$$

$$\omega_{i'} = \Lambda^i_{\;i'} \omega_i, \tag{3.20}$$

where we used the fact that the vector $\mathbf{V}$ and the dual vector ω are coordinate independent. We can now write down the most general transformation law of an arbitrary tensor with k upper indices and l lower indices:

$$T^{i'_1 i'_2 \dots i'_k}_{\quad j'_1 j'_2 \dots j'_l} = \Lambda^{i'_1}_{\;i_1} \Lambda^{i'_2}_{\;i_2} \dots \Lambda^{i'_k}_{\;i_k} \Lambda^{j_1}_{\;j'_1} \Lambda^{j_2}_{\;j'_2} \dots \Lambda^{j_l}_{\;j'_l} T^{i_1 i_2 \dots i_k}_{\quad j_1 j_2 \dots j_l}. \tag{3.21}$$

This transformation law (3.21) is such a fundamental equation that it is sometimes used to define a tensor.

3.2.5 The Metric

The most famous tensor associated with a manifold is the metric. Being so fundamental, we will spend an entire section on this object. The metric encodes the local geometry of a manifold and provides a measure of distance on this manifold. That is why we use the symbol of a line element ds^2 for the metric:

$$ds^2 = g_{ij}\,\mathrm{d}x^i \mathrm{d}x^j. \tag{3.22}$$

Being a $(0, 2)$-tensor—having two lower indices—it acts on two vectors to yield a real number. This operation is the generalised inner product (or dot product):

$$ds^2(\mathbf{V}, \mathbf{W}) = g_{ij} V^i W^j. \tag{3.23}$$

The norm of a vector can also be defined as the inner product with itself:

$$\|\mathbf{V}\| = ds^2(\mathbf{V}, \mathbf{V}) = g_{ij} V^i V^j, \tag{3.24}$$

and if we compare Eq. (3.5) with Eq. (3.24), we notice a very useful property of the metric tensor:

$$\|\mathbf{V}\| = V^i V_i = g_{ij} V^i V^j. \tag{3.25}$$

Together with its inverse g^{ij}, which is defined by the equation $g_{ij}g^{jk} = g^{kl}g_{li} = \delta_i^k$, we can use the components of the metric to raise and lower indices of tensors:

$$g_{ij}V^j = V_i, \tag{3.26}$$

$$g^{ij}V_i = V^j. \tag{3.27}$$

The metric ds^2 only depends on the background manifold in which we are working (sphere, torus...). Its components, however, are also subject to the coordinates in which we are working. Since we will need it later on, we will give here some examples on how the components of the metric change with the coordinate system. We will express the metric of the well known Euclidean "flat" space $\mathbb{R}^3$ in three different coordinate systems: Cartesian coordinates, cylindrical coordinates and spherical coordinates. The metric (line element) of flat space in Cartesian coordinates is quite straightforward:

$$ds^2 = dx^2 + dy^2 + dz^2 = \delta_{ij}\,dx^i dx^j. \tag{3.28}$$

A (0,2)-tensor is not the same thing as a matrix.* Although it does not make a difference in the Euclidean case, it makes no sense to write this as:

$$g_{ij} = \begin{pmatrix} 1 & 0 & 0 \\ 0 & 1 & 0 \\ 0 & 0 & 1 \end{pmatrix} \tag{3.29}$$

Instead, let us approach it as an honest $(0,2)$-tensor with elements $g_{ii} = 1$ and $g_{ij} = 0$, for $i \neq j$. Eq. (3.28) can now be used in combination with Eq. (3.21) to express the components of the metric in other coordinate systems. Let's start with the cylindrical coordinates, $\{x^{i'}\} = \{\rho, \phi, z\}$:

$$g_{i'j'} = \Lambda^i_{\ i'}\Lambda^j_{\ j'}g_{ij}. \tag{3.30}$$

First, we will have to calculate the components of $\Lambda^i_{\ i'}$: To that aim, we express the relation between both coordinate systems and differentiate this according to Eq. (3.15):

$$x = \rho\cos\phi,$$
$$y = \rho\sin\phi, \tag{3.31}$$
$$z = z.$$

The components of the transformation tensor $\Lambda^i_{\ i'}$ are then given by:

$$\Lambda^x_{\ \rho} = \cos\phi, \qquad \Lambda^x_{\ \phi} = -\rho\sin\phi, \qquad \Lambda^x_{\ z} = 0,$$
$$\Lambda^y_{\ \rho} = \sin\phi, \qquad \Lambda^y_{\ \phi} = \rho\cos\phi, \qquad \Lambda^y_{\ z} = 0, \tag{3.32}$$
$$\Lambda^z_{\ \rho} = 0, \qquad \Lambda^z_{\ \phi} = 0, \qquad \Lambda^z_{\ z} = 1.$$

We are now fully equipped to calculate the components of the metric tensor in the new coordinate system. We write out the first two components to get acquainted with the summation

---

*Only a $(1,1)$-tensor can by visualised as a matrix.

convention:

$$
\begin{aligned}
g_{\rho\rho} &= \Lambda^x{}_\rho \Lambda^x{}_\rho \delta_{xx} + \Lambda^x{}_\rho \Lambda^y{}_\rho \delta_{xy} + \Lambda^x{}_\rho \Lambda^z{}_\rho \delta_{xz} \\
&\quad + \Lambda^y{}_\rho \Lambda^x{}_\rho \delta_{yx} + \ldots + \Lambda^z{}_\rho \Lambda^z{}_\rho \delta_{zz} \\
&= \Lambda^x{}_\rho \Lambda^x{}_\rho + \Lambda^y{}_\rho \Lambda^y{}_\rho + \Lambda^z{}_\rho \Lambda^z{}_\rho \\
&= 1,
\end{aligned}
\tag{3.33}
$$

$$
\begin{aligned}
g_{\rho\phi} &= \Lambda^x{}_\rho \Lambda^x{}_\phi \delta_{xx} + \Lambda^x{}_\rho \Lambda^y{}_\phi \delta_{xy} + \Lambda^x{}_\rho \Lambda^z{}_\phi \delta_{xz} \\
&\quad + \Lambda^y{}_\rho \Lambda^x{}_\phi \delta_{yx} + \ldots + \Lambda^z{}_\rho \Lambda^z{}_\phi \delta_{zz} \\
&= \Lambda^x{}_\rho \Lambda^x{}_\phi + \Lambda^y{}_\rho \Lambda^y{}_\phi + \Lambda^z{}_\rho \Lambda^z{}_\phi \\
&= 0.
\end{aligned}
\tag{3.34}
$$

This can be repeated for the other components resulting in:

$$
\begin{array}{lll}
g_{\rho\rho} = 1, & g_{\rho\phi} = 0, & g_{\rho z} = 0, \\
g_{\phi\rho} = 0, & g_{\phi\phi} = \rho^2, & g_{\phi z} = 0, \\
g_{z\rho} = 0, & g_{z\phi} = 0, & g_{zz} = 1.
\end{array}
\tag{3.35}
$$

The metric in cylindrical coordinates can thus be written as

$$
ds^2 = d\rho^2 + \rho^2 \, d\phi^2 + dz^2.
\tag{3.36}
$$

The same line of reasoning can be applied to the spherical case: $\{x^{i'}\} = \{r, \theta, \phi\}$, yielding:

$$
\begin{aligned}
x &= r \sin\theta \cos\phi, \\
y &= r \sin\theta \sin\phi, \\
z &= r \cos\theta.
\end{aligned}
\tag{3.37}
$$

with a transformation tensor Λ^i_j:

$$
\begin{array}{lll}
\Lambda^x{}_r = \sin\theta \cos\phi, & \Lambda^x{}_\phi = -r \sin\theta \sin\phi, & \Lambda^x{}_\theta = r \cos\theta \cos\phi, \\
\Lambda^y{}_r = \sin\theta \sin\phi, & \Lambda^y{}_\phi = r \sin\theta \cos\phi, & \Lambda^y{}_\theta = r \cos\theta \sin\phi, \\
\Lambda^z{}_r = \cos\theta, & \Lambda^z{}_\phi = 0, & \Lambda^z{}_\theta = -r \sin\theta.
\end{array}
\tag{3.38}
$$

and finaly:

$$
\begin{array}{lll}
g_{rr} = 1, & g_{r\phi} = 0, & g_{r\theta} = 0, \\
g_{\phi r} = 0, & g_{\phi\phi} = r^2 \sin^2\theta, & g_{\phi\theta} = 0, \\
g_{\theta r} = 0, & g_{\theta\phi} = 0, & g_{\theta\theta} = r^2.
\end{array}
\tag{3.39}
$$

The metric in spherical coordinates is thus given by:

$$
ds^2 = dr^2 + r^2 \left(d\theta^2 + \sin^2\theta \, d\phi^2 \right),
\tag{3.40}
$$

3.2.6 Differential Operators

In the local perspective, Maxwell's equations are written using the divergence and curl operators. It is therefore indispensable to have a general tensorial notation of these operators. First, we have to generalise the familiar partial derivative. Working on a general metric, we can introduce the *covariant derivative*. This derivative takes into account that basis vectors do not have to be constant throughout space (as Cartesian coordinates in Euclidean space). The derivative of a vector $\mathbf{V} = V^i \mathbf{e}_i$ can then be written as:

$$\frac{\partial \mathbf{V}}{\partial x^i} = \frac{\partial V^j}{\partial x^i} \mathbf{e}_j + V^j \frac{\partial \mathbf{e}_j}{\partial x^i}. \tag{3.41}$$

The covariant derivative, symbolically abbreviated by ∇_i is thus given by:

$$\nabla_i V^j = \frac{\partial V^j}{\partial x^i} + \Gamma^j_{ik} V^k. \tag{3.42}$$

where we introduced a so-called connection Γ^k_{ij}, quantifying the derivative of the basis vectors:

$$\frac{\partial \mathbf{e}_j}{\partial x^i} = \Gamma^k_{ij} \mathbf{e}_k. \tag{3.43}$$

Another notation convention is usually introduced to abbreviate the partial derivative and the covariant derivative:

$$\frac{\partial V^j}{\partial x^i} = V^j_{,i} \tag{3.44}$$

$$\nabla_i V^j = V^j_{;i} \tag{3.45}$$

The divergence of a vector $\mathbf{V}$ is defined as:

$$\nabla_i V^i = V^i_{;i} = \frac{\partial V^i}{\partial x^i} + \Gamma^i_{ik} V^k = V^i_{,i} + \Gamma^i_{jk} V^k. \tag{3.46}$$

In the case of Cartesian coordinates in a Euclidean space, Eq. (3.43) yields $\Gamma^i_{jk} = 0$, and so Eq. (3.46) corresponds with our usual definition of the divergence. If we choose to work with the metric-compatible, torsion-free connection, also known as the Christoffel connection $\Gamma^i_{jk} = \frac{1}{2} g^{il}(\frac{\partial g_{lj}}{\partial x^k} + \frac{\partial g_{lk}}{\partial x^j} - \frac{\partial g_{jk}}{\partial x^l})$, this divergence can also be written as [1]

$$\nabla_i V^i = \frac{1}{\sqrt{g}} \frac{\partial \left(\sqrt{g} V^i \right)}{\partial x^i}. \tag{3.47}$$

The curl of a vector $\mathbf{V}$ can be written as the vector product of the ∇-symbol with $\mathbf{V}$. On the background of an abritrary metric, vector products are calculated using the Levi-Civita tensor ϵ^{ijk}:

$$\mathbf{V} \times \mathbf{W} = \epsilon^{ijk} V_j W_k \mathbf{e}_i. \tag{3.48}$$

The components of the Levi-Civita tensor are defined as [15]

$$\epsilon^{ijk} = \pm \frac{1}{\sqrt{g}} [i \, j \, k], \tag{3.49}$$

where we have to choose the minus sign when considering a left-handed coordinate system.

In previous equation g represents the determinant of the metric tensor $g = |g_{ij}|$ and $[i\,j\,k]$ is the permutation symbol, defined as:

$$[i\,j\,k] = \begin{cases} +1 & \text{if } i\,j\,k \text{ is an even permutation of 1 2 3,} \\ -1 & \text{if } i\,j\,k \text{ is an odd permutation of 1 2 3,} \\ 0 & \text{otherwise.} \end{cases} \tag{3.50}$$

We can now return to the definiton of the curl in the tensorial language:

$$\nabla \times \mathbf{V} = \epsilon^{ijk} \nabla_j V_k \mathbf{e}_i. \tag{3.51}$$

When we write out this summation, it becomes clear that the terms involving the connections cancel and we can thus use the partial derivative instead of the covariant one.

$$\nabla \times \mathbf{V} = \epsilon^{ijk} \frac{\partial V_k}{\partial x^j} \mathbf{e}_i. \tag{3.52}$$

As was the case with the divergence, this definition of the curl corresponds to the usual definition in a Cartesian coordinate system in Euclidean space.

Herewith, we have introduced all the necessary tools to tackle Maxwell's equations and write them down in manifolds with an arbitrary metric.

3.3 Transformation Optics

3.3.1 Geometries or Media

Reality is highly subject to the observer's point of view. Special relativity, e.g., introduced time dilatation and length contraction between two observers moving with respect to each other. Mathematically, a point of view is defined by a coordinate system. In Fig. 3.4, we demonstrate how a straight line in a Cartesian coordinate system is deformed in a curvilinear coordinate system.

In this section, we will rewrite free-space Maxwell's equations in arbitrary coordinates and show that this set corresponds to the macroscopic Maxwell's equations of electromagnetic fields propagating inside a material on the background of a right-handed Cartesian coordinate system. In the absence of charges and currents, Maxwell's equations are given by:

$$\nabla \cdot \mathbf{E} = 0, \qquad\qquad \nabla \cdot \mathbf{B} = 0,$$
$$\nabla \times \mathbf{E} = -\frac{\partial \mathbf{B}}{\partial t}, \qquad\qquad \nabla \times \mathbf{B} = \frac{1}{c^2} \frac{\partial \mathbf{E}}{\partial t}. \tag{3.53}$$

(a)   (b)
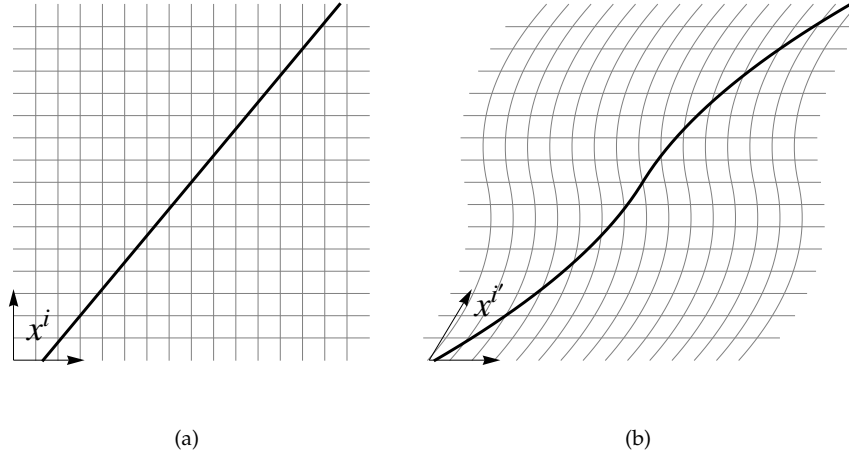
Figure 3.4: A straight line $y = ax + b$ in two different coordinate systems: (a) the traditional Cartesian coordinates $\{x^i\} = (x, y)$ and (b) a deformed coordinate system $\{x^{i'}\} = (x', y')$, with $x' = f(x, y)$ and $y' = y$.

Using Eq. (3.47) and Eq. (3.52), we can transform these equations to a general manifold with arbitrary coordinates, specified by the metric components g_{ij}:

$$\frac{1}{\sqrt{g}} \frac{\partial\left(\sqrt{g}E^i\right)}{\partial x^i} = 0, \qquad\qquad \frac{1}{\sqrt{g}} \frac{\partial\left(\pm\sqrt{g}B^i\right)}{\partial x^i} = 0,$$

$$\epsilon^{ijk}\frac{\partial E_k}{\partial x^j} = -\frac{\partial\left(\pm B^i\right)}{\partial t}, \qquad\qquad \epsilon^{ijk}\frac{\partial\left(\pm B_k\right)}{\partial x^j} = \frac{1}{c^2}\frac{\partial E^i}{\partial t}. \tag{3.54}$$

The $\pm$-signs accompany the components of **B**, due to the fact that this is a pseudo-vector that changes its sign in a left-handed coordinate system. We will apply now some manipulations to this equation: the inverse metric can be used to lower all indices, according to Eq. (3.27), the Levi-Civita tensor can be replaced by Eq. (3.49) and in vacuum $B^i = \mu_0 H^i$, which yields

$$\frac{1}{\sqrt{g}} \frac{\partial\left(\sqrt{g}g^{ij}E_j\right)}{\partial x^i} = 0, \qquad\qquad \frac{1}{\sqrt{g}} \frac{\partial\left(\pm\sqrt{g}g^{ij}\mu_0 H_j\right)}{\partial x^i} = 0,$$

$$\pm[i\,j\,k]\frac{\partial E_k}{\partial x^j} = -\frac{\partial\left(\pm\sqrt{g}g^{ij}\mu_0 H_j\right)}{\partial t}, \qquad \pm[i\,j\,k]\frac{\partial\mu_0 H_k}{\partial x^j} = \epsilon_0\mu_0\frac{\partial\left(\pm\sqrt{g}g^{ij}E_j\right)}{\partial t}, \tag{3.55}$$

where we assumed $\sqrt{g}$ to be time-independent. Both $\pm$-signs in these equations are negative at the same time, when the coordinate system is left-handed, and so they cancel each other.

In the next step, we write down the macroscopic Maxwell's equations in a dielectric:

$$\nabla \cdot \mathbf{D} = 0, \qquad\qquad\qquad \nabla \cdot \mathbf{B} = 0,$$

$$\nabla \times \mathbf{E} = -\frac{\partial \mathbf{B}}{\partial t}, \qquad\qquad \nabla \times \mathbf{H} = \frac{\partial \mathbf{D}}{\partial t}, \tag{3.56}$$

and expand these vectorial equations in right-handed Cartesian coordinates system:

$$\frac{\partial D^i}{\partial x^i} = 0, \qquad\qquad \frac{\partial B^i}{\partial x^i} = 0,$$

$$[i\,j\,k]\frac{\partial E_k}{\partial x^j} = -\frac{\partial B^i}{\partial t}, \qquad\qquad [i\,j\,k]\frac{\partial H_k}{\partial x^j} = \frac{\partial D^i}{\partial t}, \qquad (3.57)$$

In the last step, we compare Eq. (3.55) and Eq. (3.57) and notice that they can be converted into each other if we use the following constitutive equations:

$$D^i = \epsilon_0 \epsilon^{ij} E_j, \qquad\qquad (3.58)$$

$$B^i = \mu_0 \mu^{ij} H_j, \qquad\qquad (3.59)$$

with

$$\epsilon^{ij} = \mu^{ij} = \sqrt{g} g^{ij}. \qquad\qquad (3.60)$$

This previous result beautifully indicates the similarity of the effect of either geometry or material: Maxwell's equations in vacuum on a nontrivial background g_{ij} are equivalent to the macroscopic Maxwell's equations in a dielectric in a right-handed Cartesian coordinate system, if the constitutive parameters of the dielectric obey Eq. (3.60). We have thus demonstrated the equivalence between two different spaces — two different points of view: the *electromagnetic space*, which is empty and characterised by the metric components g_{ij}, and the *physical space*, which contains a dielectric specified by Eq. (3.60) on a right-handed Cartesian coordinate system.

Although the metric components of the electromagnetic space g_{ij} can refer to a general curved geometry with arbitrary coordinates, we will usually consider the conventional flat manifold background, which is the same as in the physical space, such that the nontrivial g_{ij}-components are merely the result of expressing flat space-time in an unusual coordinate system. Media that implement such a transformation of coordinates are therefore refered to as *transformation media*.[*]

3.3.2 Two Different Points of View

The invisibility cloak is probably the most instructive example of a transformation medium. An object becomes visible when the light beam is reflected or scattered on it towards the observer. To make something invisible, we should shield it from electromagnetic radiation. Of course, the cloak itself should also be invisible and may not leave a shadow at its backside. In conclusion, we need some kind of device that guides the electromagnetic waves around an object, without them to be aware of it.

Let us now approach this problem within the framework of transformation media. In the electromagnetic space $\{x^{i'}\}$, the coordinate lines are undistorted, which is shown in Fig. 3.5. The circle indicates the region where we will implement the transformation medium. Outside this region, the electromagnetic space is the same as the physical space: $\{x^{i'}\} = \{x^i\}$. Inside the circular region, the electromagnetic coordinates are related to the physical ones through a nontrivial coordinate transformation: $\{x^{i'}\} = \{f(x^i)\}$.
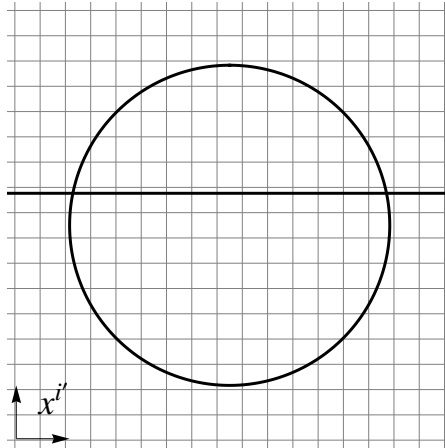
Figure 3.5: Coordinate grid of the electromagnetic space. Since we do not want the electromagnetic waves to be aware of any perturbation, the metric of this space is given by $ds^2 = \delta_{i'j'} dx^{i'} dx^{j'}$. The black line shows the possible trajectory of a light ray and the circle indicates the region where we will apply a coordinate transformation.
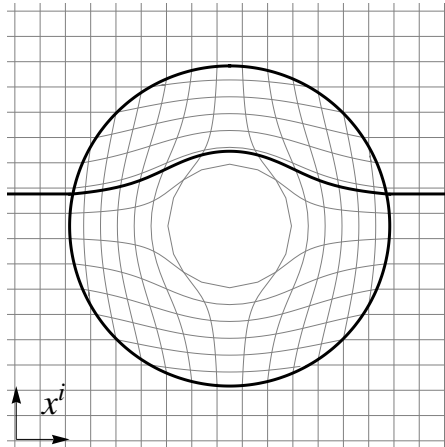
Figure 3.6: In a right-handed coordinate system, the straight lines of Fig. 3.5 are curved inside the circle. Every possible ray is bent around an inner hole which has become invisible. After passing the invisible hole, every ray returns to its position as if the space was empty.

The metric of this space is given by:

$$ds^2 = g_{i'j'} dx^{i'} dx^{j'} = \delta_{i'j'} dx^{i'} dx^{j'}. \tag{3.61}$$

To have a better insight on how the electromagnetic waves will propagate in our reality, we can rewrite these metric components in a right-handed Cartesian coordinate system:

$$ds^2 = g_{ij} dx^i dx^j. \tag{3.62}$$

---

*Since we want to make transformation media with finite extent, these media will implement *local* coordinate transformations.
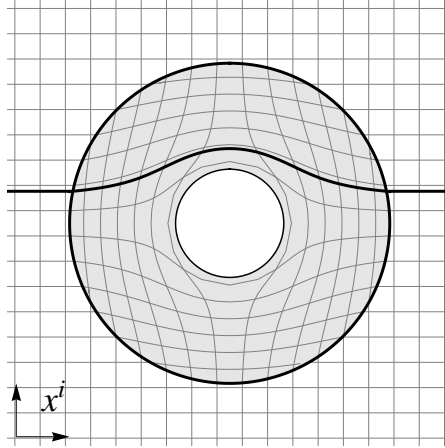
Figure 3.7: The coordinate transformation can from Fig. 3.6 be implemented by means of a dielectric (gray) whose constitutive parameters are given by Eq. (3.60).

These components can be calculated using the tensor transformation law, Eq. (3.21):

$$g_{ij} = \Lambda^{i'}{}_{i}\Lambda^{j'}{}_{j}g_{i'j'} = \Lambda^{i'}{}_{i}\Lambda^{j'}{}_{j}\delta_{i'j'}, \tag{3.63}$$

where $\Lambda^{i'}{}_{i}$ is defined as in Eq. (3.16). When we choose the coordinates $\{x^{i'}\}$ in a clever way, the grid will bend around a hole in the physical space $\{x^{i'}\}$. This is shown in Fig. 3.6.

We can approach this from the material's perspective in the physical space. Eq. (3.60) offers the recipe through which we can build this geometry with a transformation medium, as illustrated in Fig. 3.7. Something positioned inside the inner circle is not accessible for electromagnetic waves.

3.3.3 General Transformation Media

Having become acquainted with the principles of transformation optics, we can further generalise it. In Sec. 3.3.1, we assumed electromagnetic space to be empty and that physical space was described with Cartesian coordinates. In some cases, these assumptions will be inadequate: when we want to design a super antenna or cloak something under water, the electromagnetic space will certainly not be empty, and most cloaking problems have circular symmetry and are better descibed in cylindrical or spherical coordinates. In the following calculations will remove the previous assumptions. The reasoning is, however, the same as in Sec. 3.3.1.

In the electromagnetic space, we denote the fields with an accent. Formulated in terms of *free* charge $\tilde{\rho}$ and current $\tilde{\mathbf{j}}$, Maxwell's equations are given by:

$$\nabla \cdot \tilde{\mathbf{D}} = \tilde{\rho}, \qquad\qquad \nabla \cdot \tilde{\mathbf{B}} = 0,$$

$$\nabla \times \tilde{\mathbf{E}} = -\frac{\partial \mathbf{B}}{\partial t}, \qquad\qquad \nabla \times \tilde{\mathbf{H}} = \frac{1}{c^2}\frac{\partial \tilde{\mathbf{D}}}{\partial t} + \mu_0\tilde{\mathbf{j}}. \tag{3.64}$$

We can write these equations in terms of general metric components g_{ij}, as in Eq. (3.55):

$$\frac{1}{\sqrt{g}}\frac{\partial\left(\sqrt{g}g^{ij}\tilde{D}_j\right)}{\partial x^i} = \tilde{\rho}, \qquad \frac{1}{\sqrt{g}}\frac{\partial\left(\pm\sqrt{g}g^{ij}\tilde{B}_j\right)}{\partial x^i} = 0,$$

$$\pm[i\,j\,k]\frac{\partial\tilde{E}_k}{\partial x^j} = -\frac{\partial\left(\pm\sqrt{g}g^{ij}\tilde{B}_j\right)}{\partial t}, \qquad \pm[i\,j\,k]\frac{\partial\left(\pm\tilde{H}_k\right)}{\partial x^j} = \epsilon_0\mu_0\frac{\partial\left(\sqrt{g}g^{ij}\tilde{D}_j\right)}{\partial t} + \mu_0\tilde{j}^{\,i}. \qquad (3.65)$$

We notice again that the ±-signs are simultaneously negative and can thus be omitted.

Now we would like to read these equations as macroscopic Maxwell's equations in specified coordinates, e.g., spherical coordinates, determined by the metric components in Eq. (3.39). In physical space, the fields have no tilde (˜) and the metric components are labeled as γ_{ij}, yielding:

$$\frac{1}{\sqrt{\gamma}}\frac{\partial\left(\sqrt{\gamma}D^i\right)}{\partial x^i} = \rho, \qquad \frac{1}{\sqrt{\gamma}}\frac{\partial\left(\pm\sqrt{\gamma}B^i\right)}{\partial x^i} = 0,$$

$$\pm[i\,j\,k]\frac{\partial E_k}{\partial x^j} = -\frac{\partial\left(\pm\sqrt{\gamma}B^i\right)}{\partial t}, \qquad \pm[i\,j\,k]\frac{\partial\left(\pm H_k\right)}{\partial x^j} = \epsilon_0\mu_0\frac{\partial\left(\sqrt{\gamma}D^i\right)}{\partial t} + \mu_0 j^i. \qquad (3.66)$$

Eq. (3.65) and Eq. (3.66) can be converted into each other when we apply relations:

$$D^i = \frac{\sqrt{g}}{\sqrt{\gamma}}g^{ij}\tilde{D}_j, \qquad\qquad B^i = \mu_0\frac{\sqrt{g}}{\sqrt{\gamma}}g^{ij}\tilde{B}_j,$$

$$\rho = \frac{\sqrt{g}}{\sqrt{\gamma}}\tilde{\rho}, \qquad\qquad j^i = \frac{\sqrt{g}}{\sqrt{\gamma}}\tilde{j}^{\,i}. \qquad (3.67)$$

In electromagnetic space, the constitutive relations are imposed by the medium in which we are working, e.g., water in the case of under water cloaking. Generally, they are given by:

$$\tilde{D}_j = \epsilon_0\tilde{\epsilon}_j^{\ k}E_k,$$

$$\tilde{B}_j = \mu_0\tilde{\mu}_j^{\ k}H_k. \qquad (3.68)$$

In conclusion, we can perform a general coordinate transformation from electromagnetic space, defined by Eq. (3.68), when we insert a material in physical space whose properties are given by:

$$D^i = \epsilon_0\epsilon^{ij}E_j, \qquad\qquad B^i = \mu_0\mu^{ij}H_j,$$

$$\rho = \frac{\sqrt{g}}{\sqrt{\gamma}}\tilde{\rho}, \qquad\qquad j^i = \frac{\sqrt{g}}{\sqrt{\gamma}}\tilde{j}^{\,i},$$

$$\epsilon^{ij} = \frac{\sqrt{g}}{\sqrt{\gamma}}g^{ik}\epsilon_k^{\ j}, \qquad\qquad \mu^{ij} = \frac{\sqrt{g}}{\sqrt{\gamma}}g^{ik}\mu_k^{\ j}. \qquad (3.69)$$

Since these formula might appear somewhat overwhelming at first sight, let us review what we have done in this section. In Sec. 3.3.1, we demonstrated how Maxwell's equations in

vacuum, written in terms of general metric components g_{ij}, are equivalent to the macroscopic equations inside a dielectric with constitutive parameters given by Eq. (3.60), expanded in a right-handed Cartesian coordinate system. In this way, we introduced the equivalence between an electromagnetic space, which is empty on a nontrivial background, and a physical space, which is filled with a material on a trivial background, and demonstrated these concepts with the example of a cloak in Sec. 3.3.2. We generalised the formalism in two ways: the electromagnetic space should not be empty at all and the physical space can be expressed in more general coordinates. This general transformation generates constitutive equations as given in Eq. (3.69). Note how this formula also incorporates Eq. (3.60) with $\tilde{\varepsilon}_j^{\ k} = \tilde{\mu}_j^{\ k} = \delta_j^{\ k}$ and $\tilde{\rho} = \tilde{\mathbf{j}} = 0$.

3.4 Applications

3.4.1 The Invisibility Cloak

In Sec. 3.3.2, we already introduced the idea behind an invisiblity cloak. The actual material properties can be calculated with the formulae of Sec. 3.3.3, since the problem is formulated much more elegant in non-Cartesian coordinates. Consider to coordinate systems: (r, θ, ϕ) in physical space and (r', θ', ϕ') in electromagnetic space. The general coordinate transformation between both spaces has spherical symmetry and can thus be characterised by a transformation on the radial coordinate $f : [R_1, R_2] \to \mathbb{R}^+ : r \mapsto r'$. The angular coordinates are identical in the two systems.

$$r' = f(r), \tag{3.70}$$
$$\theta' = \theta, \tag{3.71}$$
$$\phi' = \phi. \tag{3.72}$$

To achieve perfect invisiblity, this function f will have to meet two boundary conditions:

$$f(R_1) = 0, \tag{3.73}$$
$$f(R_2) = R_2. \tag{3.74}$$

Eq. (3.73) maps the shell (surface of a sphere) of radius R_1 in physical space on the origin of the electromagnetic space. Since there is nothing "behind the origin" in the electromagnetic space, this formula imposes a natural boundary for the electromagnetic waves at the physical radius R_1. Eq. (3.74) maps the shell of radius R_2 on the same shell in the electromagnetic space. Outside the cloaking device, electromagnetic and physical space coincide and so this formula guarantees a smooth (continuous) transition at the outer boundary R_2. Together, Eq. (3.73) and Eq. (3.74) map the physical space $r : R1 \to \infty$ on the entire electromagnetic space $r' : 0 \to \infty$. The actual transformation function f is not uniquely determined. Every continuous function complying with Eq. (3.73) and Eq. (3.74) will render an invisible hole. For the sake of simplicity, we will use a linear function f, shown in Fig. 3.8 defined by:

$$f : [R_1, R_2] \to \mathbb{R}^+ : r \mapsto r' = \frac{R_2}{R_2 - R_1}(r - R_1). \tag{3.75}$$
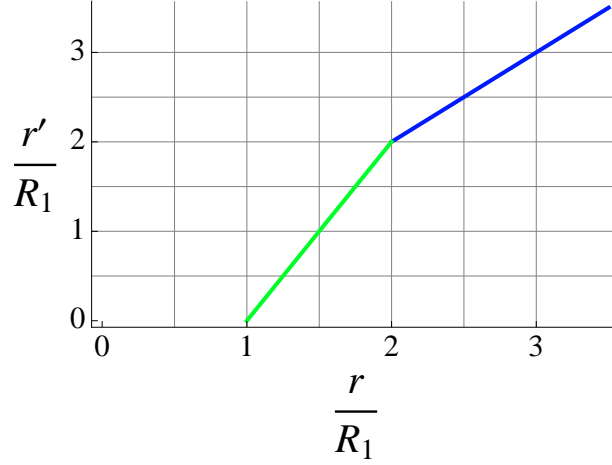
Figure 3.8: The linear transformation function f (green), defined in Eq. (3.75), maps the interval $[R_1, R_2]$ in the physical space r on the interval $[0, R_2]$ in the electromagnetic space r'. In this example, the outer radius R_2 equals two times the inner radius R_1. At this outer boundary, f is continuously matched with the surrounding space (blue), where $r' = r$. The corresponding Cartesian grid is shown in Fig. 3.6.

As we want to design a cloak in vacuum and express it in spherical coordinates, we insert following parameters in Eq. (3.69): the metric in physical space γ_{ij} is given by Eq. (3.39) and the electromagnetic parameters are: $\tilde{\rho} = \tilde{\mathbf{j}} = 0$, $\tilde{\epsilon}_j^{\ k} = \tilde{\mu}_j^{\ k} = \delta_j^{\ k}$. The most challenging problem is to calculate g_{ij}. The metric of electromagnetic space is given by:

$$ds^2 = g_{i'j'} \mathrm{d}x^{i'} \mathrm{d}x^{j'}, \tag{3.76}$$

$$= \mathrm{d}r'^2 + r'^2 \left(\mathrm{d}\theta'^2 + \sin^2 \theta' \, \mathrm{d}\phi'^2 \right). \tag{3.77}$$

Expressed in terms of the physical coordinates r, θ, ϕ:

$$ds^2 = g_{ij} \mathrm{d}x^i \mathrm{d}x^j, \tag{3.78}$$

$$= f'(r)^2 \mathrm{d}r^2 + f(r)^2 \left(\mathrm{d}\theta^2 + \sin^2 \theta \, \mathrm{d}\phi^2 \right), \tag{3.79}$$

and so the g_{ij}-components are given by:

$$\begin{aligned} g_{rr} &= f'(r)^2, & g_{r\theta} &= 0, & g_{r\phi} &= 0, \\ g_{\theta r} &= 0, & g_{\theta\theta} &= f(r)^2, & g_{\theta\phi} &= 0, \\ g_{\phi r} &= 0, & g_{\phi\theta} &= 0, & g_{\phi\phi} &= f(r)^2 \sin^2 \theta. \end{aligned} \tag{3.80}$$

The contravariant components g^{ij} are consequently given by:

$$\begin{aligned} g^{rr} &= \frac{1}{f'(r)^2}, & g^{r\theta} &= 0, & g^{r\phi} &= 0, \\ g^{\theta r} &= 0, & g^{\theta\theta} &= \frac{1}{f(r)^2}, & g^{\theta\phi} &= 0, \\ g^{\phi r} &= 0, & g^{\phi\theta} &= 0, & g^{\phi\phi} &= \frac{1}{f(r)^2 \sin^2 \theta}. \end{aligned} \tag{3.81}$$

Wrapping up all these ingredients, we are now able to use Eq. (3.69) and derive the constitutive parameters:

$$\epsilon^{ij} = \mu^{ij} = \frac{\sqrt{g}}{\sqrt{\gamma}} g^{ik} \epsilon_k^{\ j}, \tag{3.82}$$

$$= \frac{f'(r)f^2(r)\sin\theta}{r^2 \sin\theta} g^{ij}. \tag{3.83}$$

Since $\mu^{ij} = \epsilon^{ij}$, we will only consider the permittivity in the equations to come. The same formulae are valid for the permeability:

$$
\begin{array}{lll}
\epsilon^{rr} = \dfrac{f^2(r)}{f'(r)r^2}, & \epsilon^{r\theta} = 0, & \epsilon^{r\phi} = 0, \\[2ex]
\epsilon^{\theta r} = 0, & g^{\theta\theta} = \dfrac{f'(r)}{r^2}, & \epsilon^{\theta\phi} = 0, \\[2ex]
\epsilon^{\phi r} = 0, & \epsilon^{\phi\theta} = 0, & \epsilon^{\phi\phi} = \dfrac{f'(r)}{r^2 \sin^2\theta}.
\end{array}
\tag{3.84}
$$

If we actually want to implement these tensor components, we should bear in mind that they are now defined on the background of γ_{ij} and that the actual physical quantities are given by the mixed tensor components $\epsilon^i_{\ j} = \epsilon^{ik}\gamma_{kj}$ and $\mu^i_{\ j} = \mu^{ik}\gamma_{kj}$, since they convert a vector into another vector. So finally, we arrive at the long awaited constitutive parameters of a spherical invisibility cloak:

$$
\begin{array}{lll}
\epsilon^r_{\ r} = \dfrac{f^2(r)}{f'(r)r^2}, & \epsilon^r_{\ \theta} = 0, & \epsilon^r_{\ \phi} = 0, \\[2ex]
\epsilon^\theta_{\ r} = 0, & \epsilon^\theta_{\ \theta} = f'(r), & \epsilon^\theta_{\ \phi} = 0, \\[2ex]
\epsilon^\phi_{\ r} = 0, & \epsilon^\phi_{\ \theta} = 0, & \epsilon^\phi_{\ \phi} = f'(r).
\end{array}
\tag{3.85}
$$

These components have been derived by Pendry *et al.* in Ref. [2]. Let us have a closer look at these parameters and insert the transformation function f, defined by Eq. (3.75). The nonzero components are given by:

$$
\begin{aligned}
\epsilon^r_{\ r} &= \frac{R_2}{R_2 - R_1} \frac{(r - R_1)^2}{r^2}, \\
\epsilon^\theta_{\ \theta} &= \frac{R_2}{R_2 - R_1}, \\
\epsilon^\phi_{\ \phi} &= \frac{R_2}{R_2 - R_1}.
\end{aligned}
\tag{3.86}
$$

These functions, shown in Fig. 3.9, indicate how the material parameters are highly dependent on the difference between the two radii R_1 and R_2: to cloak a volume with a small cloak ($R_2 - R_1 \ll R_1$), one needs to realise high $\epsilon^\theta_{\ \theta}$ and $\epsilon^\phi_{\ \phi}$ and a very low $\epsilon^r_{\ r}$. The same reasoning applies if one want to cloak irregular shapes [16, 17].

Another fundamental property of the cloak is the singularity at the inner boundary. Ideally, the radial component of the parameters ϵ and μ should be zero at R_1. This effect results from the fact
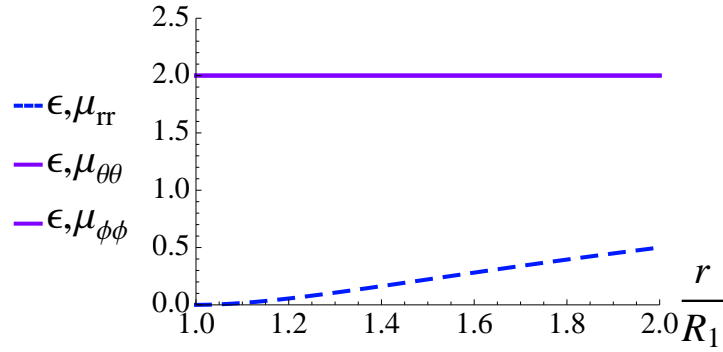
Figure 3.9: Material parameters constituting a spherical inivisibility cloak, defined by Eq. (3.75). The μ-components are identical to these from ϵ. By choosing a linear transformation function f, the θ and ϕ-components are constant. The radial component of the material's respons decreases towards the inner circle, where it becomes zero.
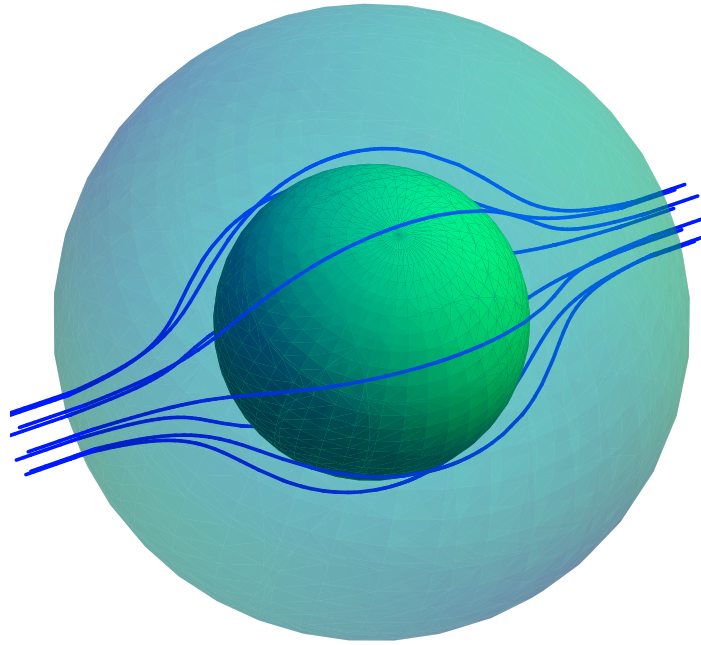
Figure 3.10: Three dimensional simulation on the propagation of light rays through a spherical invisibility cloak. The cloak, implementing the linear transformation function f as defined by Eq. (3.75), guides the rays around the inner sphere with radius R_1.

that we mapped the inner boundary in physical space on the origin in the electromagnetic space. In other words, a single point in electromagnetic space corresponds to a shell of radius R_1 in the physical space. This means that the electromagnetic waves should pass by a finite region in the

cloak in the same time interval as it would take to pass a single point in empty space. This time interval equals zero. To achieve perfect invisibility, the phase velocity inside the cloak should thus approach infinity, which is generated by zero $\epsilon^r_{\ r}$ and $\mu^r_{\ r}$. Ay, there's the rub: although phase velocities can become arbitrarily high, the group velocity—actually, the signal's velocity–is limited by the speed of light c [18]. This means that the group velocity v_g should significantly differ from the phase velocity v_f, which is only the case in the presence of high dispersion. The singularity in the profile of the constitutive parameters is thus not only difficult to realise with metamaterials, it also imposes drastical limits on the bandwith of the cloak. Currently, there is a lot of research to relax the constraints on the material parameters. The most promising idea is based on the use of non-Euclidean geometries to make regions invisible. This resulting cloaking device inhibits no singularity [19].

3.4.2 The Perfect Lens

The perfect lens can be seen as an important application of transformation optics. Although this device was already proposed by Veselago in 1968 [20], without the use of this new theory, it can be understood and generalised within the framework of transformation optics. The concept behind a perfect lens is a multi-valued coordinate transformation: one point in electromagnetic space corresponds with several points in physical space. Let us analyse this device with some inverse engineering: starting from the values of the ϵ and μ-components, we are searching for the equivalent coordinate transformation. A one-dimensional perfect lens is defined by the following material parameters:[20]

$$
\begin{aligned}
\epsilon^x_{\ x} &= -1, \\
\epsilon^y_{\ y} &= -1, \\
\epsilon^z_{\ z} &= -1.
\end{aligned}
\tag{3.87}
$$

Since this planar lens is designed to work in vacuum and can be most easily expressed in Cartesian coordinates, we can restrict ourselves to the constitutive parameters as given in Eq. (3.60). Consider now a one-dimensional coordinate transformation between two coordinate systems (x, y, z) and (x', y', z'):

$$
\begin{aligned}
x' &= f(x), \\
y' &= y, \\
z' &= z.
\end{aligned}
\tag{3.88}
$$

Similar to Sec. 3.4.1, we can derive the material parameters to implement such a continuous transformation:

$$
\begin{array}{lll}
\epsilon^x_{\ x} = \dfrac{1}{f'(x)}, & \epsilon^x_{\ y} = 0, & \epsilon^x_{\ z} = 0, \\
\epsilon^y_{\ x} = 0, & \epsilon^y_{\ y} = f'(x), & \epsilon^y_{\ z} = 0, \\
\epsilon^z_{\ x} = 0, & \epsilon^z_{\ y} = 0, & \epsilon^z_{\ z} = f'(x).
\end{array}
\tag{3.89}
$$

These material parameters now equal those from the perfect lens, as defined in Eq. (3.87), if we assume a linear transformation function f whose slope equals -1:

$$x' = f(x) = -x + a, \tag{3.90}$$

with $a \in \mathbb{R}$. We can visualise the effect of the perfect lens in Fig. 3.11, where we have chosen $a = 0$. The blue lines indicate unperturbed electromagnetic space. The green line indicates the coordinate transformation that is implemented by the lens.
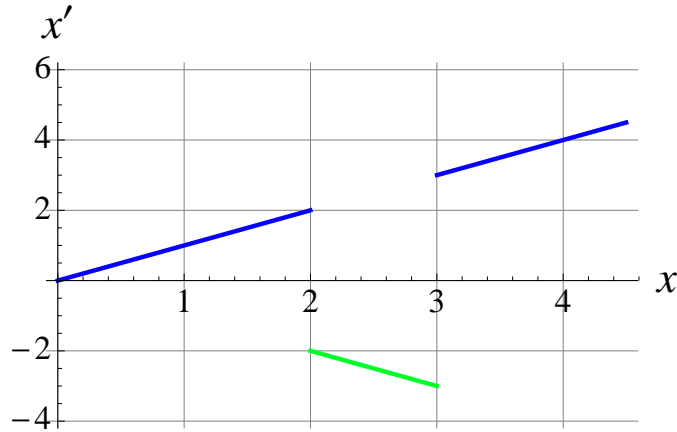
Figure 3.11: A representation of the in electromagnetic space of the effect of a superlens. The blue lines indicate the undisturbed vacuum (where $x' = x$), the green line implement the superlens.

Eq. (3.89) actually offers additional information: in a one-dimensional coordinate transformation, the material parameters are determinded by the slope of the function, the actual value of the function has no importance. This is certainly not true for a cylindrical or spherical transformation, as can be seen from Eq. (3.85). Bearing this in mind, we can give a different representation of Fig. 3.11, which is shown in Fig. 3.12, where we have shifted the curves untill they match at the boundaries. This figure is certainly easier to understand. The continuous coordinate transformation (the end points of the lens' transformation match with vacuum) turns the electromagnetic space multi-valued. The black, dashed lines indicate three different physical points, corresponding to one point in electromagnetic space: every point in the object space, positioned closed enough to the lens (at a distance closer than the total width of the lens) has two perfect images: one inside the lens, another one in the image space. We notice that this is exactly in agreement with what we have derived in Sec. 3.4.2

Transformation optics thus enables us to generalise Veselago's proposal to incorporate magnification [21] or make a higher dimensional analogue: a cylindrical [22] or spherical superlens [23].
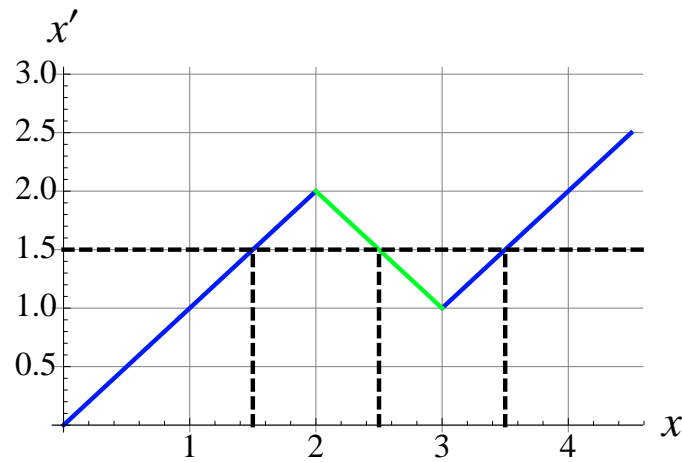
Figure 3.12: A more transparent representation of the superlens' effect. Since the material parameters in a one-dimensional transformation only depend on the slope of the function, we can shift the curves up and down untill they match at the transition zones.

3.5 Discussion

Transformation optics offers a new perspective on the interaction of light with complex media. It offers a very intuitive approach to solve problems far beyond the scope of traditional optics. It is important to realise the full potential of this technique. We derived the material parameters starting from Maxwell's equations. The technique is therefore valid beyond the range of geometrical optics. As a matter of fact, there are no constraints on the wavelength under consideration. This suggests that transformation optics could become a useful theory to design subwavelength optical components. The best example of this ability is the perfect lens. This extraordinary lens can be understood using transformation optics. The ideal Veselago lens indeed has an infinite resolution. Furthermore, we did not make any assumption on the field's polarisation. This is translated in the fact that $\epsilon = \mu$ in every direction. This constraint can be relaxed when designing the device for one single polarisation. As we will see later on, this will make some components of the ϵ and μ tensor unimportant.

Finally, it is also noteworthy that the transformation-optical technique is not limited to the control of the light's propagation. It alters the light's reality and thus can be used to enhance every parameter of light. This statement is even more justified if we consider space-time transformations. These transformations regard both electromagnetic and physical space as four-dimensional geometries between which we can perform general transformations. This will be presented and discussed in the last chapter of this thesis, where we will apply this theory to design frequency shifters. Before we will do that, we will apply the theory to design optical cavities. This will be the subject of the chapters to come.

References

[1] U. Leonhardt and P. T. G., "Transformation optics and the geometry of light," *Prog. Opt.* , to appear, 2009.

[2] J. B. Pendry, D. Schurig, and D. R. Smith, "Controlling electromagnetic fields," *Science* **312**, 1780–1782, 2006.

[3] J. Plebanski, "Electromagnetic waves in gravitational fields," *Phys. Rev.* **118**, 1396–1408, 1960.

[4] U. Leonhardt, "Optical conformal mapping," *Science* **312**, 1777–1780, 2006.

[5] M. Rahm, D. Schurig, D. A. Roberts, S. A. Cummer, D. R. Smith, and J. B. Pendry, "Design of electromagnetic cloaks and concentrators using form-invariant coordinate transformations of maxwell's equations," *Photon. Nanostruct.: Fundam. Applic.* **6**, 87–95, 2008.

[6] M. Rahm, D. A. Roberts, J. B. Pendry, and D. R. Smith, "Transformation-optical design of adaptive beam bends and beam expanders," *Opt. Express* **16**, 11555–11567, 2008.

[7] M. Rahm, S. A. Cummer, D. Schurig, J. B. Pendry, and D. R. Smith, "Optical design of reflectionless complex media by finite embedded coordinate transformations," *Phys. Rev. Lett.* **100**, 63903, 2008.

[8] M. Y. Wang, J. J. Zhang, H. S. Chen, Y. Luo, S. Xi, L. X. Ran, and J. A. Kong, "Design and application of a beam shifter by transformation media," *PIER* **83**, 147–155, 2008.

[9] D. Kwon and D. H. Werner, "Polarization splitter and polarization rotator designs based on transformation optics," *Opt. Express* **16**, 18731–18738, 2008.

[10] A. Greenleaf, Y. Kurylev, M. Lassas, and G. Uhlmann, "Cloaking devices, electromagnetic wormholes, and transformation optics," *SIAM Review* **51**, 3–33, 2009.

[11] Z. Jacob, L. V. Alekseyev, and E. Narimanov, "Optical hyperlens: Far-field imaging beyond the diffraction limit," *Opt. Express* **14**, 8247–8256, 2008.

[12] N. Kundtz, D. A. Roberts, J. Allen, S. Cummer, and D. R. Smith, "Optical source transformations," *Opt. Express* **16**, 21215–21222, 2008.

[13] U. Leonhardt and T. G. Philbin, "General relativity in electrical engineering," *New J. Phys.* **8**, 1777–1780, 2006.

[14] A. Einstein, "Die grundlage der allgemeinen relativitatstheorie," *Ann. der. Phys.* **49**, 769–822, 1916.

[15] S. Carroll, *Spacetime and Geometry*, Addison Wesley, New York, 2003.

[16] Y. Wei, Y. Min, R. Zhichao, and Q. Min, "Coordinate transformation makes perfect invisibility cloak with arbitrary shape," *New J. Phys.* **10**, 6134–6145, 2008.

[17] Y. Yu, W. K. George, and Z. Peng-Wang, "Invisibility cloaks for irregular particles using coordinate transformations," *Opt. Express* **16**, 6134–6145.

[18] P. W. Milonni, *Fast light, slow light and left-handed light*, Taylor and Francis, New York, 2005.

[19] U. Leonhardt and T. Tyc, "Broadband invisibility by non-Euclidean cloaking," *Science* **323**, 110–112, 2009.

[20] V. G. Veselago, "The electrodynamics of substances with simultaneously negative values of ϵ and μ," *Sov. Phys. Usp.* **10**, 509–514, 1968.

[21] D. Shurig, J. B. Pendry, and D. R. Smith, "Transformation-designed optical elements," *Opt. Express* **15**, 14772–14782, 2007.

[22] M. Yan, W. Yan, and M. Qiu, "Cylindrical superlens by a coordinate transformation," *Phys. Rev. B* **78**, 125113, 2008.

[23] M. Tsang and D. Psaltis, "Magnifying perfect lens and superlens design by coordinate transformation," *Phys. Rev. B.* **77**, 35122, 2007.

CHAPTER 4

Dielectric Microcavities

This chapter contains a general introduction to dielctric microcavities. Herewith, we will set the scene of the chapters to come. First, we introduce some basic concepts related to open resonators: whispering gallery modes, characterised by a complex frequency and a set of mode numbers, quality factors and mode volumes. Furthermore, this chapter provides a good example to demonstrate and verify our mathematical formalism which is also used in the following chapters.

4.1 Microcavities in Photonics

Many advances in science and technology emanate from the human urge to control our surrounding environment. One of the most distinct ways of contolling something is to capture and confine it within a finite region of space. The same is true for light waves. An optical microcavity is a component that serves this purpose. The quality of such a microcavity is determined by two important parameters: the quality factor — what's in a name? — Q, which essentially describes the temporal confinement, and the modevolume V, which is a measure of the spatial extent of the electromagnetic field. Several applications involving optical microcavities, such as optical data-storage [1], add-drop filters [2], cavity QED [3] and enhanced light sources [2]) require the electromagnetic energy in a small volume (small V) over a long periode (high Q). This broad range of applications is implemented with different types of microcavities, the most imporant implementations being Fabry-Pérot cavities, photonic crystal cavities and dielectric microcavities [4].

Fig. 4.1 shows the top-view of such a dielectric microcavity, a cylindrical rod with index of refraction n_{in}, surrounded by another dielectric, e.g., air with a lower index of refraction n_{out}. Light rays can circle around resonantly in such a cylinder due to total internal reflection, as indicated Fig. 4.1. This occurs when the optical path length equals an integral number of wavelengths. The same reasoning applies to the spherical cases, where the light ray path can be
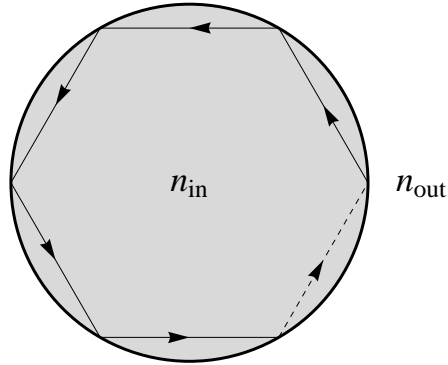
Figure 4.1: Top-view of a cylindrical microresonator. Resonances occur when the optical path length equals an integer number of the wavelength inside the cavity.

inclined with respect to the equatorial plane. This geometrical interpretation is, however, a very simple approximation of reality. Along a curved interface, total internal reflection is not as total as we are used to. When the size of the resonator approaches the magnitude of the wavelength, effects of diffraction, neglected in the previous picture, should be taken into account. In the next section we will calculate these modes more rigourously.

4.2 Quasi-Normal Modes

4.2.1 Method

The modes of a system are determined by a general equation for the propagation through space-time, and the boundary conditions, imposing additional restraints. Therefore, we will look for solutions of the electromagnetic field that comply with Maxwell's equations in combination with proper boundary conditions.

During these calculations, we will rely on the assumption that the material inhibits no absorption. Including this effects would not alter the results significantly, but rather obscure them. Traditional microcavity materials such as silica meet these assumption quite good. A more subtle assumption is made concerning the time-dependency of these modes. We will assume that a general solution inside the cavity can be written as a sum of fields with time-harmonic dependence.

$$\mathbf{E}(\mathbf{r}, t) = \mathbf{E}(\mathbf{r})e^{-i\omega t}. \tag{4.1}$$

Section 4.3.3 guarantees that this is possible.

Bearing these assumptions in mind, we now consider a dielectric cylinder with index of refraction n_{in} surrounded by a dielectricum with lower index of refraction n_{out}. We will look for solutions where the electric field is independent of the z-coordinate, directed along the z-axis
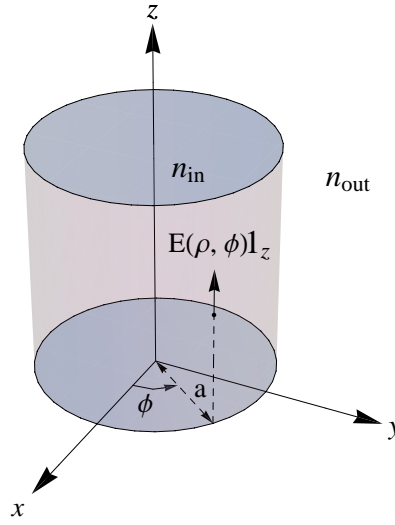
Figure 4.2: Schematic illustration of the system under consideration: a dielectric cylinder with radius a, refractive index n_{in}, embedded in a dielectricum with index of refraction n_{out}. Calulations are made for the TE-polarisation.

(TE polarisation), as depicted in Fig. 4.2:

$$\mathbf{E}(\mathbf{r}) = E(\rho, \phi) \, \mathbf{1_z}. \tag{4.2}$$

In isotropic and homogeneous regions of space, Maxwell's equations can be combined to Helmoltz' equation:[5]

$$\Delta \mathbf{E} + k^2 \, \mathbf{E} = 0, \tag{4.3}$$

where k^2 equals ω^2/c^2. This differential equation can be expanded in cylindrical coordinates:

$$\frac{1}{\rho} \frac{\partial}{\partial \rho} \left(\rho \frac{\partial E(\rho, \phi)}{\partial \rho} \right) + \frac{1}{\rho^2} \frac{\partial^2 E(\rho, \phi)}{\partial \phi^2} + \frac{\partial^2 E(\rho, \phi)}{\partial z^2} + k^2 \, E(\rho, \phi) = 0, \tag{4.4}$$

the projections along the $x-$ and $y-$axes are trivial. Using the technique of seperation of variables $E(\rho, \phi) = R(\rho) \, \Phi(\phi)$, we can rewrite this equation as:

$$\frac{\partial^2 \Phi(\phi)}{\partial \phi^2} + \nu^2 \Phi(\phi) = 0, \tag{4.5}$$

$$\rho^2 \frac{\partial^2 R(\rho)}{\partial \rho^2} + \rho \frac{\partial R(\rho)}{\partial \rho} + (\rho^2 k^2 - \nu^2) R(\rho) = 0, \tag{4.6}$$

with ν^2 an arbitrary real number.

According to Eq. (4.5), the angular dependence, $\Phi(\phi)$, are imaginary exponentials, the radial part of the electric field, which satisfies the (cylindrical) Bessel equation, Eq. (4.6), in the variable $(k\rho)$, has solutions in terms of (cylindrical) Bessel or Hankel functions. For simplicity of the

equations to come, we will use the Bessel functions J_ν and Y_ν inside, and the Hankelfunctions $H_\nu^{(1)}$ and $H_\nu^{(2)}$ outside the cylinder. The spatial dependency of the electric field in Fig. 4.2 can then be summarised as:

$$E_{\text{in}}(\rho, \phi) = [A \, J_\nu(k_{\text{in}}\rho) + B \, Y_\nu(k_{\text{in}}\rho)]e^{\pm i\nu\phi}, \tag{4.7}$$

$$E_{\text{out}}(\rho, \phi) = [C \, H_\nu^{(1)}(k_{\text{out}}\rho) + D \, H_\nu^{(2)}(k_{\text{out}}\rho)]e^{\pm i\nu\phi}. \tag{4.8}$$

where $k_{\text{in}} = n_{\text{in}} k_0$, $k_{\text{out}} = n_{\text{out}} k_0$ and (A, B, C, D) are complex integration constants. In the next step, we will now apply the boundary conditions to these fields:

Angular continuity At all radii the electric field must be continuous in ϕ, mathematically speaking: $E(\rho, 0) = E(\rho, 2\pi)$. The angular part of E should thus be periodic with period 2π. This happens when $\nu = m$, with $m \in \mathbb{Z}$. We will see shortly that this naturally implies that the magnetic field is continuous in this direction.

Finite energy In all practical situations, we will only excite those modes whose energy is finite. Inside the cylinder this implies we should reject the Bessel function Y_m, being which is infinite in the origin.

Sommerfeld radiation condition This condition is the mathematical translation of the physical fact that no energy is "flowing in" from infinity, which is fulfilled by dropping the second Hankel function $H_m^{(2)}$, since it represents an incoming wave.

Taking the above constraints into account, we can simplify the expressions (4.7)-(4.8) to

$$E_{\text{in}}(\rho, \phi) = A \, J_m(n_{\text{in}}k_0\rho)e^{\pm im\phi}, \tag{4.9}$$

$$E_{\text{out}}(\rho, \phi) = C \, H_m^{(1)}(n_{\text{out}}k_0\rho)e^{\pm im\phi}. \tag{4.10}$$

Electromagnetic boundary conditions At the interface between two materials, the electromagnetic fields satisfy [6]:

$$\Delta D_{\text{n}} = \sigma, \tag{4.11}$$

$$\Delta B_{\text{n}} = 0, \tag{4.12}$$

$$\Delta E_{\text{t}} = 0, \tag{4.13}$$

$$\Delta H_{\text{t}} = J_{\parallel}, \tag{4.14}$$

where both the free charge density, σ, and the surface current density, $J_{\parallel}$, equal to zero. Expressing Faraday's law in cylindrical coordinates yields

$$B_{\text{n}} = \frac{1}{i\omega\rho}\frac{\partial E}{\partial \phi}, \tag{4.15}$$

$$H_{\text{t}} = \frac{i}{\omega\mu}\frac{\partial E}{\partial \rho}. \tag{4.16}$$

Since we assumed the electric field to be purely tangential to the interface, the first condition, Eq. (4.11), is automatically fulfilled. Eqs. (4.12)-(4.13) both require the radial part of the electric field to be continuous. The last boundary condition, Eq. (4.14), imposes an additional constraint on the radial derivative of the electric field. In summary, the boundary

conditions, Eqs. (4.11)-(4.14), impose a set of two equations connecting the fields inside and outside the cylinder:

$$A\,J_m(n_\text{in}k_0a) = C\,H_m^{(1)}(n_\text{out}k_0a), \tag{4.17}$$

$$A\,\frac{n_\text{in}k_0}{\mu_\text{in}}J_m'(n_\text{in}k_0a) = C\,\frac{n_\text{out}k_0}{\mu_\text{out}}H_m^{(1)'}(n_\text{out}k_0a), \tag{4.18}$$

where the accents refer to differentiation with respect to the radial coordinate ρ. The nontrivial solutions of this set can be found by equating it's determinant to zero, resulting in the dispersion relation of the cavity:

$$\sqrt{\frac{\mu_\text{out}}{\epsilon_\text{out}}}J_m(n_\text{in}k_0a)H_m^{(1)'}(n_\text{out}k_0a) - \sqrt{\frac{\mu_\text{in}}{\epsilon_\text{in}}}J_m'(n_\text{in}k_0a)H_m^{(1)}(n_\text{out}k_0a) = 0. \tag{4.19}$$

In reasoning above, we gradually derived the dispersion relation to calculate the eigenmodes of a dielectric cylinder, paying attention to the importance of the boundary conditions in the determination of the systems solutions. In the next section we will explicitly solve Eq.(4.19), to find out which frequencies (ω) constitute the eigenfrequencies of this setup.

4.2.2 Results

Even when we assume absorptionless materials ($n_\text{in}, n_\text{out} \in \mathbb{R}$), Eq. (4.19) has no real solutions for k_0. This is a characteristic property of open systems, which we will discuss in section(4.3.2). To visualise the dispersion relation in the complex plane, we make contour plots of its real and imaginary parts. This will produce plots as shown in Fig. 4.3. The eigenfrequencies are consequently located at an intersection between a red and a blue curve, implying both real and imaginary parts of Eq. (4.19) to be zero.

Once we have found these solutions, the coefficients A and C can be calculated as the eigenvectors corresponding to the eigenvalue zero of Eqs. (4.17)-(4.18). These are only determined up to a normalisation factor, which depends on the energy pumped into the system. Fig. 5.4 shows a two-dimensional and a cross-sectional plot of the electric field corresponding to the second intersection ($k_0\,a = 3.44 - 1.39 \cdot 10^{-2}\,i$) of Fig. 4.3.

Very good confinement occurs for high m-numbers. When we choose, for instance, $m = 16$, we obtain the contour plots of Fig. 4.5. The imaginary part of these solutions is several orders of magnitude smaller than in the former example (comparing first intersections: $(k_0\,a)_{m=5} = 2.36 - 1.28 \cdot 10^{-3}\,i$, $(k_0\,a)_{m=16} = 6.30 - 1.47 \cdot 10^{-10}\,i$). The corresponding mode profile is shown in Fig. 4.6. These solutions are often referred to as whispering-gallery modes, due to the striking resemblence with acoustic whispering-gallery modes, which were first studied by Lord Rayleigh to explain the peculiar propagation of sound waves in Saint Paul's Cathedral, London, through which you can here somebody whispering, if you are both positioned close to the walls of the hall, but not in the center [7].

The correctness of these previous results has been verified by means of finite elements simulations with Comsol Multiphysics.
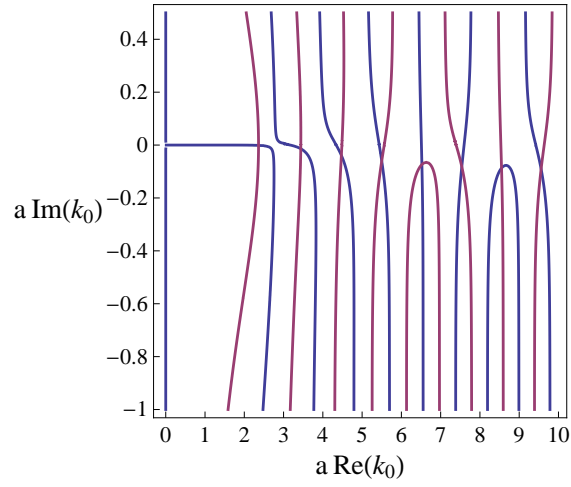
Figure 4.3: Contour plots in the complex k_0-plane, showing real (blue) and imaginary part (red) of Eq. (4.19). Parameters are $\epsilon_{\text{in}} = 10, \epsilon_{\text{out}} = \mu_{\text{in}} = \mu_{\text{out}} = 1, m = 5$. Intersections of a red and a blue curve indicate solutions to the dispersion relation.

(a)   (b)
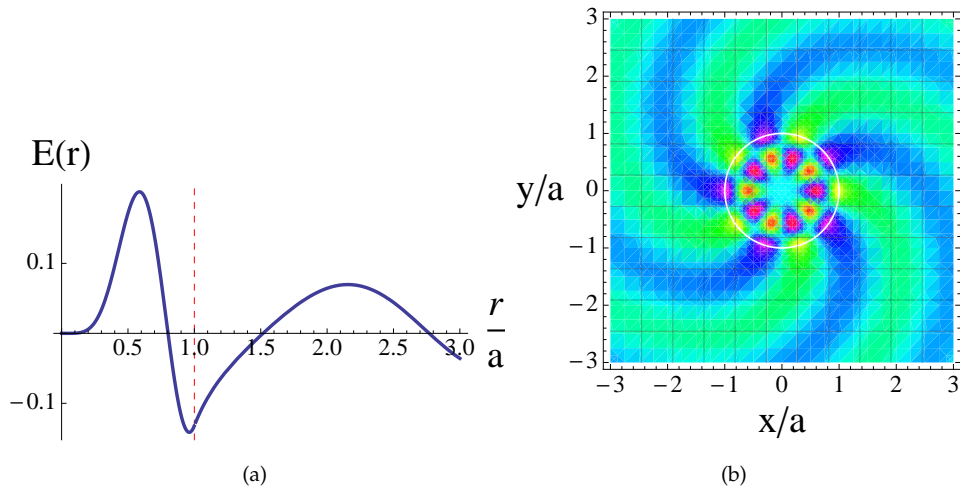
Figure 4.4: Electric field corresponding to the second intersection of Fig. 4.3: $Re(k_0) a = 3.44$, $Im(k_0) a = -1.39 * 10^{-2}$. (a) Cross-sectional plot showing the radial field distribution. The dashed line indicates the boundary of the cavity. (b) Two-dimensional plot demonstrating the typical angular pattern.
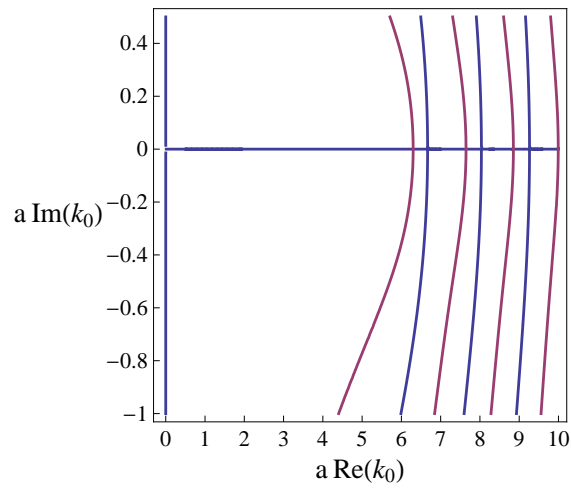
Figure 4.5: Contour plot for the system described in Fig.4.3, but the modes are now calculated for the parameter $m = 16$.

(a)

(b)
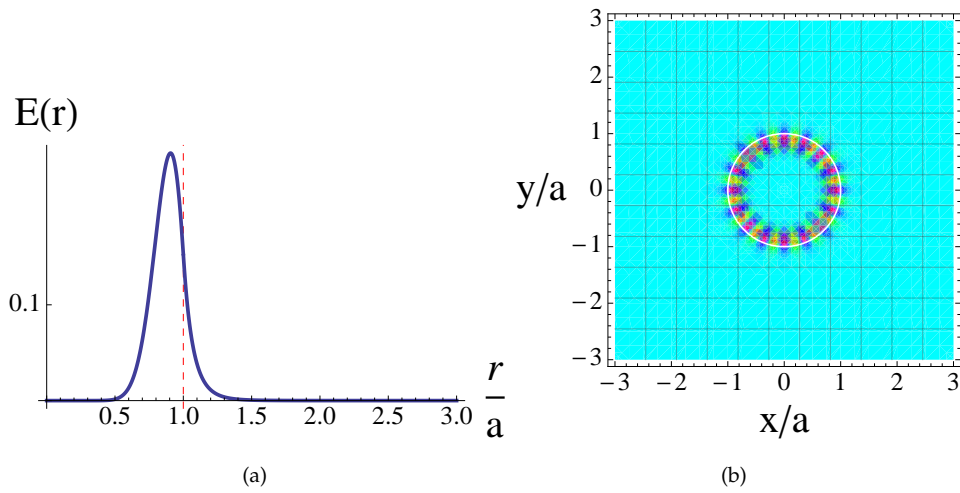
Figure 4.6: Electric field corresponding to the first intersection of Fig. 4.5: $Re(k_0) a = 6.30$, $Im(k_0) a = -1.47 \cdot 10^{-10}$. (b) Cross-sectional plot showing the radial field distribution. The field is almost entirely located at the boundary of the cavity. (a) Two-dimensional plot demonstrating the typical angular pattern.

4.3 Discussion

4.3.1 Quantisation

As we can observe from the results in the previous section, the eigenmodes of a cylindrical microcavity are quantised. The solutions can thus be characterised with discrete "mode numbers". A first quantisation occurred when imposing the angular continuity of the electromagnetic field. This condition gave birth to $m \in \mathbb{Z}$. Ph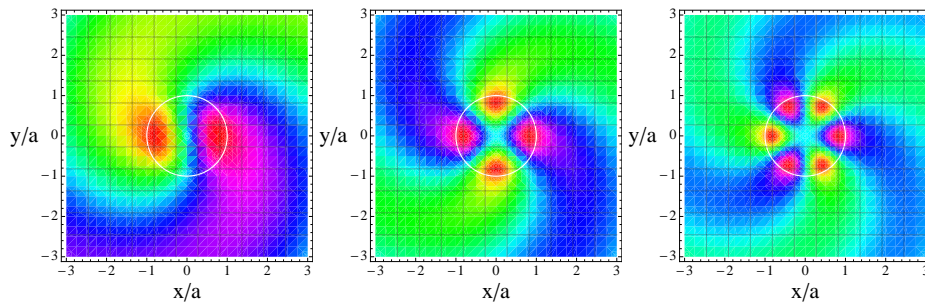ysically, this number corresponds to the number of field maxima in one round trip, which is illustrated by Fig.4.7 for three different values of m. From the "photon-point-of-view", this quantity actually measures the tangential component of its angular momentum.

Figure 4.7: Two-dimensional plots indicating the effect of the angular mode number m on the field distribution for $m = 1, 2, 3$. This number equals the number of wavelengths in one round trip inside the cavity.

Another quantisation arose when solving the dispersion relation, Eq. (4.19). The intersections on Fig. 4.3 indicated several solutions of the dispersion relation with a fixed mode number m. The origin of this quantisation is the same as with the quantum mechanical solutions for an electron inside a finite potential well. Therefore, the different solutions are ordered using the radial mode number ν, measuring the radial component of the photon momentum [8]. Fig. 4.8 clearly demonstrates the effect of ν, raising the radial field variation inside the cavity.
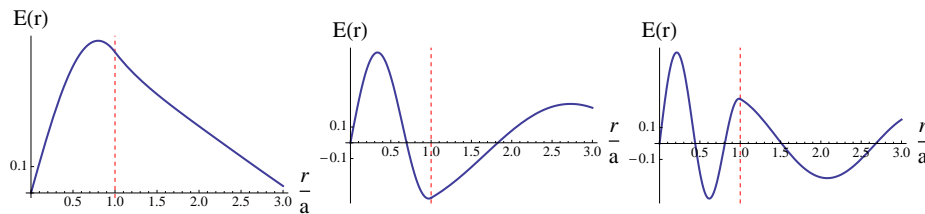
Figure 4.8: Cross-sectional plots indicating the effect of the radial mode number ν on the radial field distribution for $\nu = 1, 2, 3$. This number equals the number of field maxima inside the cavity.

We could draw this analogy with quantum mechanics even further by defining a third mode number μ, encoding the chosen polarisation (TE or TM), as a replacement for the spin quantum number s [8].

The combination of both quantum numbers ν and m offers insight in the photon trajectory. To that aim, we write down the electric field outside the cavity:

$$E_{\text{out}}(\mathbf{r}, t) = C \, H_m^{(1)}(n_{\text{out}} k_0 r) e^{im\phi} e^{-i\omega t}. \tag{4.20}$$

For large arguments $|z| \rightarrow \infty$, the Hankel function of the first kind can be approximated by [9]

$$H_m^{(1)}(z) = \sqrt{\frac{2}{\pi z}} e^{i(z - \frac{m\pi}{2} - \frac{\pi}{4})}. \tag{4.21}$$

For the same large values, Eq.(4.20), can be approximated by:

$$E_{out}(\mathbf{r}, t) \sim e^{i(n_{out} k_0 r + m\phi - \omega t)}. \tag{4.22}$$

Bearing in mind the effect of ν on the real part of k_0, we derived that the surfaces of constant phase are moving along helical trajectories, whose centrifugal properties are determined by ν and m.

An important remark concerning the quantisations is how they impose a lower boundary on the mode volume V. It is convenient to introduce a dimensionless parameter $X = k_{in}a = 2\pi a/\lambda_{in}$. This parameter compares the dimensions of the cavity to the wavelength of the light inside the cavity. Fig. 4.9 shows the solutions with mode number $m = 1$, which have the lowest value of X, since the real part of the solutions is proportional to the mode number. It first solution, located around $Re(X) = 2$, indicates the general principle of traditional optics that is is impossible to confine light in a volume with characteristic dimensions smaller than its wavelength.

This is perhaps a good time to introduce a more rigorous definition of the mode volume $V_{vm\mu}$. It is usually defined, related to the energy density inside a cavity, as a normalised integration of the total energy density of the mode. This gives us a measure of how well the fields are confined within the cavity, taking into account the evanescent tails:

$$V_{Mode} = \frac{\int_{Mode} \epsilon(\mathbf{r})|\mathbf{E}(\mathbf{r})|^2 \, d\mathbf{r}}{\max(\epsilon(\mathbf{r})|\mathbf{E}(\mathbf{r})|^2)}. \tag{4.23}$$

Having a finite quality factor Q and thus radiating energy to infinity, whispering gallery modes will produce difficulties, as this integral will not converge ($E \sim e^{i(k' + ik'')r} \sim e^{-k''r}$, with $k'' < 0$) [10]. Actually, we are only interested in the energy density of the part of the mode which is trapped inside the cavity. It is pointless to take the radiating parts into account. When Q is high, the confined part of the mode will dominate near the surface and the radiating tail will come in the picture after some distance R. Therefore, the mode profile will exponentially decay near the resonators surface (as shown in Fig.4.6) and will begin to rise again after some distance R. To illustrate this, Fig.4.10 plots the same mode on two different scales, indicating the two different regions. Although it is not quite rigorous, the integration problem could be solved by integrating Eq.(4.23) up to a value R' where the field has become negligible.
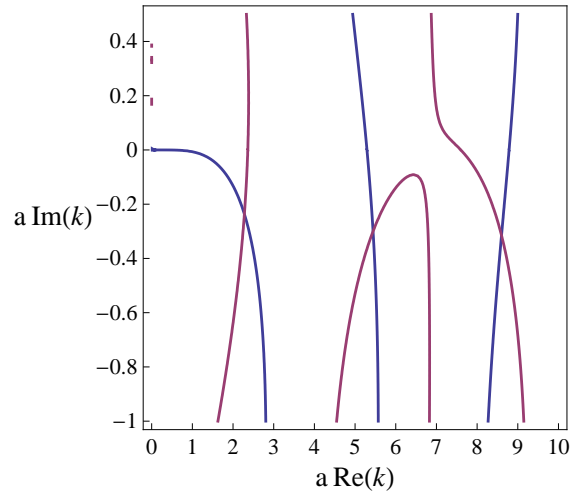
Figure 4.9: Contour plot of a system with $\epsilon_{in} = 10$, $\epsilon_{out} = \mu_{in} = \mu_{out} = 1$, expressed in terms of the parameter $X = k_{in}a$, showing the lower boundary of the wavelength we can confine within a cavity of radius a.

(a)

(b)
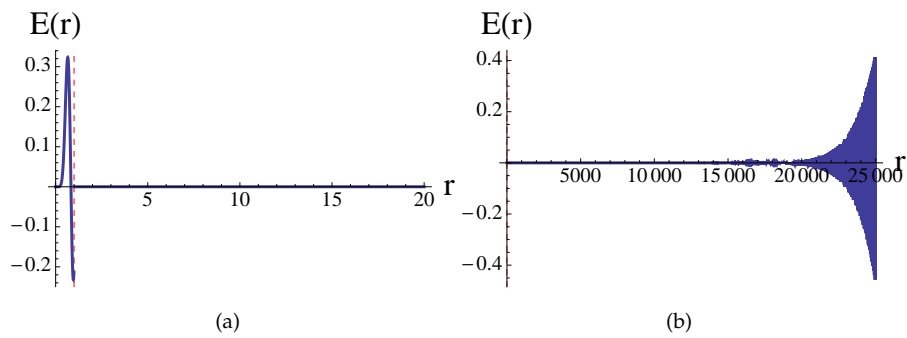
Figure 4.10: Cross-sectional plots of a mode with $m = 8$ and $\nu = 2$ with the usual material parameters. (a) Plot of the near field, close to the resonators surface, (b) The far-field regime showing the radiating part of the mode.

4.3.2 Complex Frequencies

Complex eigenfrequencies are key characteristic of quasi-normal modes. These eigenfrequencies arise due to the boundary condition at infinity: in the case of a conservative system we state a vanishing field condition (at infinity or the systems boundary). In this case, however, we chose "the purely outgoing wave"-condition, loosing the time-reversability of the system and thus generating complex eigenfrequencies [8]. Since we are used to handle real eigenfrequencies and their associated normal modes, it will be advantageous to spend some attention to their complex counterparts. Let us start with reinserting this complex eigenfrequency ($\omega = \omega' + i\omega''$) in Eq.(4.1) to write down the time-dependency of the electric field:

$$\mathbf{E}(\mathbf{r}, t) = \mathbf{E}(\mathbf{r})e^{-i\omega' t}e^{\omega'' t}. \tag{4.24}$$

The electric field of a mode with negative ω'' will exponentially decay in time with a decay rate proportional to the imaginary part of the eigenfrequency. This is the mathematical translation of the fact that microcavities are essentially open systems, losing energy continuously to the outside world. The previous result suggests that we could relate the quality factor to the eigenfrequency. Indeed, the quality factor is usually defined as the temporal confinement of the energy normalised to the frequency of oscillation, such that Q^{-1} represents the fraction of energy lost in a single optical cycle. Being defined in relation to the systems energy, which decays as $e^{2\omega'' t}$, we define the quality factor as

$$Q = \frac{\omega'}{2\omega''}. \tag{4.25}$$

Another approach to define this quality factor passes by the Fourier plane. The spectrum of these complex eigenmodes is given by the Fourier transform of Eq. (4.24):

$$\mathbf{E}(\mathbf{r}, \omega) = \frac{1}{\sqrt{2\pi}} \int_{-\infty}^{\infty} \mathbf{E}(\mathbf{r}, t)e^{i\omega t}\, dt = \frac{\mathbf{E}(\mathbf{r})}{\sqrt{2\pi}\,[\,i(\omega - \omega') + \omega'']}. \tag{4.26}$$

The associated power spectrum therefore follows the well-known Lorentzian line function, as shown in Fig. 4.11. From this point of view, the quality factor is defined as the ratio of the resonant frequency to its linewidth (full width half maximum), which results in the same formula as Eq. (4.25).

Let us now have a look on how this quality factor depends on the chosen parameters:

Material properties The ratio of the refractive indices $n_{\text{in}}/n_{\text{out}}$ highly affects the Q-factor. This seams quite reasonable since this ratio determines the amount of reflection at the interface between both dielectrics.

Mode indices When ν is chosen to be a constant, Q also improves with increasing angular momentum m. Having a higher momentum in the angular than in the radial direction, will cause the photon to collide at glazing incidence with the boundary, enhancing the amount of reflection.

The previous two effects are well summarised in Fig. 4.12, where the Finesse ($F = Q/m$) is shown as a function of the mode number m (and the lowest order radial solution $\nu = 1$) for several values of the dielectric constant ϵ inside the cavity. This graph, reproduced from [11], matches very well with the results obtained by our program, as indicated by the asterixes.
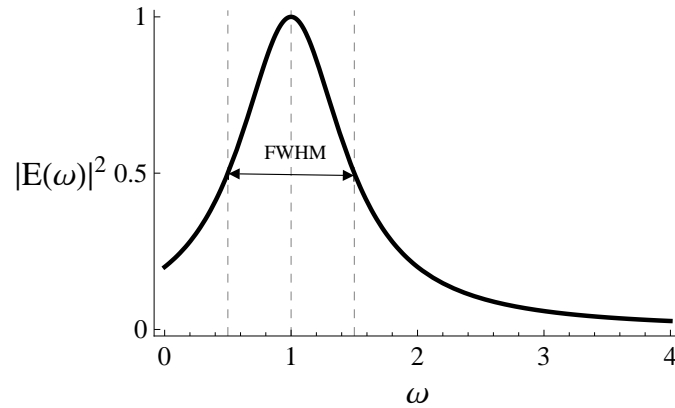
Figure 4.11: Power spectrum associated with a complex eigenfrequency $\omega = 1.0 + 0.5\,\mathrm{i}$, having FWHM $= 2 \cdot 0.5$.
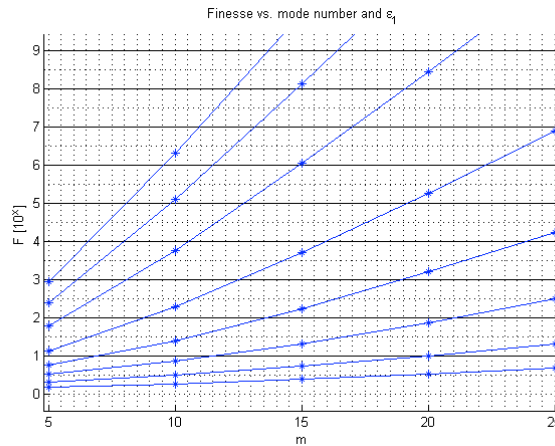
Figure 4.12: The Finesse F calculated for several whispering gallery modes with TE-polarisation. Each line shows the variation of F versus the angular momentum m, with $\nu = 1$. These lines are plotted for several values of $\frac{n_{in}}{n_{out}}$, ranging from 1.25 up to 3.5. Blue lines, reproduced from [11], asterixes generated with simulation.

4.3.3 A Complete Set of Eigenmodes

Complex frequencies raise ontological questions on the concept of a mode. Usually, working in self-adjoint systems, the eigenmodes form a complete set, implying the possibility to expand any abritrary (piecewise continuous) function $f(x)$ as an infinite sum of the eigenfunctions $\phi(x)$:

$$\lim_{m \to \infty} \int_a^b \left[f(x) - \sum_{n=0}^m a_n \phi_n(x) \right]^2 \, \mathrm{d}x = 0. \tag{4.27}$$

The integration domain corresponds to the physical boundary at which the field vanishes. In the case of quasi-normal modes, with an exponentially growing field at infinity, the above integral is definitely not applicable. Moreover, to proof the completeness of the eigenmodes of Hermitian operators, one explicitly uses this property [12]. It is therefore not a trivial question whether quasi-normal modes form a complete set. The importance of this property should not be underestimated. Most importantly, to study the dynamics of a system, the problem can be reduced to the study of its eigenfunctions, at least when they form a complete set. Also, a complete set of eigenfunctions is accompanied by a rich mathematical formalism to make analytic calculations, such as higher order perturbation theory. Recently, it has been proven that, under certain circomstances, the quasi-normal modes of a dielectric microcavity form a complete set inside this cavity. In honour of the mathematical beauty, we will give here the outline of the proof given in Ref. [13] , which we have applied to the cylindrical case.

Let us start by considering the retarded Green's function that satisfies

$$\left[\rho \frac{\partial}{\partial \rho}(\rho \frac{\partial}{\partial \rho}) - \rho^2 \epsilon(\rho) \frac{\partial^2}{\partial t^2} - m^2 \right] G(\rho, \rho'; t) = \delta(t)\delta(\rho - \rho'). \tag{4.28}$$

and $G(\rho, \rho'; t) = 0, \forall t \leqslant 0$. In the Fourier domain, this can be rewritten as

$$\tilde{D}(\omega)\tilde{G}(\rho, \rho'; \omega) = \left[\rho \frac{\partial}{\partial \rho}(\rho \frac{\partial}{\partial \rho}) + \rho^2 \epsilon(\rho)\omega^2 - m^2 \right] \tilde{G}(\rho, \rho'; \omega) = \delta(\rho - \rho'). \tag{4.29}$$

This means that $\tilde{G}(\rho, \rho', \omega)$ is a solution of Eq. (4.6), except in $\rho = \rho'$. Suppose now that $f(\rho, \omega)$ and $g(\rho, \omega)$ are solutions of 4.6, with $f(0, \omega) < \infty$ and $g(r, \omega)$ satisfies Sommerfeld's boundary condition. We then know that $\tilde{G}(\rho, \rho', \omega)$ can be written as [14]:

$$\tilde{G}(\rho, \rho'; \omega) = \frac{f(\rho, \omega)g(\rho', \omega)}{\tilde{W}(\omega)}. \tag{4.30}$$

where $\tilde{W}(\omega) = \rho(g \frac{\partial f}{\partial \rho} - f \frac{\partial g}{\partial \rho})$ is the reduced Wronskian, which is independent of ρ thanks to Abel's theorem. The trick is now to express $G(\rho, \rho'; t)$ in terms of f and g, using the inverse Fourier transform: $G(\rho, \rho'; t) = \frac{1}{2\pi} \int_{-\infty}^{\infty} \tilde{G}(\rho, \rho'; \omega) e^{-i\omega t} \, d\omega$. This integral can now be evaluated using complex analysis, by closing the the contour line with a hemicircle in the lower half-plane as shown in Fig.(4.13):

$$G(\rho, \rho'; t) = i \sum_{j=1}^{n} \text{Res}(\tilde{G}(\rho, \rho'; \omega), \omega_j) - I_c \tag{4.31}$$

To continue we will have to introduce two assumptions on the variation of the dielectric constant:

(i) $\epsilon(\rho)$ inhibits at least one discontinuity,

(ii) $\epsilon(\rho)$ is bounded and approaches its asymptotic value faster than any exponential.

The contribution of the integral along the closing circle I_c at infinity vanishes with the help of the discontinuity (i). This leaves us with the calculation of the residues. The second assumption (ii) ensures f and g to be analytic in the lower half-plane. The poles of $\tilde{G}(\rho, \rho'; \omega)$ thus coincide
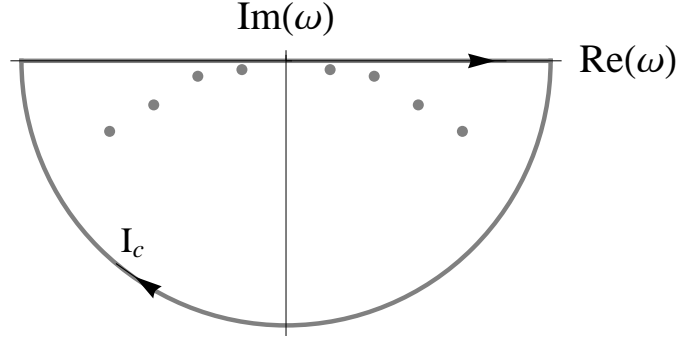
Figure 4.13: Contourintegral to calculate $G(\rho, \rho', t)$.

with the zeros of the Wronskian. At these complex frequencies $f(\rho, \omega)$ must be proportional to $g(\rho, \omega)^*$ and so both boundary conditions are met at the same time, implying that f and g are quasi-normal modes.

The residue of a function $f(z) = \frac{g(z)}{h(z)}$ at a simple pole z_1, with g, h analytic in z_1 and $g(z_1) \neq 0$, $h(z_1) = 0$ is given by $Res(f(z), z_1) = \frac{g(z_1)}{h'(z_1)}$. Applied to our problem, this formula translates to:

$$Res(\tilde{G}(\rho, \rho'; \omega), \omega_j) = \frac{f(\rho, \omega_j) g(\rho', \omega_j)}{\frac{\partial \tilde{W}(\omega)}{\partial \omega}|_{\omega = \omega_j}} \tag{4.32}$$

We would now wish to rewrite this denominator using f and g. Since they are both solutions of 4.6, we can write:

$$\rho^2 \epsilon(\rho) \omega^2 g(\rho, \omega) = -\rho \frac{\partial}{\partial \rho}(\rho \frac{\partial}{\partial \rho}) g(\rho, \omega) + m^2 g(\rho, \omega) \tag{4.33}$$

$$\rho^2 \epsilon(\rho) \omega_j^2 f(\rho, \omega_j) = -\rho \frac{\partial}{\partial \rho}(\rho \frac{\partial}{\partial \rho}) f(\rho, \omega_j) + m^2 f(\rho, \omega_j) \tag{4.34}$$

Multiplying both equations with the absent function and substracting leads to:

$$\rho(\omega^2 - \omega_j^2)\epsilon(\rho) g(\rho, \omega) f(\rho, \omega_j) = \left[\frac{\partial}{\partial \rho}(\rho \frac{\partial g(\rho, \omega)}{\partial \rho})\right] f(\rho, \omega_j) - \left[\frac{\partial}{\partial \rho}(\rho \frac{\partial f(\rho, \omega_j)}{\partial \rho})\right] g(\rho, \omega) \tag{4.35}$$

and after integration up to a large distance R:

$$(\omega^2 - \omega_j^2) \int_0^R \rho \epsilon(\rho) g(\rho, \omega) f(\rho, \omega_j) \, d\rho = \left[\rho \frac{\partial g(\rho, \omega)}{\partial \rho} f(\rho, \omega_j) - \rho \frac{\partial f(\rho, \omega_j)}{\partial \rho} g(\rho, \omega)\right]_0^R \tag{4.36}$$

Since R is large and we know that both f and g satisfy the outgoing boundary condition, we can rewrite the right-hand side of previous equation to:

$$\left[i(\omega_j - \omega) \sqrt{\epsilon(\rho)} \rho g(\rho, \omega) f(\rho, \omega_j)\right]_{\rho = R} - \left[\rho \frac{\partial g(\rho, \omega)}{\partial \rho} f(\rho, \omega_j) - \rho \frac{\partial f(\rho, \omega_j)}{\partial \rho} g(\rho, \omega)\right]_{\rho = 0} \tag{4.37}$$

$^*gf' = fg' \leftrightarrow f \sim g$

This second terms is almost $\tilde{W}(\omega)$. Since we are looking for $\frac{\partial \tilde{W}(\omega)}{\partial \omega}|_{\omega=\omega_j}$, we reinsert 4.37 in 4.36 continue by differentiating this with respect to ω and set $\omega = \omega_j$.

$$2\omega_j^2 \int_0^R \rho\epsilon(\rho)g(\rho,\omega)f(\rho,\omega_j)\,\mathrm{d}\rho + \mathrm{i}\sqrt{\epsilon(R)}\,R\,g(R,\omega)f(R,\omega_j) = \frac{\partial \tilde{W}(\omega)}{\partial \omega}|_{\omega=\omega_j} \qquad (4.38)$$

We are almost there. Let's introduce the norm $\ll f(\rho,\omega_j)f(\rho,\omega_j) \gg$

$$\ll f(\rho,\omega_j)f(\rho,\omega_j) \gg = \lim_{R\to\infty}\left[\int_0^R \rho\epsilon(\rho)f(\rho,\omega_j)f(\rho,\omega_j)\,\mathrm{d}\rho + \frac{\mathrm{i}}{2\omega_j}\sqrt{\epsilon(R)}\,R\,f(R,\omega_j)f(R,\omega_j)\right] \tag{4.39}$$

This enables us to rewrite 4.31 as:

$$G(\rho,\rho';t) = \frac{\mathrm{i}}{2}\sum_{j=1}^{n}\frac{f(\rho,\omega_j)f(\rho',\omega_j)\mathrm{e}^{-\mathrm{i}\omega_j t}}{\omega_j \ll f(\rho,\omega_j)f(\rho,\omega_j) \gg} \qquad (4.40)$$

This last statement proves the completeness of the quasi-normal set, since every solution of the wave equation can be written as a sum of Greens functions, which in turn can be written as a sum of the quasi-normal modes.

4.4 Practical Implementation and Applications

Depending on the application in view, dielectric microresonators will be implemented as different geometries (Fig.4.14), using specific materials (liquid microdroplets, fused silica, optical crystals). The spherical structures are fabricated by melting a little piece of optical fibre, where the surface tension forces generate an atomically smooth surface. The two dimensional structures are generally produced in lithographical processes [4].

(a)   (b)   (c)
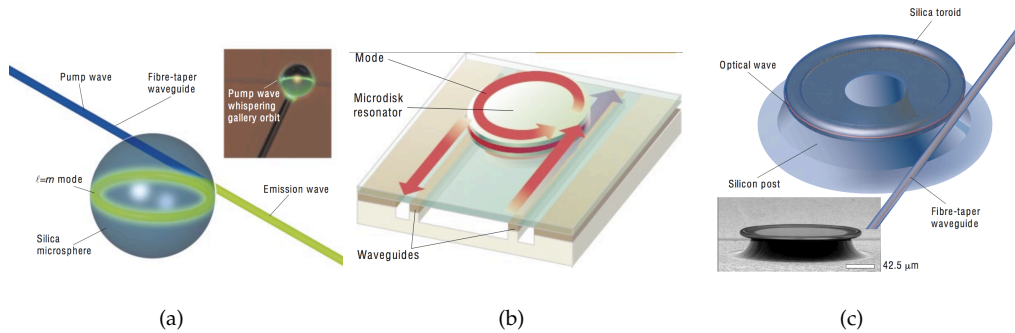
Figure 4.14: Different geometries to implement whispering gallery resonators: (a) a spherical, (b) cylindrical, (c) toroid microcavity. Reproduced from Ref.[2].

To couple the light efficiently in and out a whispering gallery, one can make use of a tapered optical fibre (Fig.4.14). Provided there is good phase synchronisation and sufficient overlap of the field, light will tunnel from the resonator into the fibre and vice-versa through frustrated

total internal reflection. Since this coupling efficiency is highly sensitive to the gap between fibre and cavity, other geometries have been suggested with a non symmetrical deformation. This gives rise to so-called "bow-tie" modes, as shown in Fig.4.15. The regions with higher radius of curvature will produce longer evanecent tails, enhancing the output coupling into the fibre.
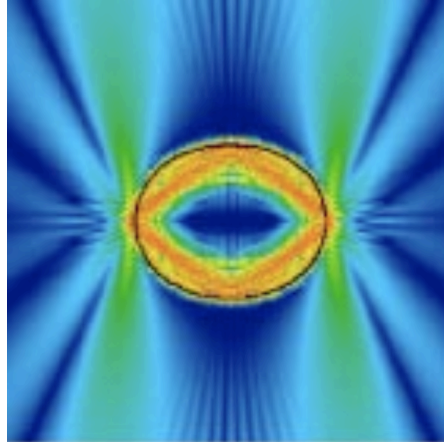
Figure 4.15: Alternative desings of microcavities, depart from the sperical symmetry to enhance several properties. A bow-tie resonator, reproduced from Ref.[15].

The possible applications of these structures are diverse, which is why any enumeration will be incomplete. This following list should therefore be read as an argument for the great potential of these little structures.

- In this chapter, we introduced microresonators as confining elements of electromagnetic energy. This can of course be exploited to implement them as optical buffers. Such devices would pave the way for future all-optical data processing [16]. Miniaturisation of such microresonators is one of the biggest challenges in this area [17].

- Ultra high Q resonators can be used to design lasers with low lasing threshold, being inversely proportional to the reflectivity inside the cavity. The major problem of these lasers is the isotropic emission of light. This issue is resolved using deformed shapes, as shown in Fig. 4.15. Ref. [18] suggests such a deformed microdisk laser, combining unidirectional emission with low threshold power.

- It should come as no surprise that microresonators have several purposes in the telecommunication industry[19], the optical application field par excellence. Being frequency selective with a linewidth inversely proportional to Q (Fig.4.11), microresonators are well-suited as optical filters. It is, however, not a trivial problem to combine accurate tunability with high Q. Next to these filters, whispering gallery resonators can also be used in other telecom components such as switches and modulators.

- Small mode volumes generate high nonlinearities, even when the materials have low nonlinear properties as is the case for silica. The highest intensities occur close to the surface, suggesting microspheres with surface nonlinear processes [20].

- The high sensitivity of these resonators to surface perturbations can be employed to make sensors. By measuring changes in the transmission characteristics of the whispering gallery, one can make photonic biosensors that detect the presence of biological pathogens near the resonators surface [21] or acceleration sensors that convert an applied force in a variation of the gap between a fibre and the resonator [22].

- More exotic optical phenomena can be observed when several microresonators are combined in one component. Socalled "Coupled Ring Optical Waveguides" offer the possibility to tailor the group velocity of the waveguide, making it possible to slow down light [23].

- Finally, we mention the use of dielectric microcavities in the field of cavity quantum electrodynamics (CavityQED). This research investigates how and why excited atoms behave differently when they are placed inside cavities. A well-known different behaviour is the Purcell effect, through which we can modulate the rate of spontaneous emission inside a cavity. Another exciting phenomenon occurs under certain circumstances, where an atom with its surrounding cavity strongly interacts to combine into a atom-cavity state (polariton), which is a mode where energy is bouncing back and forward between the electromagnetic waves and the atoms excitation inside the cavity [24].

References

[1] L. Novotny and B. Hecht, *Principles of Nano-Optics*, Cambridge University Press, New York, 2006.

[2] K. J. Vahala, "Optical microcavities," *Nature* **424**, 839–846, 2003.

[3] J. Vuckovic and Y. Yamamoto, "Photonic crystal microcavities for cavity quantum electrodynamics with a single quantum dot," *App. Phys. Lett.* **82**, 2374–2376, 2003.

[4] A. V. Kavolkin, J. J. Baumberg, G. Malpuech, and F. P. Laussy, *Microcavities*, Oxford University Press, Oxford, 2006.

[5] E. Born and M. Wolf, *Principles of Optics*, Cambidge University Press, Cambridge, 1986.

[6] J. D. Jackson, *Classical Electrodynamics (3rd edition)*, Wiley, New York, 1999.

[7] L. Rayleigh, "The problem of the whispering gallery," *ScientificPapers* **5**, 617–620, 1912.

[8] R. K. Chang and A. J. Campillo, *Optical Processes In Microcavities*, World Scientific Publishing, Singapore, 1996.

[9] M. Abramowitz and I. A. Stegun, *Handbook of Mathematical Functions with Formulas, Graphs, and Mathematical Tables*, Dover, New York, 1964.

[10] T. J. A. Kippenberg, *Nonlinear Optics in Ultra-high-Q Whispering-Gallery Optical Microcavities*. PhD thesis, California Institute of Technology, 2004.

[11] J. E. Heebner, T. C. Bond, and J. S. Kallman, "Generalized formulation for performance degradations due to bending and edge scattering loss in microdisk resonators," *Opt. Express* **15**, 4452–4473, 2007.

[12] J. Mathews and R. L. Walker, *Mathematical methods of physics*, W.A. Benjamin, New York, 1970.

[13] P. T. Leung and K. M. Pang, "Completeness and time-independent perturbation of morphology-dependent resonances in dielectric spheres," *J. Opt. Soc. Am. B.* **13**, 805–817, 1995.

[14] T. Myint-U, *Partial Differential Equations of Mathematical Physics*, North Holland, New York.

[15] J. U. Nockel and A. D. Stone, "Ray and wave chaos in asymmetric resonant optical cavities," *Nature* **385**, 45–47, 1997.

[16] A. B. Matsko, *Practical Applications Of Microresonators In Optics And Photonics*, Taylor and Francis, London, 2009.

[17] D. K. Armani, T. J. Kippenberg, S. M. Spillane, and K. J. Vahala, "Ultra-high-Q toroid microcavity on a chip," *Nature* **421**, 925–928, 2003.

[18] Q. H. Song, H. Cao, B. Y. Liu, S. T. Ho, W. Fang, and G. S. Solomon, "Chaotic microcavity laser with low threshold and unidirectional output," *ArXiv e-prints* , 2008.

[19] A. B. Matsko, A. A. Savchenkov, V. S. Ilchenko, and L. Maleki, "Review of applications of whispering-gallery-mode resonators in photonics and nonlinear optics," *The Interplanetary Network Progress Report* **42-162**, 1–51, 2005.

[20] G. Kozyreff, J. L. Dominguez Juarez, and J. Martorell, "Whispering-gallery-mode phase matching for surface second-order nonlinear optical processes in spherical microresonators," *Phys. Rev. A* **77**, 043817, 2008.

[21] R. W. Boyd and J. E. Heebner, "Sensitive disk resonator photonic biosensor," *Appl. Opt.* **40**, 5742–5747, 2001.

[22] J. P. Laine, *Design and applications of optical microsphere resonators*. PhD thesis, Helsinki University of Technology Publications in Engineering Physics, 2003.

[23] A. Yariv, Y. Xu, R. K. Lee, and A. Scherer, "Coupled-resonator optical waveguide: a proposal and analysis," *Opt. Lett.* **24**, 711–713, 1999.

[24] H. J. Kimble, "Strong interactions of single atoms and photons in cavity QED," *Physica Scripta* **76**, 127–137, 1998.

CHAPTER 5

Microcavities in
Transformation Optics

In this chapter, we will look for microcavities within the field of transformation
optics. First, we will examin the ability of an invisibility cloak to serve as an optical
cavity. This section will introduce a general dispersion equation which is valid for
every transformation medium, performing a radial coordinate transformation. We
will find that the ideal invisbility cloak is not capable of confining light, whereas
a perturbed version has high-quality solutions, from wich none is subwavelength.
Secondly, we will use the tools of transformation optics to design a device that
confines perfectly electromagnetic energy of any wavelength. This device reduces
the wavelength inside the cavity with material parameters that tend to infinity.

5.1 The Invisibility Cloak Revisited

In chapter 3, we introduced the concept of an invisibility cloak. Such a device turns a finite
region in space invisible by guiding the light around it. For an ideal cloak, it is impossible for
light of any wavelength to enter the cloaked region. But if no light can go in, then perhaps no
light can go out? This idea suggests that we could approach an invisibility cloak as an optical
cavity.

### 5.1.1 The Cavity Setup

We will calculate the confined modes of such a cloak cavity with the formalism that we in-
troduced in chapter 4. As we explained in that chapter, we will calculate these modes in the
two-dimensional case for TE polarisation. The setup of such a cavity is shown in Fig. 5.1. The
modes of this system are calculated by solving Maxwell's equations in the different regions

(I, II, III) and match them with the boundary conditions. In regions (I) and (III), the fields are solutions of Helmholz' equation in vacuum and, according to the reasoning in chapter three, the electric field is given by:

$$E_{\mathrm{I}}^z(\rho, \phi) = A \, J_m(k_0\rho) \, e^{im\phi}, \tag{5.1}$$

$$E_{\mathrm{III}}^z(\rho, \phi) = D \, H_m^{(1)}(k_0\rho) \, e^{im\phi}, \tag{5.2}$$

with A and D complex constants, $k_0 = \omega/c$, and $m \in \mathbb{Z}$. The solutions inside region (II) are calculated in the next section.
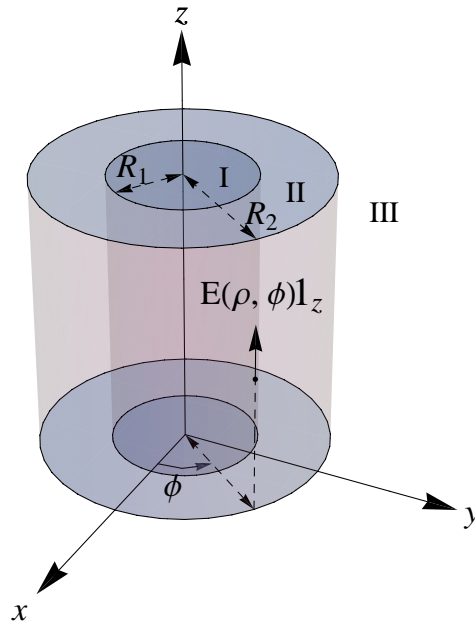
Figure 5.1: A cylindrical cloak (II), with inner radius R_1 and outer radius R_2, surrounded by vacuum (III), includes a cloaked region (I) where electromagnetic fields might be trapped. Unless it is specified differently, we will assume $R_2 = 2R_1$.

5.1.2 Inside a Cylindrical Invisibility Cloak

To calculate the solutions in region (II), we will derive the constitutive parameters $\epsilon^i_{\ j}$ and $\mu^i_{\ j}$ of the cylindrical cloak and insert thems in Maxwell's equations. In the cylindrical case, the electromagnetic coordinates (ρ', ϕ', z') are mapped on the physical coordinates (ρ, ϕ, z) by the transformation

$$\begin{aligned} \rho' &= f(\rho), \\ \phi' &= \phi, \\ z' &= z. \end{aligned} \tag{5.3}$$

Below, we will gradually calculate the material parameters that implement such a transformation. The metric of electromagnetic space is given by

$$ds^2 = d\rho'^2 + \rho'^2 d\phi'^2 + dz'^2, \tag{5.4}$$

and, expressed in the physical coordinates (ρ, ϕ, z):

$$ds^2 = f'(\rho)^2 d\rho^2 + f(\rho)^2 d\phi^2 + dz^2.^* \tag{5.5}$$

In the cylindrical case, the components of g_{ij} are thus given by:

$$
\begin{array}{lll}
g_{\rho\rho} = f'(\rho)^2, & g_{\rho\phi} = 0, & g_{\rho z} = 0, \\
g_{\phi\rho} = 0, & g_{\phi\phi} = f(\rho)^2, & g_{\phi z} = 0, \\
g_{z\rho} = 0, & g_{z\phi} = 0, & g_{zz} = 1,
\end{array}
\tag{5.6}
$$

which in turn leads to the expressions

$$
\begin{array}{lll}
g^{\rho\rho} = \dfrac{1}{f'(\rho)^2}, & g^{\rho\phi} = 0, & g^{\rho z} = 0, \\[2mm]
g^{\phi\rho} = 0, & g^{\phi\phi} = \dfrac{1}{f(\rho)^2}, & g^{\phi z} = 0, \\[2mm]
g^{z\rho} = 0, & g^{z\phi} = 0, & g^{zz} = 1,
\end{array}
\tag{5.7}
$$

Since permeability equals the permittivity, we will restrict ourselves to this last parameter. Using Eq. (3.69), we then calculate that

$$
\begin{array}{lll}
\epsilon^{\rho\rho} = \dfrac{f(\rho)}{\rho f'(\rho)}, & \epsilon^{\rho\phi} = 0, & \epsilon^{\rho z} = 0, \\[2mm]
\epsilon^{\phi\rho} = 0, & \epsilon^{\phi\phi} = \dfrac{f'(\rho)}{f(\rho)\rho}, & \epsilon^{\phi z} = 0, \\[2mm]
\epsilon^{z\rho} = 0, & \epsilon^{z\phi} = 0, & \epsilon^{zz} = \dfrac{f'(\rho)f(\rho)}{\rho}.
\end{array}
\tag{5.8}
$$

In terms of an arbitrary (continuous) transformation function f, the nonzero components of $\epsilon^i{}_j$ are then

$$
\begin{aligned}
\epsilon^{\rho}{}_{\rho} &= \frac{f(\rho)}{\rho f'(\rho)}, \\
\epsilon^{\phi}{}_{\phi} &= \frac{\rho f'(\rho)}{f(\rho)}, \\
\epsilon^{z}{}_{z} &= \frac{f(\rho)f'(\rho)}{\rho}.
\end{aligned}
\tag{5.9}
$$

The components of the permeability $\mu^i{}_j$ are identical to those of the permittivity $\epsilon^i{}_j$. Fig. 5.2 plots these parameters in the case of a simple linear transformation function, satisfying $f(R_1) = 0$ and $f(R_2) = R_2$:

$$f : [R_1, R_2] \to \mathbb{R}^+ : \rho \mapsto \rho' = \frac{R_2}{R_2 - R_1}(\rho - R_1). \tag{5.10}$$

---

*Here, $f'(\rho)$ stands for the derivative of f with respect to ρ.

This function and its corresponding two-dimensional plot are shown in Fig. 3.8 and Fig. 3.6. We encounter a singularity at the inner boundary R_1, which is even worse than in the spherical case (shown in Fig. 3.9). Independent of the transformation function f, $\epsilon^\rho{}_\rho(R_1)$ and $\mu^\rho{}_\rho(R_1)$ will be zero and $\epsilon^\phi{}_\phi(R_2)$ and $\mu^\phi{}_\phi(R_2)$ will always tend to infinity.[*]
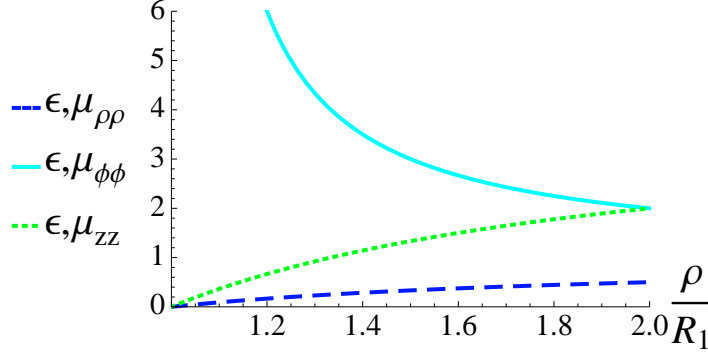
Figure 5.2: Material parameters constituting a cylindrical inivisibility cloak, defined by Eq. (3.75). At the inner boundary, the radial and the z-component of the material's response are zero. The angular component goes to infinity.

Since the cloak is built with anisotropic materials, we cannot use Helmholtz' equation to find the field solutions. Let us therefore return to Maxwell's equations and try to find a similar expression. In the absence of free charges ρ and currents $\mathbf{J}$, the laws of Faraday and Ampère-Maxwell are

$$\nabla \times \mathbf{E} = -\frac{\partial \mathbf{B}}{\partial t}, \qquad\qquad \nabla \times \mathbf{E_0} = i\omega \mathbf{B_0}, \qquad\qquad (5.11)$$

$$\nabla \times \mathbf{H} = \frac{\partial \mathbf{D}}{\partial t}, \qquad\qquad \nabla \times \mathbf{H_0} = -i\omega \mathbf{D_0}, \qquad\qquad (5.12)$$

where we assumed a harmonic time-dependency $\mathbf{E} = \mathbf{E_0}\, e^{-i\omega t}$. Bearing in mind the TE polarisation $\mathbf{E_0} = E^z\, \mathbf{1_z}$, we can expand Eq. (5.11) in cylindrical coordinates, yielding:

$$B^\rho = \frac{1}{i\omega\rho}\frac{\partial E^z}{\partial \phi},$$

$$B^\phi = -\frac{1}{i\omega}\frac{\partial E^z}{\partial \rho}, \qquad\qquad (5.13)$$

$$B^z = 0.$$

These expressions can be reinserted in Eq. (5.12), using the constitutive equations $B^i = \mu_0\mu^i{}_j H^j$ and $D^i = \epsilon_0\epsilon^i{}_j E^j$:

$$\frac{1}{\rho}\frac{\partial}{\partial \rho}\left(-\frac{\rho}{i\omega\mu_0\mu^\phi{}_\phi}\frac{\partial E^z}{\partial \rho}\right) - \frac{1}{\rho}\frac{\partial}{\partial \phi}\left(\frac{1}{i\omega\rho\mu_0\mu^\rho{}_\rho}\frac{\partial E^z}{\partial \phi}\right) = -i\omega\epsilon_0\epsilon^z{}_z E^z. \qquad (5.14)$$

---

[*]Suppose f a is nonzero with $f(R_1) = 0$. If $f'(R_1) \neq 0$, then $(f(R_1)/f'(R_1)) = 0$. If $f'(R_1) = 0$, then $f(R_1)/f'(R_1) = f'(R_1)/f''(R_1)$, which is zero since we can repeat this reasoning until $f^{(n)}(R_1) \neq 0$. Such an integer n exists since f is nonzero.

This equation contains only the unknown function E^z and can be simplified by introducing the free space wavenumber $k_0 = \omega/c$. In this way, we obtain the analogue of Helmholtz' equation in an anisotropic material with zero non-diagonal elements, which is valid for TE polarisation:

$$\frac{1}{\rho}\frac{\partial}{\partial\rho}\left(\frac{\rho}{\mu^{\phi}_{\phi}}\frac{\partial E^z}{\partial\rho}\right) + \frac{1}{\rho}\frac{\partial}{\partial\phi}\left(\frac{1}{\rho\mu^{\rho}_{\rho}}\frac{\partial E^z}{\partial\phi}\right) + k_0^2\epsilon^z_{\,z}E^z = 0. \tag{5.15}$$

Notice that, for this polarisation, $(\mu^{\rho}_{\,\rho}, \mu^{\phi}_{\,\phi}, \epsilon^z_{\,z})$ are the only parameters of importance. The other components $(\epsilon^{\rho}_{\,\rho}, \epsilon^{\phi}_{\,\phi}, \mu^z_{\,z})$ matter for TM polarised waves. The number of nontrivial material parameters of an invisibility cloak can thus be reduced if one considers a single polarisation. The solutions inside the cloaking material (region II) can now be found by solving this equation, with the constitutive parameters of the cylindrical cloak, as given in Eq. (5.9). After some elementary rearrangements, we end up with

$$\frac{f(\rho)}{f'(\rho)}\frac{\partial}{\partial\rho}\left(\frac{f(\rho)}{f'(\rho)}\frac{\partial E^z}{\partial\rho}\right) + \frac{\partial^2 E^z}{\partial\phi^2} + k_0^2 f^2(\rho)E^z = 0. \tag{5.16}$$

As usual, the solutions will have a harmonic angular dependency. The radial part of this equation can be reduced to the Bessel equation in the variable $\rho' = f(\rho)$ and so we know that the solutions inside the cloak are given by:

$$E^z_{\text{II}}(\rho, \phi) = \left[B\,J_m(k_0 f(\rho)) + C\,Y_m(k_0 f(\rho))\right]e^{im\phi}. \tag{5.17}$$

The components of the magnetic field can be found from Eq. (5.18) in combination with Eq. (5.9), resulting in

$$\begin{aligned}
H^{\rho} &= \frac{1}{i\omega\mu_0}\frac{f'(\rho)}{f(\rho)}\frac{\partial E^z}{\partial\phi}, \\
H^{\phi} &= -\frac{1}{i\omega\mu_0}\frac{f(\rho)}{\rho f'(\rho)}\frac{\partial E^z}{\partial\rho}, \\
H^z &= 0.
\end{aligned} \tag{5.18}$$

5.1.3 The Dispersion Relation

The solution derived in the previous section can now be matched with the vacuum solutions. Implicitly, we have already applied some boundary conditions: the fields are finite in the origin, have angular continuity and obey Sommerfeld's radiation condition. The dispersion relation can then be found by additionally imposing the electromagnetic boundary conditions. As shown in the previous chapter, the tangential components of the electric field (E^z) and magnetic field (H^{ϕ}) must be continuous. When we apply these conditions at both boundaries ($\rho = R_1$) and ($\rho = R_2$),

we find the following set of four independent equations:

$$A\, J_m(k_0 R_1) = B\, J_m(k_0 f(R_1)) + C\, Y_m(k_0 f(R_1)),$$ (5.19)

$$A\, J'_m(k_0 R_1) = B\, \frac{f(R_1)}{R_1} J'_m(k_0 f(R_1)) + C\, \frac{f(R_1)}{R_1} Y'_m(k_0 f(R_1)),$$ (5.20)

$$B\, J_m(k_0 f(R_2)) + C\, Y_m(k_0 f(R_2)) = D\, H^{(1)}_m(k_0 R_2),$$ (5.21)

$$B\, \frac{f(R_2)}{R_2} J'_m(k_0 f(R_2)) + C\, \frac{f(R_2)}{R_2} Y'_m(k_0 f(R_2)) = D\, H'^{(1)}_m(k_0 R_2).$$ (5.22)

The equations involving the magnetic field are simplified using the relation $f'(\rho)/\mu^{\phi}_{\phi} = f(\rho)/\rho$, which is derived from Eq. (5.9). Note that Eqs. (5.19)-(5.22) are valid for any transformation device, performing a radial coordinate transformation $\rho' = f(\rho)$ between R_1 and R_2. Setting the determinant of this set equal to zero generates the dispersion relation of the system. If the cloaking device is 'perfect', i.e., $f(R_1) = 0$ and $f(R_2) = R2$, *no modes exist inside the cloaking region*. This can be understood from the fact that the modes of a dielectric cavity are related to the poles of the scattering factor $S(\omega)$[1]. This frequency-dependent factor indicates the amplitude of the scattered wave when the device is probed with one unit of incoming wave. An ideal invisibility cloak has a scattering factor $S(\omega) = 0$, which has no poles, prohibiting the existence of confined modes.

However, when we apply a little perturbation on the parameters, making the cloak less ideal, there might be solutions of the dispersion relation. We apply a little perturbation ΔR at the inner boundary. The cloaking material will then cover the region $[R_1 + \Delta R, R_2]$, departing from the ideal situation since $f(R_1 + \Delta R) \neq 0$. This is also useful from a practical point of view, since we slice off the singular inner boundary of the cloak. The resulting system indeed provides cavity modes at well-defined frequencies. This is shown in Fig. 5.3.
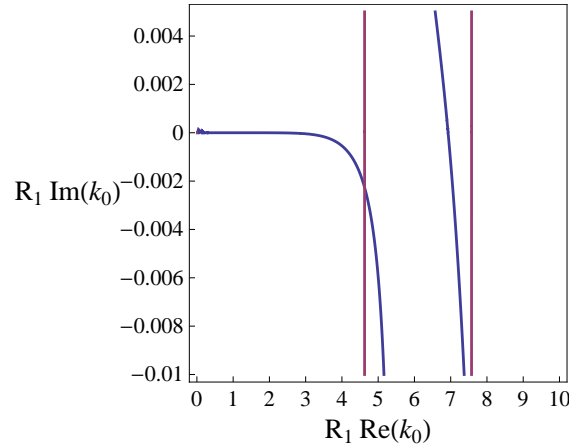
Figure 5.3: Contour plot of the dispersion relation defined by Esq. (5.19)-(5.22), with parameters $\Delta R = 0.1R_1, R_2 = 2R_1$, and $m = 3$. The quality factor Q depends on the perturbation ΔR. The first intersection of this plot: $k_0 R_1 = 4.63 - 2.26 \cdot 10^{-3}\, i$ has $Q \approx 10^3$.

The solutions are discrete and have qualitatively the same properties as the solutions of a dielectric cylinder. As the perturbation ΔR becomes smaller, the Q-factor grows and can become
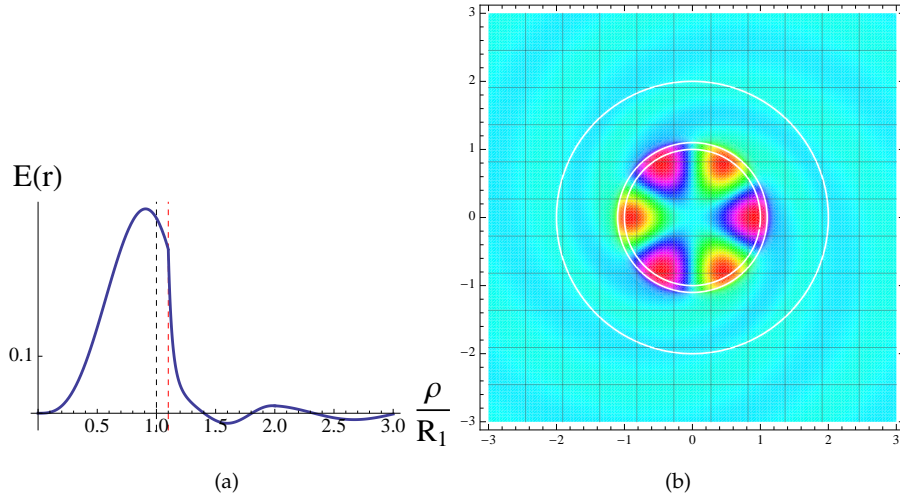
Figure 5.4: The electric field distribution inside the cavity, corresponding to the first solution in Fig. 5.3. The cross-sectional plot (a) and the density plot (b) clearly demonstrate how the field is concentrated in the cloaked region (I). The red, dashed lines in the cross-sectional plot indicate the boundaries R_{in}, R_2 of the perturbed cloaking device. The black dashed line is drawn at the inner boundary R_1 of the perfect cloaking device.

very large: $\Delta R = 10^{-3}$ gives a mode (mode numbers $m = 3, \nu = 1$) with $Q \approx 10^{17}$. There are, however, no subwavelength modes within this system. This might sound paradoxal with what we said earlier about the cloak being frequency-independent, although it is not the case: an ideal cloak has no modes insides the cloaked region—which is indeed frequency independent— whereas a perturbed cloak does not obey the rules of transformation optics and thus has specific resonances above a threshold frequency.

5.2 A Hyperbolic Map

The invisibility cloak is somewhat disappointing as an optical cavity. The cloak only supports confined modes when it is perturbed. Although these modes can have high quality factors, they are discrete and certainly not subwavelength. This should not temper our enthusiasm. We will leave the cloak behind and try to design an ideal cavity within the framework of transformation optics.

5.2.1 Defining the Transformation

An ideal cavity confines the electromagnetic energy in a finite (small) region of space for infinite time. Translated in terms of electromagnetic and physical space, this could be achieved by mapping the entire electromagnetic space on a finite region in physical space. Such a map can be constructed with a hyperbolic function which goes to infinity in a finite point. We will therefore

(a)   (b)
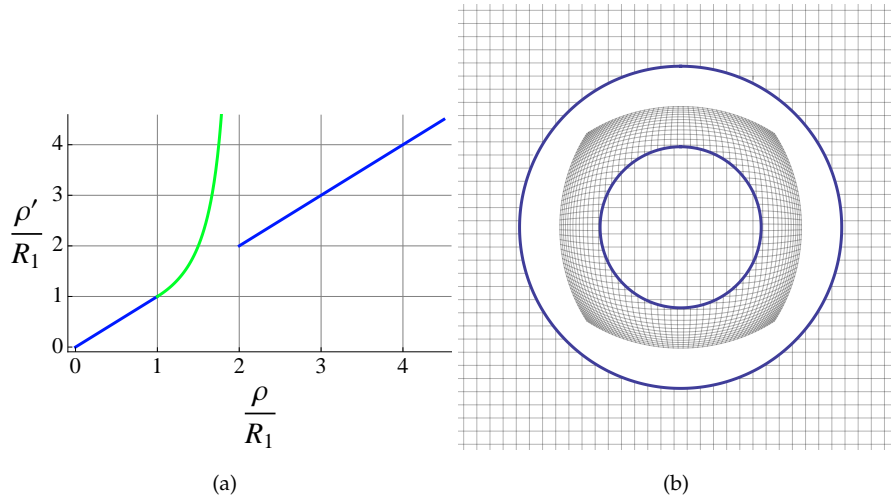
Figure 5.5: The coordinate transformation of a hyperbolic map. (a) With a hyperbolic transformation function as defined in Eq. (5.24), the interval $[R_1, R_2]$ in the physical radial coordinate ρ covers the interval $[R_1, +\infty]$ in the electromagnetic radial coordinate ρ'. The corresponding coordinate transformation is shown in (b). The coordinate lines match vacuum at the inner boundary and get squeezed together towards the outer boundary R_2.

consider again a device as shown in Fig. 5.1, which performs a coordinate transformation between (x^i) and $(x^{i'})$:

$$
\begin{aligned}
\rho' &= f(\rho), \\
\phi' &= \phi, \\
z' &= z,
\end{aligned}
$$

$$(5.23)$$

where f is defined by

$$f : [R_1, R_2] \rightarrow \mathbb{R}^+ : \rho \mapsto \rho' = \frac{R_1(R_1 - R_2)}{\rho - R_2}. \tag{5.24}$$

This function, shown in Fig. 5.5, has a hyperbolic shape and becomes infinite at the outer boundary of the device R_2, and is matched at the inner boundary R_1 with vacuum. The matching at the inner boundary assures a smooth transition of the waves and since there is nothing "beyond infinity", the electromagnetic energy can not escape this device. The corresponding coordinate transformation is shown in the same figure. The cartesian coordinate lines in physical space become denser as we approach the outer radius R_2. Although they stop in the plot at a certain position, theoretically the grid would have an infinite number of lines within the transformation medium. An equivalent transformation has been proposed from a different point of view to design a perfectly matched layer for numerical software [2].

5.2.2 Material Parameters

The hyperbolic transformation from Eq. (5.24) is implemented with an anisotropic, inhomogenious material. The components of the permittivity and permeability can be found by inserting this function in Eq. (5.9), yielding:

$$\epsilon^{\rho}{}_{\rho} = \frac{R_2 - \rho}{\rho},$$
$$\epsilon^{\phi}{}_{\phi} = \frac{\rho}{R_2 - \rho}, \tag{5.25}$$
$$\epsilon^{z}{}_{z} = \frac{-R_1^2(R_1 - R_2)^2}{(\rho - R_2)^3}.$$
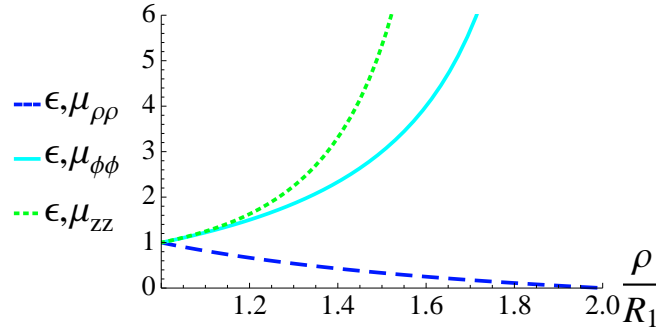
Figure 5.6: Material parameters constituting a hyperbolic transformation defined by Eq. (5.24). At the outer boundary, the radial component is zero. The other two components grow to infinity as they approach the outer boundary.

5.2.3 Results

The modes of this system are calculated with the traditional procedure. The dispersion relation is actually the same as in Sec. 5.1.3, where we have to use the hyperbolic function f of Eq. (5.24) instead of the transformation function of the cylindrical cloak. To evaluate the deteminant of Eqs. (5.19)-(5.22) numerically, we have to introduce a perturbation at the outer boundary to eliminate the infinity at $f(R_2)$. Therefore, we calculate the modes of the device which performs the transformation Eq. (5.24) up to a certain value $R_{\text{out}} = R_2 - \Delta R$. So actually, we cut off a rim at the outer boundary with thickness ΔR. The modes of this system can be determined by the solutions of

$$A\, J_m(k_0 R_1) = B\, J_m(k_0 R_1) + C\, Y_m(k_0 R_1), \tag{5.26}$$
$$A\, J'_m(k_0 R_1) = B\, J'_m(k_0 f(R_1)) + C\, Y'_m(k_0 R_1), \tag{5.27}$$
$$B\, J_m(k_0 f(R_{\text{out}})) + C\, Y_m(k_0 f(R_{\text{out}}) = D\, H_m^{(1)}(k_0 R_{\text{out}}) \tag{5.28}$$
$$B\, \frac{f(R_{\text{out}})}{R_{\text{out}}} J'_m(k_0 f(R_{\text{out}})) + C\, \frac{f(R_{\text{out}})}{R_{\text{out}}} Y'_m(k_0 f(R_{\text{out}})) = D\, H'^{(1)}_m(k_0 R_{\text{out}}). \tag{5.29}$$

The corresponding contour plot is shown in Fig. 5.7, with $\Delta R = 0.005$ and $m = 3$. The solutions (at the intersections of a blue and a red curve) have a high quality factor Q, which grows as ΔR becomes smaller, at the same time diminishing the spacing between the solutions. In the limit $\Delta R \to 0$, every real ω is a solution, indicating perfect confinement for every wavelength.
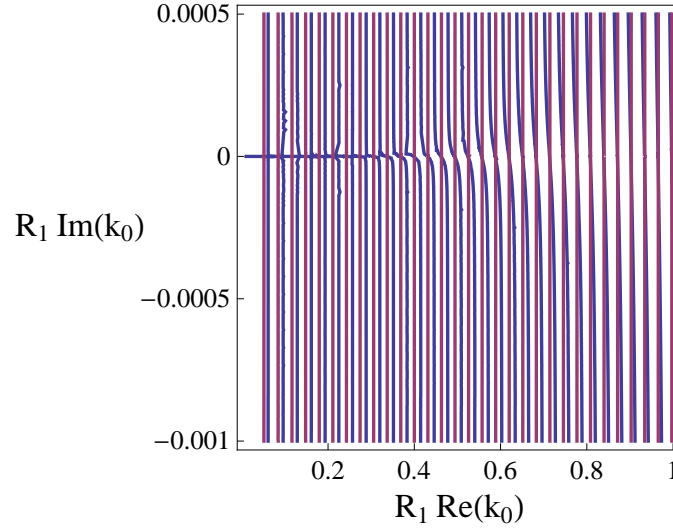

Figure 5.7: Contour plot of the dispersion relation defined by Eq. (5.26)-Eq. (5.29), with parameters $\Delta R = 0.01 R_1, R_2 = 2 R_1$, and $m = 3$. The quality factor is very high and the solutions are discrete but come closer to each other as ΔR becomes smaller.

In Fig. 5.8, we plot the cross-sectional and two-dimensional plot of such a mode inside the cavity, corresponding to the solution $k_0 R_1 = 1.00 - 4.81 \cdot 10^{-5}$ i. We immediately notice two important properties: (i) the field is almost completely situated in the transformation medium, which sounds reasonable since this medium contains the electromagnetic interval $[R_1, +\infty]$, whereas the inner disk (region I) only occupies the electromagnetic interval $[0, R1]$ and (ii) the wavelength of the electric field becomes smaller towards the outer radius R_2. This is of course due to the increasing index of refraction inside the medium.

5.2.4 Conclusion

Judging from these previous results, this hyperbolic design might seem the ideal optical cavity we are looking for. Although this device achieves perfect confinement at every wavelength (or approximates it arbitrarily good), we should look back on the materials with which it is implementend in Fig. 5.6. Since the wavelength is becoming extremely small within the device, it is not conventional to say that this device confines subwavelength modes. The structure, however, is conceptually of great importance: when the constitutive parameters are not bounded to a finite value, it is possible to confine electromagnetic energy, independent of the wavelength or polarisation, something which is not possible with traditional optical components.
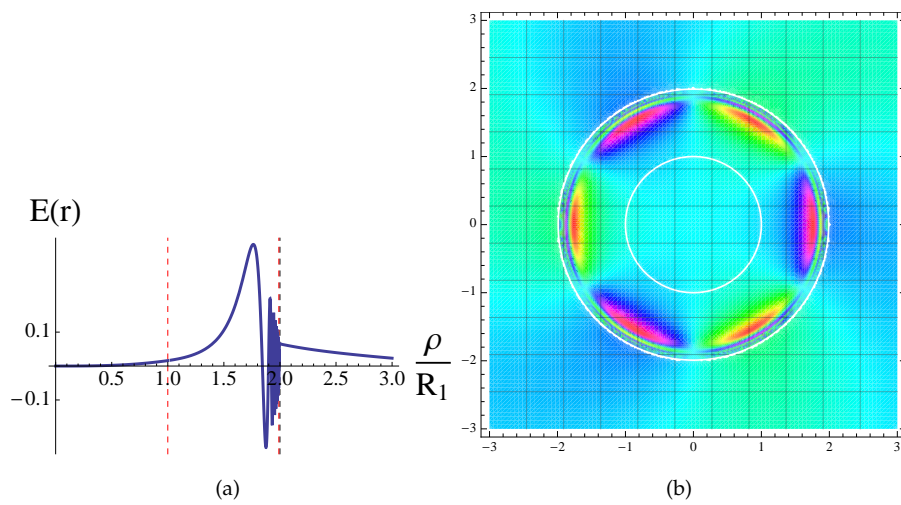
Figure 5.8: The electric field distribution inside the cavity, corresponding to the solution $k_0 R_1 = 1.00 - 4.81 \cdot 10^{-5}\,$i. The cross-sectional plot (a) and the density plot (b) and show how almost the entire field is concentrated in the transformation medium (II). The red, dashed lines in the cross-sectional plot indicate the boundaries R_1, R_{out} of the perturbed cloaking device. The black, dashed line is drawn at the inner boundary R_1 of the perfect cloaking device.

References

[1] R. K. Chang and A. J. Campillo, *Optical Processes In Microcavities*, World Scientific Publishing, Singapore, 1996.

[2] N. A. Zharova, I. V. Shadrivov, and Y. S. Kivshar, "Inside-out electromagnetic cloaking," *Opt. Express* **16**, 4615–4620, 2008.

CHAPTER 6

Subwavelength Cavities

In this chapter we will introduce different transformation media that confine true subwavelength modes. We will start by introducing *the perfect cavity*, whose name originates from the conceptual resemblence with the perfect lens. This structure is able to confine light of any wavelength in combination with an infinite quality factor. We will, however, encounter its weak point, which is an extreme sensitivity to perturbations. Subsequently, we will try to remove this singular nature by introducing a well-designed derivative design of this perfect cavity. This structure will have one very good confined mode, whose frequency can be tuned into deep subwavelength regions.

6.1 Introduction

In the previous chapter, we introduced a transformation medium that is capable of storing electromagnetic energy of any wavelength for an infinite time. A perturbed version of this device with less extreme parameters approximates these characteristics quite good. There were, however, two major drawbacks: the energy is almost entirely situated inside the transformation medium and the the wavelength inside this region (II) becomes extremely small. This results from the fact that some components of the constitutive parameters become very large inside the device. We would like to design a device with the same ideal properties — confining subwavelength light for an infinite time — built with parameters that do not grow to infinity. This would improve the field distribution inside the cavity, but even more importantly, it would confine true subwavelength modes.

6.2 The Perfect Cavity

6.2.1 The Transformation Function

Let us briefly return to the example of the invisibility cloak, Sec. 3.4.1. The electromagnetic fields are excluded from the cloaked region by mapping the physical radius R_1 on origin of the electromagnetic space. The radial coordinate in electromagnetic space is defined on the interval $[0, +\infty]$, and there is nothing beyond this range. In the example of the hyperbolic map of Sec. 5.2, we have designed a cavity that mapped the entire electromagnetic space on a finite physical space. We could, however, design a cavity from a cloaking perspective and design a device that cloaks the volume surrounding the device, instead of the volume inside the device. Such a device should smoothly guide the electromagnetic waves such that they never enter the surrounding space. Let us first consider the two-dimensional case. The setup, which is the same as in the previous chapter, is shown in Fig. 5.1. Since we want to cloak away region (III), we will use a radial coordinate transformation, mapping the physical coordinates (ρ, ϕ, z) on the electromagnetic coordinates (ρ', ϕ', z') as defined by Eq. (5.3). To achieve perfect cloaking of region (III), the radial tranformation function has to meet by the boundary conditions

$$f(R_1) = R_1, \tag{6.1}$$

$$f(R_2) = 0. \tag{6.2}$$

Here again, the actual shape of the function will have no implications on the cloaking performance. We will therefore consider the most trivial function satisfying the boundary conditions (6.1)-(6.2):

$$f : [R_1, R_2] \to \mathbb{R}^+ : \rho \mapsto \rho' = \frac{R_1}{R_1 - R_2}(\rho - R_2). \tag{6.3}$$

This coordinate transformation is shown in Fig. 6.1. As the radial coordinate gets folded, the corresponding coordinate lines in Cartesian coordinates follow closed loops: a particle moving along a vertical coordinate line in region (I), identified by a positive *x*-coordinate is bent to the right in the cloaking region and returns in the vacuum region on the same vertical line, staying bounded in this region for an infinite time.

6.2.2 Material Parameters

The cloaking material region (II) has to be built with materials whose parameters are imposed by the rules of transfomation optics. In case of a cylindrical setup, assuming the inner region to be vacuum, we can apply Eq. (5.9) in combination with the correct transformation function,
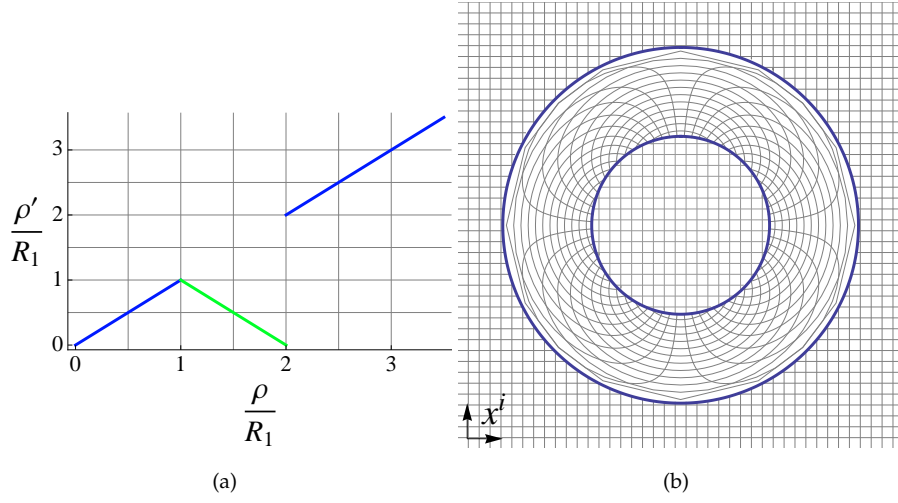
Figure 6.1: The coordinate transformation of the perfect cavity. The surrounding space is made invisible through a radial coordinate transformation that maps R_2 on the origin in electromagnetic space and it is matched with vacuum at R_1 (left). Expressed in Cartesian coordinates (x^i), the coordinate lines get folded back on themselves and compose closed curves, resembling the ears of Mickey Mouse (right).

Eq. (6.3). The nontrivial components of the material's response are then given by

$$\epsilon^\rho{}_\rho = \frac{\rho - R_2}{\rho},$$

$$\epsilon^\phi{}_\phi = \frac{\rho}{\rho - R_2},$$

$$\epsilon^z{}_z = \frac{R_1^2}{(R_1 - R_2)^2} \frac{\rho - R_2}{\rho}.$$

(6.4)

The variation of these components as a function of the physical coordinate ρ is shown in Fig. 6.2. These components have a negative sign, imposing the use of left-handed materials. From Eq. (5.9), one can derive that any transformation medium, satisfying Eqs. (6.1)-(6.2), will have a region with negative components. The same is true in the spherical or planar analogue. A folded map will always need an implementation of left-handed materials. The perfect lens from Sec. 3.4.2 is another example of such a map where space is folded and left-handed response is necessary.

Next, we notice the well-known behaviour at the bounday that is mapped on the origin. The radial components become zero, while the angular component tends to negative infinity. Although $\epsilon^z{}_z$ and $\mu^z{}_z$ also become zero with this partical choice of f, this is not a general property. We could, e.g., choose the transformation function f to be

$$f : [R_1, R_2] \to \mathbb{R}^+ : \rho \mapsto \rho' = \frac{R_1}{\sqrt{R_2^2 - R_1^2}} \sqrt{R_2^2 - \rho^2}.$$

(6.5)

71

This function satisfies the boundary conditions (6.1)-(6.2), but additionally solves the differential equation $f(\rho)f'(\rho)/\rho = $ Constant. This particular transformation would thus have a constant ϵ^z_z and μ^z_z [1]. For a three-dimensional spherical design, one can obtain from Eq. (3.85) that none of the material's components would become infinitely large in this design.
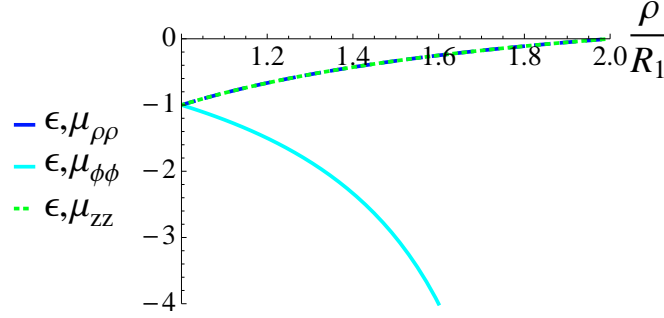
Figure 6.2: Material parameters constituting a perfect cavity, defined by Eq. (6.3). Next to the singularity at the outer boundary, which is the same as the singularity at the inner boundary for the traditional invisibility cloak, we notice that every component is negative, obligating the use of left-handed materials.

6.2.3 Results

As was the case in the previous chapter, the modes of this cavities are the solutions of Eqs. (5.19)-(5.22), where we have to insert $f(R_1) = R_1$ and $f(R_2) = 0$. Instead of evaluating the determinant of this set after performing a little perturbation, we will have a closer look at these equations in the limit of the ideal case:

$$A\, J_m(k_0 R_1) = B\, J_m(k_0 R_1) + C\, Y_m(k_0 R_1), \tag{6.6}$$

$$A\, J'_m(k_0 R_1) = B\, J'_m(k_0 R_1) + C\, Y'_m(k_0 R_1), \tag{6.7}$$

$$B\, \lim_{x \to 0} J_m(k_0 x) + C\, \lim_{x \to 0} Y_m(k_0 x) = D\, H^{(1)}_m(k_0 R_2), \tag{6.8}$$

$$B\, \lim_{x \to 0}\left[\frac{x}{R_2} J'_m(k_0 x)\right] + C\, \lim_{x \to 0}\left[\frac{x}{R_2} Y'_m(k_0 x)\right] = D\, H'^{(1)}_m(k_0 R_2). \tag{6.9}$$

These limits should be handled with care, since they contain expressions like $0 \times \infty$. When we assume the angular mode number $m \neq 0$, we can unambiguously evaluate these limits to be:

$$\lim_{x \to 0} J_m(k_0 x) = 0, \tag{6.10}$$

$$\lim_{x \to 0} Y_m(k_0 x) = -\infty, \tag{6.11}$$

$$\lim_{x \to 0}\left[\frac{x}{R_2} J'_m(k_0 x)\right] = 0, \tag{6.12}$$

$$\lim_{x \to 0}\left[\frac{x}{R_2} Y'_m(k_0 x)\right] = +\infty. \tag{6.13}$$

We can now reinsert these limits in the last two equations

$$B \times 0 + C \times -\infty = D \, H_m^{(1)}(k_0 R_2), \tag{6.14}$$

$$B \times 0 + C \times +\infty = D \, H_m^{\prime(1)}(k_0 R_2), \tag{6.15}$$

and we immediately obtain that this set only has solutions if $D = 0$ and $C = 0$, while there are no requirements on B. When we combine this with the equations at the first boundary, we derive that the initial set of four equations is equivalent to

$$A \, J_m(k_0 R_1) = B \, J_m(k_0 R_1), \tag{6.16}$$

$$A \, J_m'(k_0 R_1) = B \, J_m'(k_0 R_1), \tag{6.17}$$

$$C = D = 0. \tag{6.18}$$

This set imposes no constraints on k_0, which means that this cavity supports modes for every wavelength, even if the wavelength is bigger then the characteristic dimensions of the cavity. These modes are perfectly confined, since D equals zero, prohibiting any radiation to infinity and pushing Q to infinity. One might object that, since every k_0 solves the equation, there are also solutions with $Q \neq \infty$. These solutions $\omega = \omega' + i\omega''$ can be rejected by expressing a conservation of energy: in the absence of electromagnetic sources, absorption or gain, we can state that the electromagnetic energy density $w = 1/2Re(\mathbf{D}^* \cdot \mathbf{E} + \mathbf{B}^* \cdot \mathbf{H})$ satisfies [2]

$$\int w \, dV = \text{Constant}, \tag{6.19}$$

if the integration domain V covers the entire space. When the coefficient D is zero, and there are thus no fields outside the cavity in region (III), we can immediately deduce that the complex part of the frequency ω'' should be zero.

We are now able to plot the solutions of this perfect cavity. We can choose any real free-space wave vector k_0 and plot the solutions, using Eq. (5.17). It goes without saying that the most impressive examples are the subwavelength modes, where the field is confined within a region which is smaller than the wavelength inside the device. Therefore, we show such a mode ($k_0 R_1 = 0.01$) in Fig. 6.3. The cross-sectional plot (left) shows how the field is equally distributed in the vaccum region and the cloaking region. Moreover, the field's variation inside the cavity is the exact mirror image of the field in the vacuum region. This is, however, not a general property of the cavity. We could have chosen a different f, satisfying Eqs. (6.1)-(6.2), which would have generated a different field distribution inside region (II). This confirms what we have already mentioned in Sec. 3.4.1: the actual shape of f has no influence on the cavities performance. One can make well-considered choices for this function f to enhance the field distribution inside the transformation medium via Eqs. (5.17)-(5.18) or to relax the material's parameters to implement the structure, as discussed in Sec. 6.2.2.

We have made analogous calculations in the three-dimensional case. These calculations of the spherical perfect cavity are given in Appendix A.
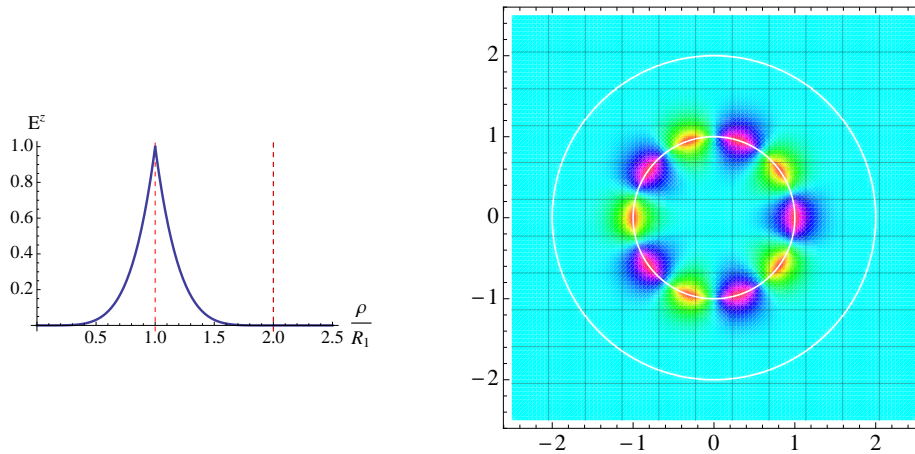
Figure 6.3: The electric field distribution inside the cavity, corresponding to a deep sub-wavelength solution $k_0 R_1 = 0.01$. The cross-sectional plot (left) shows how the electric field distribution inside the cavity is the mirrored image of the field inside the vacuum layer. This is due to the specific choice of the transformation function. There is no field radiated outside the cavity. The angular dependendy (right) resembles that of a traditional microcavity.

6.2.4 Discussion

The coordinate transformation Eq. (6.3), which cloaks away the surrounding space, indeed seems to implement a perfect cavity. The adjective *perfect* refers to the parameters defining the cavities quality: Q is infinite, since there is no radiation to infinity and characteristic dimensions of the cavity can be many orders of magnitude smaller than the confined wavelength. Next to the high Q and low V, the cavity exhibits a continuum of eigenmodes $\omega \in \mathbb{R}$. This property is interesting in some applications, such as optical buffers or supercontinuum generation, but is disadvantageous for optical filters or narrow linewidth light sources.

These previous parameters Q and V are bounded from a practical perspective: the photon lifetime inside the cavity will be finite due to the inevitable losses inside the left-handed material and the bandwidth of the confinement will be bounded by the dispersion relation of the used materials. The previous calculations inherently assumed dispersionless materials or monochromatic light. This does, however, not alter the fact that this design can be interesting from a conceptual point of view. The same is true for Pendry's design of a lens with subwavelength resolution.

As opposed to the hyperbolic map from Sec. 5.2 we notice a completely different mechanism of confinement: inside the cavity, a wave is confined if the cavity's size approximately equals a multiple number ν of the wavelength. The hyperbolic map reduced the wavelength of any mode to zero at the outer boundary, and thus fulfilling this condition. This newer design, however, does not alter the wavelength inside the device. Instead, it compensates the phase completely and so the multiple number ν of wavelengths equals zero, pushing the analogy with the perfect lens even further.

The reduction of Eqs. (6.6)-(6.9) to the trival Eqs. (6.16)-(6.17) was possible when we assumed the angular mode number $m \neq 0$. A mode without angular momentum cannot be confined within this cavity. Such a mode has a purely radial propagation component and in the absence of angular propagation it cannot be deflected to the left or to the right. The same is true for a traditional invisibility cloak. A ray which is directed exactly towards the center of the cloak does not know in which direction it should bend around the cloak.

In the previous calculations, we did not mention anything about the sensitivity of this cavity with respect to the material parameters. Essentially being a strange kind of cloak, one might expect the same kind of sensitivity: as material parameters deviate from the ideal values, an invisibility cloak retains its cloaking characteristics, albeit less performant [3]. The perfect cavity, however, suffers from an extreme sensitivity with respect to perturbations. When we perturbe the cavity by slicing a little rim ΔR from the outer boundary ($R_{out} = R_2 - \Delta R$), as we did in the previous chapters, we notice that the eigenmodes completely disappear. We demonstrate this with the contour plot of the perfect cavity shown in Fig. 6.4, where we have imposed the slightest perturbation of $\Delta R = 10^{-4}$ on the outer boundary. Such an enormous sensitivity also effects the use of numerical software, due to convergence problems which occur with the unavoidable discretisation error.

Recently, an analogous design has been proposed in combination with an invisibility cloak. [4],[5] When this structure is placed inside an invisibility cloak, it can defeat the cloaking effect, making the contained region visible again. This explains why it has been baptised as *the anti-cloak*.
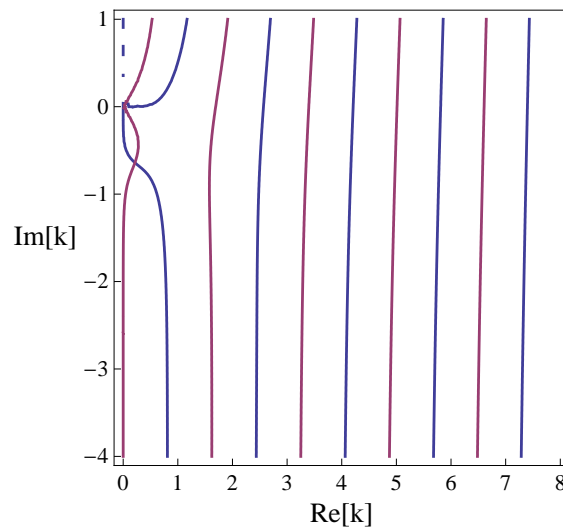
Figure 6.4: Contour plot showing the missing eigenfrequencies (no intersections) when we impose a little perturbation $\Delta R = 10^{-4}$ at the outer boundary.

Although it could be practically possible to achieve components of ϵ and μ equal to zero, there will always be dissipation, associated with the left-handed material, deteriorating the device's functionality. Once again, we can draw the analogy with the perfect lens, which has the same

type of sensitivity on its material parameters to achieve subwavelength resolution [6]. Together with the previous mentioned analogies, this justifies the chosen name *perfect cavity*.

6.3 A Non-Singular Version

Although the previous design theoretically achieves the perfect set of modes, it might not be useful in practical realisations due to its extreme sensitivity. Therefore, we have tried to eliminate this singularity by considering a derivative design of this cavity.

6.3.1 Designing the Perturbation

The sensitivity of the perfect cavity was situated at the outer boundary R_2. At this boundary, the material parameters are the most extreme: zero or infinity. We could, however, introduce an additional perturbation at the inner boundary R_1 by slicing of a little rim with thickness ΔR_1. The transformation material would thus be situated in the interval $[R_{in}, R_{out}]$, where $R_{in} = R_1 + \Delta R_1$ and $R_{out} = R_2 - \Delta R_2$. This would cause $f(R_{in}) \neq R_{in}$ and thus would eliminate the vacuum matching. Furthermore, we will choose to implement the transformation from Eq. (6.5), because it has $\epsilon^z{}_z = \mu^z{}_z = $ a constant. The transformation function f of this device would thus be given by:

$$f : [R_{in}, R_{out}] \to \mathbb{R}^+ : \rho \mapsto \rho' = \frac{R_1}{\sqrt{R_2^2 - R_1^2}} \sqrt{R_2^2 - \rho^2}. \tag{6.20}$$

The only difference with the transformation from Eq. (6.5), constituting a perfect cavity, is the domain on which this function is defined. In Fig. 6.5, we plot this new transformation. We note that in comparison with the perfect cavity, this transformation has two additional degrees of freedom: ΔR_1 and ΔR_2. The material parameters that constitute this transformation are shown in Fig. 6.5, which we realise up to the values R_{in} and R_{out}.

6.3.2 Results

The solutions of this derivative structure can be calculated numerically. In Fig. 6.6 we plot the solutions of this cavity, where we have chosen the perturbations $\Delta R_1 = 0.05R_1$ and $\Delta R_2 = 0.01R_1$. The results are similar to those of the perfect cavity with a little perturbation at the outer boundary R_2, shown in Fig. 6.4, There is, however, a major difference at low k_0, where we notice the existance of one eigenmode. The actual value of the eigenfrequency is a function of several parameters: ΔR_1, ΔR_2 and m. Oddly enough, the real part of this eigenfrequency decreases with increasing angular mode number m. This is exactly oposite to what happens in a traditional microcavity. This effect is summarised in Table 6.1. The dependency on ΔR_1 and ΔR_2 is shown in Table 6.2: the real part of the eigenfrequency $\text{Re}(k_0)$ decreases with growing ΔR_1 and increases as ΔR_2 becomes bigger. The highest Q-factors appear with the smallest $\text{Re}(k_0)$. The perturbation ΔR_2 is the most important factor on the position of k_0.
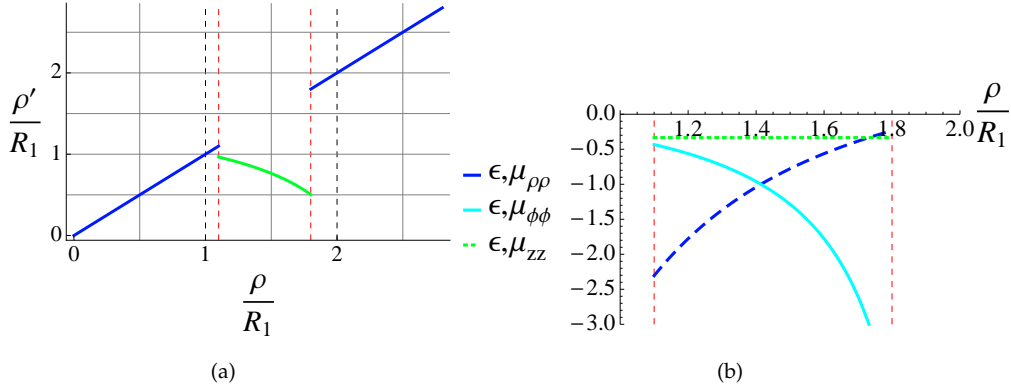
Figure 6.5: The derived design of a perfect cavity, where we have removed a little rim at both boundaries. (a) We plot the transformation from Eq. (6.20). The original boundaries R_1, R_2 correspond with the black dashed lines. The actual boundaries R_{in}, R_{out} are shown in red. At the inner boundary, we remove a rim of thickness $\Delta R_1 = 0.1 R_1$, at the outer boundary we apply $\Delta R_2 = 0.2 R_1$. The material parameters that implement this transformation are shown on figure (b). Due to the perturbation ΔR_2, the components stay bounded between two finite, negative values.

These previous results give us some feeling on how we have to design this cavity. Let us try to confine a mode with angular mode number $m = 5$ at $\text{Re}(k_0)R_1 \approx 10^{-1}$. Such a mode is deep subwavelength since $R_1/\lambda_0 \approx 10^{-1}/(2\pi) \approx 1.5 \cdot 10^{-2}$, implying that the cavity is approximately 60 times smaller than the wavelength. We would like to relax the material parameters and search for solutions with a large ΔR_2. Such a solution can be found with $\Delta R_1 = 2 \cdot 10^{-1} R_1$ and $\Delta R_2 = 2 \cdot 10^{-2} R_1$, having an eigenfrequency at $k_0 R_1 = 1.05104 \cdot 10^{-1} - 7.88149 \cdot 10^{-12}$ i. Fig. 6.7 plots the cross-section and two-dimensional field distribution of the eigenmode corresponding to this eigenfrequency. The mode has an equivalent shape as the modes inside the perfect cavity, with a maximum at the inner boundary. At the outer boundary, however, we notice a difference: instead of becoming zero, the field has a steep increment that matches with a little outgoing Hankel function. If we make ΔR_2 even smaller, the height of this steep edge decreases and can become arbitrarily small.

The results obtained in these simulations have been verified using a numerical simulation program. These comparisons are summarised in Appendix B.

6.3.3 Alternatives

To gain a better understanding in the underlying physical mechanism of the subwavelength confinement, we have searched for alternative designs that show the same functionality. The results from Sec. 6.3.2 seem to indicate that the subwavelength confinement is provided when there is a significant mismatch in combination with an outer boundary that is mapped almost on the origin. This reasoning is confirmed when we investigate an alternative design, where we have perturbed the perfect cavity by replacing a region $[R_{aux1}, R_{aux2}]$ by vacuum. The
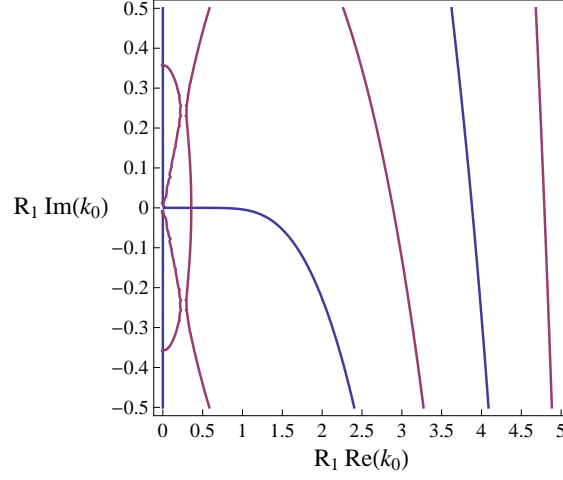
Figure 6.6: Contour plot showing a unique solution inside the derived design, where we have chosen $R_1 = 1$, $R_2 = 2$, $\Delta R_1 = 10^{-1}R_1$ and $\Delta R_2 = 5 \cdot 10^{-2}R_1$ with an angular mode number $m = 5$. At large k_0 these contours resemble those from Fig. 6.4. We do, however, notice a single solution at $k_0 = 3.56503 \cdot 10^{-1} - 3.93021 \cdot 10^{-7}$ i.

m	$\mathrm{Re}(k_0)R_1$	$\mathrm{Im}(k_0)R_1$
2	$5.78228 \cdot 10^{-1}$	$-9.40724 \cdot 10^{-2}$
3	$3.3351 \cdot 10^{-1}$	$-1.31805 \cdot 10^{-3}$
4	$1.56127 \cdot 10^{-1}$	$-1.41194 \cdot 10^{-7}$
5	$6.69607 \cdot 10^{-2}$	$-1.41926 \cdot 10^{-13}$
6	$2.74633 \cdot 10^{-2}$	$-4.15791 \cdot 10^{-13}$

Table 6.1: The dependency of the unique solution inside the derived design, defined by Eq. (6.20). These solutions were calculated with $\Delta R_1 = 0.02R_1$ and $\Delta R_2 = 0.01R_1$. As we increase m, the solution is shifted towards lower frequencies with higher Q.

correponding transfromation function is shown in Fig. 6.8. The modes of this design are solution of a set of eight equations (two at each boundary) in eight variables ($A \ldots H$). The design has three degrees of freedom: R_{aux1}, R_{aux2}, ΔR_2, which makes a general description of its eigenmodes even more complicated. In general terms, however, the same ideas apply to this design: the value of the eigenfrequency depends in the same fashion on the perturbation at the outer boundary ΔR and on the discontinuities in the transformation function. When we choose, e.g. $R_{\mathrm{aux1}} = 1.3R_1$, $R_{\mathrm{aux2}} = 1.6R_1$ and $\Delta R = 5 \cdot 10^{-2}R_1$, then we find a subwavelength solution at $k_0R_1 = 4.978 \cdot 10^{-1} - 7.360 \cdot 10^{-6}$ i. This mode is shown in Fig. 6.9. From this figure we notice also that the major part of the field is situated at the boundary R_{aux2} and that the field in the region $[R_{\mathrm{aux2}}, R_{\mathrm{out}}]$ has the same evolution as in the previous design. This makes us suspect that R_{aux2} is of crucial importance in the confining mechanism. This idea is confirmed when we try to map the parameters of this alternative design on the previous design. When we take this previous

$\Delta R_1/R_1$	$\mathrm{Re}(k_0)R_1$	$\mathrm{Im}(k_0)R_1$	$\Delta R_2/R_1$	$\mathrm{Re}(k_0)R_1$	$\mathrm{Im}(k_0)R_1$
$5\cdot10^{-3}$	$1.55203\cdot10^{0}$	$-4.48093\cdot10^{-2}$	$5\cdot10^{-3}$	$2.00719\cdot10^{-2}$	$-2.83112\cdot10^{-18}$
$1\cdot10^{-2}$	$1.34044\cdot10^{0}$	$-1.75312\cdot10^{-2}$	$1\cdot10^{-2}$	$4.77431\cdot10^{-2}$	$-6.76716\cdot10^{-15}$
$5\cdot10^{-2}$	$9.51259\cdot10^{-1}$	$-1.42216\cdot10^{-3}$	$5\cdot10^{-2}$	$3.56503\cdot10^{-1}$	$-3.93021\cdot10^{-7}$
$1\cdot10^{-1}$	$8.37764\cdot10^{-1}$	$-5.13236\cdot10^{-4}$	$1\cdot10^{-1}$	$8.37764\cdot10^{-1}$	$-5.13236\cdot10^{-4}$

Table 6.2: Two tables summarizing the effect of ΔR_1 and ΔR_2 on the solution ($m = 5$) inside the cavity. In the left table we have fixed $\Delta R_2 = 10^{-1}R_1$ and varied ΔR_1 between $5\cdot10^{-3}R_1$ and $10^{-1}R_1$. The real part of the frequency decreases as ΔR_1 increases. In the right table we varied ΔR_2 while keeping ΔR_1 fixed at 10^{-1}, where we notice that the $\mathrm{Re}(k_0)$ increases as ΔR_2 increases. The sensitivity with respect to ΔR_2 is much larger than the sensitivity with respect to ΔR_1. To achieve deep subwavelength confinement, we need a small ΔR_2.
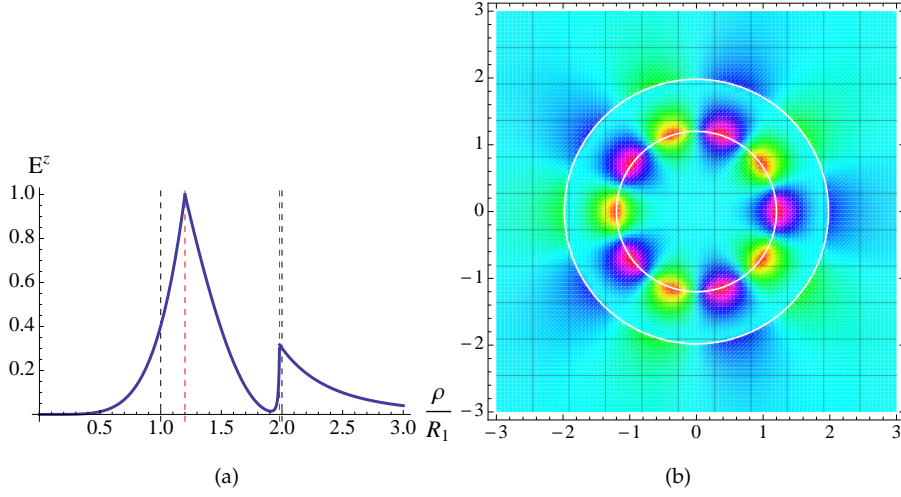

Figure 6.7: The electric field distribution inside the modified cavity, corresponding to a subwavelength solution with $m = 5$ and $k_0R_1 = 0.1$. The geometric parameters of this cavity are: $\Delta R_1 = 2\cdot10^{-1}R_1$ and $\Delta R_2 = 2\cdot10^{-2}R_1$. The eigenfrequency is situated at $k_0R_1 = 1.05104\cdot10^{-1} - 7.88149\cdot10^{-12}$ i.

design and apply $\Delta R_1 = 2.5\cdot10^{-1}R_1$ and $\Delta R_2 = 1\cdot10^{-2}R_1$, then we have an mode at $k_0R_1 = 4.41833\cdot10^{-2} - 3.36986\cdot10^{-15}$ i. Let us try to find this mode with the alternative design. Therefore we choose: $R_{\mathrm{aux2}} = R_1(1 + \Delta R_1)$, $\Delta R = \Delta R_2$ and R_{aux1} is chosen arbitrarily between R_1 and R_{aux2} at $1.25\cdot10^{-1}R_1$. With these parameters, we find a solution $k_0R_1 = 4.41833\cdot10^{-2} - 3.36986\cdot10^{-15}$ i, which fits quite well with the solution from the previous design. Furthermore we have found that the exact position of R_{aux1} is of little importance for the determination of the eigenfrequency. These ideas enable us to define different types of alternatives: any design of cavity involving a significant mismatch, followed by a transformation function which maps its outer boundary near the origin, will have subwavelength confinement within some range of its parameters. We have noticed that these parameters should be chosen such that at the boundary with a

discontinuity $f(R_{aux})$ should be smaller than R_{aux} — providing a discontinuity with a negative direction —, which means that in absolute values the $\phi\phi$-components of the material's response should be bigger than the zz-components. This also explains why R_{aux1} from the alternative design in Fig. 6.8 was of little importance: this discontinuity has a positive direction.

(a)

(b)
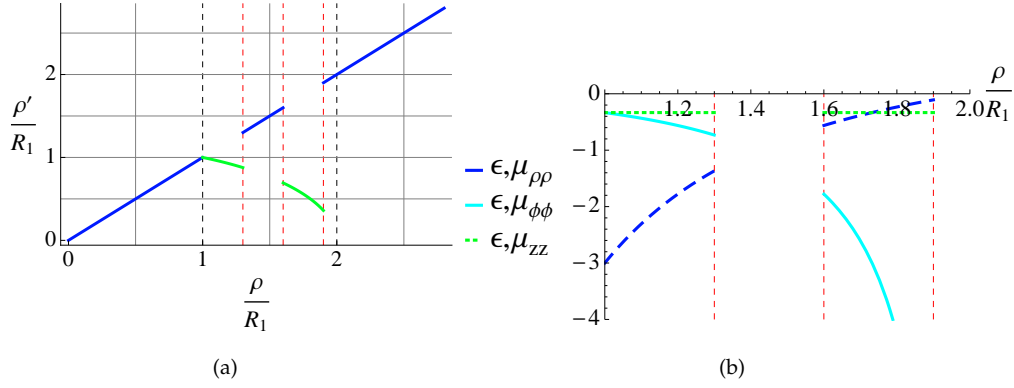
Figure 6.8: An alternative design starting from the perfect cavity: instead of perturbing the inner boundary as in Fig. 6.5, we replace an inner region $[R_{aux1}, R_{aux2}]$ by vacuum (a). The material parameters (b) are exactly the same as for a perfect cavity, except inside the above mentioned region, which we leave vacuum $\epsilon = \mu = 1$. The black dashed lines indicate the boundaries of the perfect lens R_1 and R_2, the red dashed lines correspond with R_{aux1}, R_{aux2} and $R_{out} = R_2 - \Delta R$ respectively.

(a)

(b)
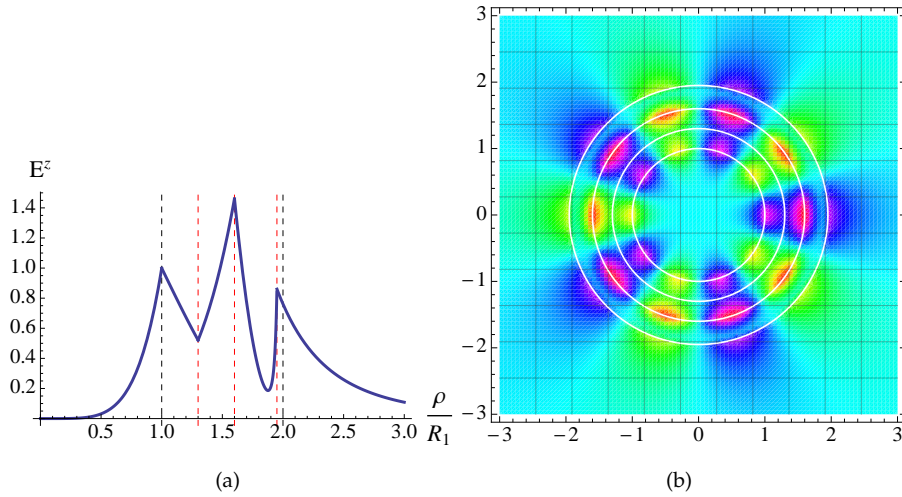
Figure 6.9: A subwavelength mode $k_0 = 4.978 \cdot 10^{-1} - 7.360 \cdot 10^{-6}\,\mathrm{i}$ inside the alternative design from Fig. 6.8, where we have chosen the parameters: $R_{aux1} = 1.3R_1$, $R_{aux2} = 1.6R_1$ and $\Delta R = 5 \cdot 10^{-2}R_1$. In the region $[R_{aux2}, R_{out}]$ we notice the same field distribution as with the modified desing in Fig. 6.7: the field decreases towards the outer boundary and has a little steep edge at the end (a). The two-dimensional density plot is shown in figure (b).

6.3.4 Discussion

We will now construct an interpretation of the confining mechanism of the first design from Fig. 6.5. The alternatives can be understood with an equivalent reasoning. We have found that the eigenfrequencies are strongly affected by a discontinuity in the transformation function. In the absence of a discontinuity, the structure (perfect cavity) is extremely singular. Furthermore, we observed a field maximum at the discontinuous boundary, which is followd by an exponential decay and a little steep edge initiating another local maximum at the outer boundary. This looks like we are dealing with two surface modes inside this structure at R_{in} and R_{out}. The interpretation then goes as follows: the left-handed dielectric between $[R_{in}, R_{out}]$ has two resonant surface modes at the boundaries with vacuum. The anisotropy inside the material, which is a consequence of the mapping $f(R_{out}) \approx 0$, reduces the energy at the outer surface mode in favor of the inner surface mode and thus enhances the confinement. In the near future, we will continue this research and try to explain these surface modes from a transformation-optical perspective.

Although we have sacrificed the continuum of modes from the perfect cavity, we have found one unique mode, which can be tuned deep subwavelength. This is not such a big sacrifice since the prescribed negative response can only be achieved at a single wavelength due to dispersion. One could try to improve the bandwith of confined modes by implementing the technique of Ref. [7], which imposes additional constraints on the material's dispersion characteristics. Another technique to broaden the bandwidth has already been mentioned and consists in using non-Euclidean geometries [8].

From the material's perspective there is still another major remark: the permittivity and permeability are *macroscopic parameters*. When they are generated using metamaterials—as these left-handed cavities require—the functional elements have to be one or more orders of magnitude smaller than these subwavelength cavities, which is a challenge nowadays in the optical range.

References

[1] Y. Luo, J. Zhang, H. Chen, S. Xi, and B. I. Wu, "Cylindrical cloak with axial permittivity/permeability spatially invariant," *App. Phys. Lett.* **93**, 033504, 2008.

[2] E. Born and M. Wolf, *Principles of Optics*, Cambidge University Press, Cambridge, 1986.

[3] W. Cai, U. K. Chettiar, A. V. Kildishev, and V. M. Shalaev, "Optical cloaking with metamaterials," *Nature Photonics* **1**, 224–227, 2007.

[4] H. Chen, X. A. Luo, H. Ma, and C. T. Chan, "The anti-cloak," *Opt. Express* **16**, 14603–14608, 2008.

[5] G. Castaldi, I. Gallina, V. Galdi, A. Alu, and N. Engheta, "The anti-cloak," *Opt. Express* **17**, 3101–3114, 2009.

[6] P. Tassin, I. Veretennicoff, and G. Van der Sande, "Veselago's lens consisting of left-handed materials with arbitrary index of refraction," *Opt. Commun.* **264**, 130–134, 2006.

[7] A. V. Kildishev, W. Cai, U. K. Chettiar, and V. M. Shalaev, "Transformation optics: approaching broadband electromagnetic cloaking," *New J. Phys.* **10**, 115029–115041, 2008.

[8] U. Leonhardt and T. Tyc, "Broadband invisibility by non-Euclidean cloaking," *Science* **323**, 110–112, 2009.

CHAPTER 7

A Frequency Tuner Using General Relativity

In this chapter, we will borrow two famous metrics from general relativity (the Schwarzschild solution and the Robertson-Walker metric) and try to mimick them inside a dielectric. Since these metrics inhibit two different kind of redshifts, we will try to implement them as frequency tuners. To achieve this purpose, we will first have to derive more general constitutive equations that relate material parameters with a general four-dimensional space-time metric. It will turn out that it is not possible to translate the gravitational redshift in a dielectric. The cosmological redshift, however, is perfectly transferable in a dielectric with isotropic an homogeneous permittivity and permeability that is evolving in time.

7.1 Introduction

In chapter 3 we wrote down Maxwell's equations in a general metric and we compared them with the macroscopic Maxwell's equations in a dielectric, expressed in a right-handed coordinate system. We thus introduced dielectrics that could perform general transfomations, which we therefore called transformation media. One might object that it was somewhat exaggerating to say that these media perform *general* transformations, since they merely implement spatial transformations. Moreover, a tensorial formulation of Maxwell's equations is only possible on the background of a four-dimensional space-time. This shortcoming will be eliminated in Sec. 7.2, where we will derive how general space-time transformations are implemented with bianisotropic materials, defined by Plebanski's constitutive equations, Eq. (3.2). Although most applications in transformation optics involve spatial transformation media, there are two intriguing examples of space-time transformation media: an optical analogue of an event horizon and an optical analogue of the Aharonov-Bohn effect [1]. Both examples, involving the study of

light propagation in a moving medium, have a fundamental theoretical importance. Hitherto, there has been little attention for space-time transformation media in practical applications.

7.2 General Space-time Transformations

It is not too difficult to extend the differential formalism from Sec. 3.2 to a four-dimensional manifold. A point on such a manifold can be expressed in a four-dimensional coordinate system, e.g., the Galilean coordinates $\{x^\mu\} = \{ct, x, y, z\}$, which are a generalisation of the Cartesian coordinates from a three-dimensional space. From special relativity, we know that the flat space-time metric in Galilean coordinates can be expressed as

$$ds^2 = -c^2 dt^2 + dx^2 + dy^2 + dz^2. \tag{7.1}$$

This metric, associated with a four-dimensional flat space-time is called the Minkowski metric.[*]

We will derive the material properties corresponding to general space-time metrics in a very similar way as in Ref. [1]. To translate Maxwell's equations in a general covariant way, we introduce the electromagnetic field strength tensor. In a right-handed Cartesian coordinate system, its components are given by:

$$F_{\mu\nu} = \begin{pmatrix} 0 & -E_x & -E_y & -E_z \\ E_x & 0 & cB_z & -cB_y \\ E_y & -cB_z & 0 & cB_x \\ E_z & cB_y & -cB_x & 0 \end{pmatrix}. \tag{7.2}$$

When we additionally define the current four-vector $j^\mu = (\rho, j^x/c, j^y/c, j^z/c)$, we can compress the four free space Maxwell's equations into two tensorial equations:

$$\frac{\partial F_{\mu\nu}}{\partial x^\lambda} + \frac{\partial F_{\nu\lambda}}{\partial x^\mu} + \frac{\partial F_{\lambda\mu}}{\partial x^\nu} = 0,$$
$$\epsilon_0 \nabla_\nu F^{\mu\nu} = j^\mu. \tag{7.3}$$

We can rewrite these equations in terms of the background metric ds^2 with components $g_{\mu\nu}$:

$$\frac{\partial F_{\mu\nu}}{\partial x^\lambda} + \frac{\partial F_{\nu\lambda}}{\partial x^\mu} + \frac{\partial F_{\lambda\mu}}{\partial x^\nu} = 0,$$
$$\epsilon_0 \frac{1}{\sqrt{-g}} \frac{\partial(\sqrt{-g} F^{\mu\nu})}{\partial x^\nu} = j^\mu. \tag{7.4}$$

The minus sign in front of the determinant of the metric g is simply the result of the fact that this determinant is negative in a four-dimensional space time with Lorentzian signature.

To express the macroscopic Maxwell's equations inside a dielectric in a tensorial way, we introduce the electromagnetic excitation tensor $G^{\mu\nu}$. Again, in a right-handed Cartesian coordinate

---

[*]We will consequently apply a Lorentzian $(-+++)$ signature, where the time coordinate has a negative contribution to the line element.

system, we express its components as:

$$G^{\mu\nu} = \begin{pmatrix} 0 & D^x & D^y & D^z \\ -D^x & 0 & H^z/c & -H^y/c \\ -D^y & -H^z/c & 0 & H^x/c \\ -D^z & H^y/c & -H^x/c & 0 \end{pmatrix}.$$

(7.5)

In terms of this tensor, we can write macroscopic Maxwell's equations inside a dielectric, in a right-handed Cartesian coordinate sytem as

$$\frac{\partial F_{\mu\nu}}{\partial x^\lambda} + \frac{\partial F_{\nu\lambda}}{\partial x^\mu} + \frac{\partial F_{\lambda\mu}}{\partial x^\nu} = 0,$$

$$\frac{\partial G^{\mu\nu}}{\partial x^\nu} = J^\mu.$$

(7.6)

We can now identify both sets—free space with general metric in Eq. (7.4) and dielectric in right handed Cartesian coordinates in Eq. (7.6)—when we impose

$$J^\mu = \sqrt{-g} j^\mu$$

(7.7)

$$G^{\mu\nu} = \epsilon_0 \sqrt{-g} F^{\mu\nu}$$

(7.8)

This first equation (7.7) looks familiar and is completely equivalent with what we have derived in Eq. (3.69). The second equation (7.8) associates the metric with the constitutive equations of the material. We will clarify this relation in the next steps. Using the property of the metric to raise and lower indices, according to Eqs. (3.26)-(3.27), we can rewrite Eq. (7.8) as

$$F_{\mu\nu} = \frac{1}{\epsilon_0 \sqrt{-g}} g_{\mu\lambda} g_{\nu\rho} G^{\lambda\rho}.$$

(7.9)

We can now express the $(0\ i)$-components[*] of this equation in terms of the usual vector fields, yielding:

$$E_i = \frac{1}{\epsilon_0 \sqrt{-g}} (g_{0j} g_{i0} - g_{00} g_{ij}) D^j - \frac{1}{\epsilon_0 \sqrt{-g}} g_{0k} g_{ij} \frac{1}{c} \epsilon^{kjl} H_l.$$

(7.10)

We rearrange this formula to express **D** as a function of **E** and **H** and raise the index i with g^{mi}:

$$g^{mi}(g_{0j} g_{i0} - g_{00} g_{ij}) D^j = g^{mi} \epsilon_0 \sqrt{-g} E_i + g^{mi} g_{ij} \frac{g_{0k}}{c} \epsilon^{kjl} H_l.$$

(7.11)

To simplify the expression in front of D^j, we indicate two identities

$$g^{mi} g_{i0} = -g_{00} g^{m0},$$

(7.12)

$$g^{mi} g_{ij} = \delta_j^m - g^{m0} g_{j0},$$

(7.13)

which immediately follow from $g_{\mu\lambda} g^{\lambda\nu} = \delta_\mu^\nu$ and $g_{j\lambda} g^{\lambda m} = \delta_j^m$. When we insert these equations in Eq. (7.11), we finally arrive with

$$D^m = \epsilon_0 \frac{\sqrt{-g} g^{mi}}{-g_{00}} E_i + \epsilon^{mkl} \frac{g_{0k}}{c g_{00}} H_l.$$

(7.14)

---

[*]We recall the convention that Greek indices run from 0 to 3: (t, x, y, z), while the Latin indices cover only the spatial dimensions 1 to 3: (x, y, z).

The same line of reasoning can be repeated in terms of the dual tensors ${}^*F^{\mu\nu} = \frac{1}{2}\epsilon^{\mu\nu\lambda\rho}F_{\lambda\rho}$ and ${}^*G_{\mu\nu} = \frac{1}{2}\epsilon\mu\nu\lambda\rho G^{\lambda\rho}$, yielding:

$$B^m = \mu_0 \frac{\sqrt{-g}g^{mi}}{-g_{00}}H_i - \epsilon^{mkl}\frac{g_{0k}}{cg_{00}}E_l. \tag{7.15}$$

When we identify these equations (7.14)-(7.15) with Plebanski's constitutive equations, as given in Eq. (3.2), we find that a general space-time metric $g_{\mu\nu}$ can be implemented in physical space with a bianisotropic dielectric whose material properties are given by

$$\epsilon^{ij} = \epsilon_0 \frac{\sqrt{-g}g^{ij}}{-g_{00}} \tag{7.16}$$

$$\omega_i = \frac{g_{0i}}{g_{00}} \tag{7.17}$$

In a completely analogous way as in Sec. 3.3.2, one can now deduce the material's implementation when we assume a nontrivial metric γ_{ij}, e.g., spherical coordinates, in the physical space:

$$\epsilon^{ij} = \epsilon_0 \frac{\sqrt{-g}g^{ij}}{\sqrt{\gamma}(-g_{00})} \tag{7.18}$$

$$\omega_i = \frac{g_{0i}}{g_{00}} \tag{7.19}$$

We notice that these relations include the spatial transformations from Eq. (3.60) when we insert the Minskowskian metric: $g_{00} = -1$ and $g_{0i} = 0$.

7.3 Gravitational Redshift

7.3.1 The Schwarzschild Solution

In general relativity, the Einstein field equations describe how space is altered due to the presence of energy and momentum [2]. One of the most famous solutions of these equations is *the Schwarzschild solution*, which is the unique vacuum solution outside a spherical symmetric object with mass M [3]. Due to the spherical symmetry, it is described most easily in spherical coordinates, yielding:

$$ds^2 = -\left(1 - \frac{R_s}{r}\right)c^2 dt^2 + \left(1 - \frac{R_s}{r}\right)^{-1} dr^2 + r^2 d\Omega^2, \tag{7.20}$$

where $d\Omega^2$ is the metric of a unit two-sphere:

$$d\Omega^2 = d\theta^2 + \sin^2\theta \, d\phi^2. \tag{7.21}$$

This metric introduces the Schwarzschild radius R_s, which is defined as

$$R_s = \frac{2GM}{c^2}, \tag{7.22}$$

with $G = 6.67 \cdot 10^{-11} \text{m}^3 \text{kg}^{-1} \text{s}^{-2}$, the gravitational constant. This solution fits extremely well the motion of planets in our solar system. One of the tests to verify the accuracy of Einstein's theory is the observation of the gravitational redshift.

Suppose that a photon is emitted at a radius r_1 (measured from the origin of the gravitating body with mass M) at a frequency ω_1. When this photon is propagating on the background of a Schwarzschild metric towards an observer at radius r_2, then it will be observed at a different frequency ω_2, which is related to the initial frequency ω_1 by

$$\frac{\omega_2}{\omega_1} = \left(\frac{1 - R_s/r_1}{1 - R_s/r_2} \right)^{1/2} . \tag{7.23}$$

This shows us that the observed frequency will be shifted to lower values if the photon travels away from the gravitating body ($r_2 > r_1$). Lower freqencies correspond with longer (redder) wavelengths, which is why we call this a redshift. Photons that are traveling towards the gravitating body are blueshifted, corresponding with the higher frequencies. The frequency shift is actually an expression of the conservation of energy. The photon's energy is a constant along its trajectory. Its total energy is, however, the sum of the kinetic energy, which is proportional to the frequency, with the potential energy, which depends on the metric background. It is then clear that when a photon climbs out a gravitational potential, it will hand in some kinetic energy, shifting down in frequency. In the opposite direction the inverse reasoning applies. This frequency conversion is not own to the Schwarzschild solution: any metric encoding a gravitational potential will inhibit such a gravitational redshift.

7.3.2 Material Implementation

Let us now try to design a material that implements this Schwarzschild metric. Therefore, we apply Eqs. (7.18)-(7.19), where γ_{ij} is given by Eq. (3.39), yielding:

$$\epsilon^r_{\ r} = \mu^r_{\ r} = 1,$$

$$\epsilon^\theta_{\ \theta} = \mu^\theta_{\ \theta} = \frac{1}{1 - \frac{R_s}{r}}, \tag{7.24}$$

$$\epsilon^\phi_{\ \phi} = \mu^\phi_{\ \phi} = \frac{1}{1 - \frac{R_s}{r}}. \tag{7.25}$$

These parameters are plotted in Fig. 7.1. The response in the radial direction stays constant (ϵ_0) over the entire space. The angular responses grow to infinity at R_s. This radius corresponds with the event horizon of a black hole. At the singularity $r = 0$, we notice that the angular responses becomes zero.

7.3.3 Discussion

Firstly, we observe that at infinity the material equals vacuum, which is in correspondance with the fact that the Schwarzschild solutions is assymptotically flat (Minkowskian) at infinity.
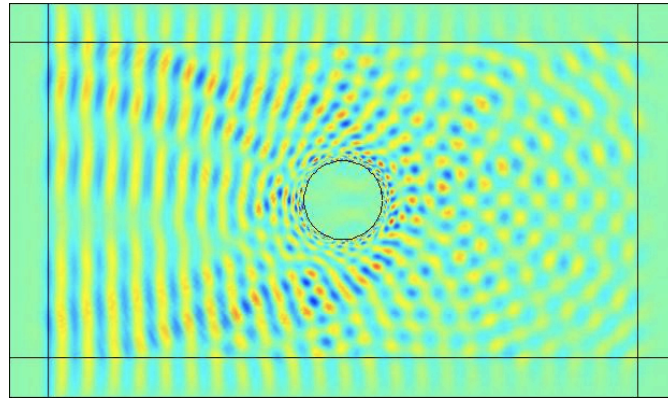
When we simulate the propagation of electromagnetic waves through a component with constitutive equations from Eq. (7.24), we get the density plot from Fig. 7.2. We notice here how
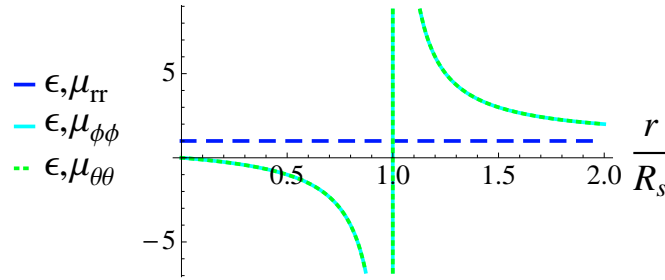
Figure 7.1: Material parameters that implement the Schwarzschild metric. We notice that the angular responses tend to infinity at the event horizon ($r = R_s-$, passed which they become negative. At the singularity ($r = R_s$) these parameters become zero.

the wavefront is bent around the material, which could be an analogy of the effect of photon deflection around massive objects.

Figure 7.2: A numerical simulation of the propagation of electromagnetic field through the structure with material parameters from Eq. (7.24). Inside the event horizon $r = R_s$ (indicated by the inner circle), we have put an absorbing material.

We should be careful to identify other similarities. This component is built from an anisotropic (linear) dielectric, so we do not encounter the gravitational redshift, which occurs in gravitational reality. This should be no surprise, because we have not encoded the g_{00}-component that alters the proper time of a stationary observer. It is thus not possible to translate the gravitational redshift with a dielectric, since we will observe it from an Minkowskian metric which has $g_{00} = -1$.

7.4 Frequency Shifter Based on a FRW-Metric

7.4.1 Robertson-Walker Metric

To study the evolution and structure of the universe in its totality, we appeal to the cosmological models. One of these models is the Robertson-Walker metric, in which we postulate that the universe is spatially homogeneous and isotropic but can be evolving in time [3]. In its most general appearance, this solution is given by

$$ds^2 = -c^2 dt^2 + a^2(t)\left[\frac{dr}{1 - \kappa r^2} + r^2 \, d\Omega^2\right]. \tag{7.26}$$

The dimensionless scale factor $a(t)$ encodes the evolution of this universe and is related to the famous Hubble parameter $H = \dot{a}/a$, where $\dot{a}$ refers to the derivative with respect to time. The curvature parameter κ is a measure of the spatial curvature. It can take on any value $\in \mathbb{R}$: a negative value is refered to as an *open* universe, a positive value is called *closed*, and $\kappa = 0$ is *flat*.

Such a nonstationary solution with $a(t) \neq$ constant has an interesting influence on the propagation of electromagnetic radiation. A photon emitted at a frequency ω_{em} at the instance t_{em} will be measured at a different frequency ω_{obs} at the time t_{obs}. The relation between these to frequencies is given by:

$$\frac{\omega_{obs}}{\omega_{em}} = \frac{a(t_{em})}{a(t_{obs})}. \tag{7.27}$$

In the case of an expanding universe $a(t_{obs})$ will be bigger then $a(t_{em})$ and so the observed frequency will be lower—redshifted—than the emitted frequency. This effect has been labeled with the name *cosmological redshift*. The origin of the redshift lies the fact that a particle slows down with respect to a comoving observer in an expanding universe. This shift is used by astronomers to calculate the distance of stars, since it gives us a measure of time that has elapsed since the photon was emitted.

7.4.2 Material implementation

The Robertson-Walker metric Eq. (7.26) has its g_{00}-component equal to one, which is the same as our Minkowskian reference frame. This gives us good hopes to implement a structure in which we can observe an analogy of the cosmological redshift. This shift also occurs in the spatially flat implementation metric ($\kappa = 0$) and so we will restrict ourselves to this case. In Galilean coordinates, this metric can be written as:

$$ds^2 = -c^2 dt^2 + a^2(t)\left[dx + dy^2 + dz^2\right]. \tag{7.28}$$

Let us now implement this metric with a dielectric using Eqs. (7.18)-(7.19). Once again, we have notice that this structure can be made without bianisotropy ($\mathbf{w} = 0$). The permittivity and

permeability have to meet

$$\epsilon^x_{\ x} = \mu^x_{\ x} = a(t),$$
$$\epsilon^y_{\ y} = \mu^y_{\ y} = a(t), \tag{7.29}$$
$$\epsilon^z_{\ z} = \mu^z_{\ z} = a(t). \tag{7.30}$$

The Robertson-Walker metric without spatial curvature can thus be translated into a isotropic, homogeneous dielectric whose permittivity and permeability equal the scale factor $a(t)$ at all times.

The solutions inside such a component are found by solving Maxwell's equations in the absence of free sources and currents:

$$\nabla \times \mathbf{E} = -\frac{\partial \mathbf{B}}{\partial t}, \tag{7.31}$$

$$\nabla \times \mathbf{H} = \frac{\partial \mathbf{D}}{\partial t}, \tag{7.32}$$

in combination with these constitutive equations:

$$\mathbf{D} = \epsilon_0\, a(t)\, \mathbf{E}, \tag{7.33}$$

$$\mathbf{B} = \mu_0\, a(t)\, \mathbf{H}. \tag{7.34}$$

When we take the curl of Eq. (7.33) and apply Eqs. (7.33)-(7.34), we derive that $\mathbf{E}(\mathbf{r}, t)$ is the solution of

$$\nabla \times (\nabla \times \mathbf{E}) = -\mu_0\epsilon_0 \frac{\partial}{\partial t}\left(a(t)\frac{\partial}{\partial t}(a(t)\mathbf{E})\right). \tag{7.35}$$

By introducing the variable η, defined by

$$\mathrm{d}\eta = \frac{\mathrm{d}t}{a(t)}, \tag{7.36}$$

we can rewrite this equation to the more acquainted form

$$\Delta \mathbf{E} - \mu_0\epsilon_0 \frac{\partial^2 \mathbf{E}}{\partial \eta^2} = 0, \tag{7.37}$$

from which we know the solutions can be written as a sum of plane waves in the variables $(\mathbf{r}, \eta)$ and when we reinsert Eq. (7.36), we find the solutions in terms of $\mathbf{r}$ and t:

$$\mathbf{E}(\mathbf{r}, t) = \sum_\omega A(\omega)\, e^{i(\mathbf{k}\cdot\mathbf{r} - \omega \int \frac{\mathrm{d}t}{a(t)})}, \tag{7.38}$$

where $|\mathbf{k}| = \omega/c$. One term out of this sum is shown in Fig. 7.3.

Let us now have a look if we can retrieve the redshift. The instantaneous frequency ω_{inst} is defined as the partial derivative of the phase with respect to the time-coordinate with a minus sign [4]. Applied to a single solution inside the component, this becomes

$$\omega_{\text{inst}}(t) = -\frac{\partial(\mathbf{k}\cdot\mathbf{r} - \omega \int \frac{\mathrm{d}t}{a(t)})}{\partial t} = \frac{\omega}{a(t)}. \tag{7.39}$$
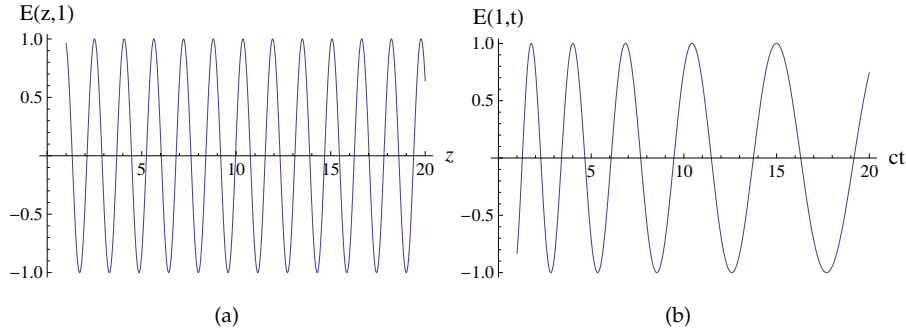
Figure 7.3: A graphical representation of one solution of the wave equation inside the material. (a) The spatial variation at a constant time $t = 1$. (b) The temporal variation of this solution for fixed $r = 1$, when we modulate the permittivity and permeability with
$$a(t) = 1 + 3/20\,t.$$

At two different times t_1 and t_2, the instantaneous frequencies are thus related by

$$\frac{\omega_{\text{inst}}(t_2)}{\omega_{\text{ins}}(t_1)} = \frac{a(t_1)}{a(t_2)},\tag{7.40}$$

which perfectly agrees with Eq. (7.27).

7.4.3 A Frequency Shifting Device

Inside the material, an individual solution is subject to an equivalent of the cosmological redshift. We could now wonder if such a device with a finite extend, would suit as a frequency converter. Therefore, consider the setup as shown in Fig. 7.4, where we introduced the function

$$f(t) = \int \frac{\mathrm{d}t}{a(t)},\tag{7.41}$$

and where we has imposed that $z = 0$ coincides with the left boundary of the component to clarify the equations to come. We illuminate the dielectric from the left in region (I) with a monochromatic plane wave at frequency ω_0 and we want to calculate the wave that will be emitted in region (III).

Inside the component we will generate a sum of solutions of the wave equation to match the wave at the left boundary ($z = 0$):

$$A_0 \mathrm{e}^{-\mathrm{i}\omega_0 t} = \int_{-\infty}^{\infty} A(\omega)\,\mathrm{e}^{-\mathrm{i}\omega f(t)}\mathrm{d}\omega.\tag{7.42}$$
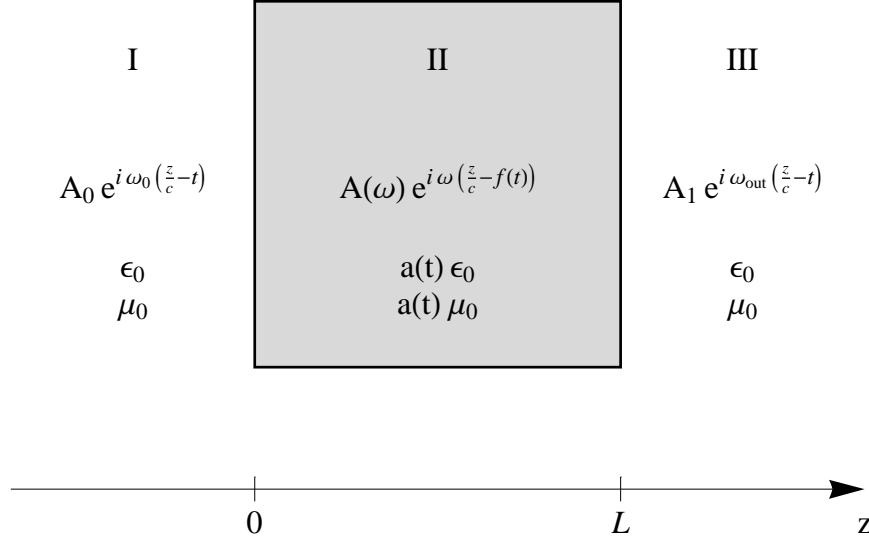
It can be shown that the other electromagnetic boundary condition, implying the continuity of the tangential component of the magnetic field, is automatically fulfilled due to the impedance-matching. The coefficients $A(\omega)$ are found by multiplying both sides of this equation with

$f'(t)\mathrm{e}^{\mathrm{i}\omega'f(t)}$ and integrate over the time coordinate. This yields:

$$\int_{-\infty}^{+\infty} A_0\mathrm{e}^{-\mathrm{i}\omega_0 t}f'(t)\mathrm{e}^{\mathrm{i}\omega'f(t)}\mathrm{d}t = \int_{-\infty}^{\infty}\int_{-\infty}^{\infty} A(\omega)\,\mathrm{e}^{-\mathrm{i}\omega f(t)}f'(t)\mathrm{e}^{\mathrm{i}\omega'f(t)}\mathrm{d}\omega\,\mathrm{d}t, \tag{7.43}$$

$$= \int_{-\infty}^{\infty} A(\omega)\int_{-\infty}^{\infty}\mathrm{e}^{\mathrm{i}(\omega'-\omega)f(t)}\mathrm{d}f\,\mathrm{d}\omega, \tag{7.44}$$

$$= 2\pi\,A(\omega'). \tag{7.45}$$

I	II	III
$A_0\,\mathrm{e}^{i\,\omega_0\left(\frac{z}{c}-t\right)}$	$A(\omega)\,\mathrm{e}^{i\,\omega\left(\frac{z}{c}-f(t)\right)}$	$A_1\,\mathrm{e}^{i\,\omega_{\mathrm{out}}\left(\frac{z}{c}-t\right)}$
ϵ_0	$a(t)\,\epsilon_0$	ϵ_0
μ_0	$a(t)\,\mu_0$	μ_0

Figure 7.4: A setup where we implement the a finit Robertson-Walker device. At the left a monochromatic wave at ω_0 impinges on the device. We modulate the permittivity and permeability as $a(t) = 1 + t$. This results in a frequency shift in region (III), which is given by $\frac{\omega_{out}}{\omega_0} = \frac{a(t_1)}{a(t_2)}$

At the right boundary a wave will be emitted that is given by:

$$\mathbf{E}_{\mathrm{II}}(L,t) = \int_{-\infty}^{\infty} A(\omega)\,\mathrm{e}^{\mathrm{i}\omega(L/c-f(t))}\mathrm{d}\omega. \tag{7.46}$$

When we insert Eq. (7.45) in this equation, we can rewrite the output as

$$\mathbf{E}_{\mathrm{II}}(L,t) = \frac{A_0}{2\pi}\int_{-\infty}^{\infty}\int_{-\infty}^{+\infty}\mathrm{e}^{-\mathrm{i}\omega_0 t'}f'(t')\mathrm{e}^{\mathrm{i}\omega f(t')}\mathrm{d}t'\,\mathrm{e}^{\mathrm{i}\omega(L/c-f(t))}\mathrm{d}\omega, \tag{7.47}$$

and when we change the order of integration, this becomes

$$\mathbf{E}_{\mathrm{II}}(L,t) = A_0\int_{-\infty}^{+\infty}\delta\left(f(t') + L/c - f(t)\right)\mathrm{e}^{-\mathrm{i}\omega_0 t'}\mathrm{d}t'. \tag{7.48}$$

The dirac delta function ones again cancels the integral and when we introduce the inverse function f^{-1}, we finally arrive at

$$\mathbf{E}_{\mathrm{II}}(L,t) = A_0\mathrm{e}^{-\mathrm{i}\omega_0 f^{-1}(f(t)-L/c)}. \tag{7.49}$$

In region (III) after the device will thus propagate a wave with an electric field that is given by

$$\mathbf{E}_{\text{III}}(z, t) = A_0 e^{i\omega_{\text{out}}(z/c - t)}, \tag{7.50}$$

with an angular frequency

$$\omega_{\text{out}} = \frac{\partial \left(\omega_0 f^{-1}(f(t) - L/c) \right)}{\partial t}, \tag{7.51}$$

$$= \omega_0 \frac{f'(t)}{f' \left(f^{-1} \left(f(t) - L/c \right) \right)}. \tag{7.52}$$

This equation shows indeed that the proposed design from Fig. 7.4 executes a frequency shift. Since the velocity of the wavefronts $v = c/a(t)$, we know that $L = \int_{t_1}^{t_2} c/a(t) \, \mathrm{d}t = c \left(f(t_2) - f(t_1) \right)$, where t_1 and t_2 indicate the time of incidence and departure of a wavefront. If we are looking at a time t to right boundary, then $f^{-1} \left(f(t) - L/c \right)$ corresponds to the time when the wavefront was at the left boundary.

$$\frac{\omega_{\text{out}}}{\omega_0} = \frac{f'(t_2)}{f'(t_1)}, \tag{7.53}$$

$$= \frac{a(t_1)}{a(t_2)}. \tag{7.54}$$

which brings us full circle at the cosmological redshift formula.

7.4.4 Discussion

Firstly, we observe that the Robertson-Walker solution is implemented with an anisotropic, homogeneous material, which is evolving in time. This corresponds exactly to the postulates by which we constructed the Robertson-Walker metric: a spatially isotropic and homogeneous and nonstationary universe.

Secondly, it is worth mentioning that the permittivity and permeability should vary homogenously. The underlying physical effect should thus not be confused with high-frequent electrical modulation. Also here the number of variable material parameters can be reduced with a factor two when considering a single polarisation.

We also want to point out that the modulation should be very high to achieve significant frequency tuning. This problem could be resolved by temporally capturing the wave inside the components with reflecting facets.

Finally, we want to mention that in the case of a redshift—where the wave has gained energy through the material—the energy balance can be restored when considering the energy that is needed to modulate the constitutive parameters. A blue-shifted setup seems more appealing since this might return energy to the material. The possible applications will be further investigated in the near future.

References

[1] U. Leonhardt and T. G. Philbin, "General relativity in electrical engineering," *New J. Phys.* **8**, 1777–1780, 2006.

[2] A. Einstein, "Die grundlage der allgemeinen relativitatstheorie," *Ann. der. Phys.* **49**, 769–822, 1916.

[3] S. Carroll, *Spacetime and Geometry*, Addison Wesley, New York, 2003.

[4] B. Boashash, "Estimating and interpreting the instantaneous frequency of a signal. i. fundamentals," *Proc. IEEE* **80**, 520–538, 1992.

CHAPTER 8

Conclusions and Outlook

Transformation optics introduces the concept of an electromagnetic space that can differ significantly from the physical space that we perceive. This offers us a new approach to study the interaction between light and matter. The elegance of this approach is the intrinsic independency on parameters of the light under consideration, such as the polarisation or frequency.

The example of an invisibility cloak clearly pointed out how transformation media are capable of deceiving the light by changing the boundary conditions in the electromagnetic space. In chapter 2, our analysis of traditional microcavities demonstrated the importance of boundary conditions in the determination of its modes. The combination of these two facts suggests the possibility of designing performant cavities within the framework of transformation optics. Moreover, the frequency independency of this technique provides the possibility of subwavelength cavities.

In this work, we have proposed different designs for optical cavities. One of these designs—that we have named *the perfect cavity*—confirms the previous considerations. This cavity confines every frequency, even the subwavelength ones, for an infinite time. In practice, however, the slightest perturbation in the material parameters would alter the boundary conditions and eliminate the continuous set of modes.

To solve this problem, we have derived another design from the perfect cavity, which is based on a discontinuous transformation between the physical and the electromagnetic spaces. The resulting cavity still has deep subwavelength modes, which are less sensitive to perturbations. Considering the mode profiles and the sensitivity of these modes regarding deviations on the material parameters, we assume that these modes are surface modes.

Nevertheless, there are still some remaining questions related to our transformation-optical cavities. As left-handed materials tend to have significant absorption, we will have to include this parameter in future simulations. Furthermore, it will be interesting to explain these deep subwavelength modes from the perspective of plasmonics. This will give an indication of how to generalise the component in three dimensions, making a spherical cavity. We will also try to implement the innovative idea of broadband, non-Euclidean cloaking recently proposed by

Ulf Leonhardt in order to raise the bandwidth or relax the material constraints of these cavities. Finally, although our current work was focused on transformations of the radial coordinate, more involved transformations including other coordinates may be useful.

We also explored the potential of space-time transformation optics, in which space-time metrics from general relativity can be implemented with dielectrics. On the background of such a metric—the Robertson-Walker solution that describes the structure of the universe—a photon experiences a cosmological redshift. We successfully translated this effect generating a compact frequency shifting device that is able to alter the frequency of an electromagnetic wave using a time-dependent index of refraction.

In the near future, we will generalise the setup by taking into account the energy that is needed to modulate the refractive index. Such an energy balance will especially be interesting in the case of an electromagnetic blueshift, where the outgoing light has lost energy inside the material, which could potentially be used as an energy converter. Likewise, we will need to define a way to modulate the permeability together with the permittivity, and analyse the possibility of direct applications such as frequency modulation for telecommunications or frequency conversion for laser applications. It would be nice, of course, if we could use this frequency-shifting device as an optical cavity, e.g., by choosing a clever modulation of the refractive index.

It is, however, very difficult to make future perspectives within this rapidly evolving field of transformation optics, due to the innovating work of many researchers through which we gain, every day, a better understanding in the relativity of electromagnetic reality.

APPENDIX A

Spherical Cavity

In this Appendix, we give the calculations of the perfect cavity in the spherical case. Although these calculations are somewhat more cumbersome than in the cylindrical case, the underlying idea is exactly the same. First, we will discuss the setup of such a cavity. Then, we will calculate the spherical solutions inside the cloaking region. In the last step, we will match the solutions of the different regions and demonstrate that there is no constraint on the confined frequency.

A.1 Setup

As is the case with the well-known invisibility cloaks, the structure under consideration is actually a spherical shell. Between the inner radius R_1 and the outer radius R_2 of the shell, we implement a dielectric structure whose ϵ and μ tensor become a function of space. These variations can be designed using the theory of transformation optics. Working in a spherical coordinate system (r, θ, ϕ), we assume the field to be TE, also called magnetic multipole fields. We suggest a transformation, defined by:

$$r' = f(r), \tag{A.1}$$

$$\theta' = \theta, \tag{A.2}$$

$$\phi' = \phi. \tag{A.3}$$

The function $f(r)$ has to meet the constraints

$$f(R_1) = R_1, \tag{A.4}$$

$$f(R_2) = 0. \tag{A.5}$$

Eq. (A.4) ensures the continuity of electromagnetic space and as a result the shell will be impedance-matched at the inner boundary. The confinement of the waves is ensured by

Eq. (A.5). The boundary at which $f(r) = 0$ imposes a natural boundary for the electromagnetic waves. These conditions, however, do not define $f(r)$ in an unambiguous way. Let us consider a linear function. By imposing A.4 and A.5, we find

$$f(r) = \frac{R_1}{R_1 - R_2}(r - R_2). \tag{A.6}$$

The material parameters that implement this transformation are given by

$$\epsilon^r_{\ r} = \mu^r_{\ r} = \frac{f^2(r)}{r^2 f'(r)} = \frac{R_1}{R_1 - R_2} \frac{(r - R_2)^2}{r^2}, \tag{A.7}$$

$$\epsilon^\theta_{\ \theta} = \mu^\theta_{\ \theta} = f'(r) = \frac{R_1}{R_1 - R_2}, \tag{A.8}$$

$$\epsilon^\phi_{\ \phi} = \mu^\phi_{\ \phi} = f'(r) = \frac{R_1}{R_1 - R_2}. \tag{A.9}$$

These components are all negative ($R_1 < R_2$), which means that the structure will be made using left-handed materials. We also notice that these components stay bounded to finite values, as opposed to the cylindrical perfect cavity.

A.2 Solutions Inside a Spherical Cloak

To find out which fields propagate inside the cloaking shell, we first derive the wave equation for the waves inside the cloak. We start with Maxwell's equations:

$$\mathbf{\nabla} \times \mathbf{E} = -\frac{\partial \mathbf{B}}{\partial t}, \qquad\qquad \mathbf{\nabla} \times \mathbf{E_0} = i\omega \mathbf{B_0}, \tag{A.10}$$

$$\mathbf{\nabla} \times \mathbf{H} = \frac{\partial \mathbf{D}}{\partial t}, \qquad\qquad \mathbf{\nabla} \times \mathbf{H_0} = -i\omega \mathbf{D_0}, \tag{A.11}$$

where we used the convention $\mathbf{E} = \mathbf{E_0} e^{-i\omega t}$. Assuming $\mathbf{E_0} = E^\theta \mathbf{1}_\theta + E^\phi \mathbf{1}_\phi$, we can calculate the magnetic field using Eq. (A.10) in combination with $B^i = \mu_0 \mu^i_{\ j} H^j$:

$$H^r = \frac{B^r}{\mu_0 \mu^r_{\ r}} = \frac{1}{\mu_0 \mu^r_{\ r}} \frac{1}{i\omega} \frac{1}{r \sin \theta} \left(\frac{\partial}{\partial \theta}(\sin \theta E^\phi) - \frac{\partial E^\theta}{\partial \phi} \right),$$

$$H^\theta = \frac{B^\theta}{\mu_0 \mu^\theta_{\ \theta}} = -\frac{1}{\mu_0 \mu^\theta_{\ \theta}} \frac{1}{i\omega} \frac{1}{r} \frac{\partial}{\partial r}(rE^\phi), \tag{A.12}$$

$$H^\phi = \frac{B^\phi}{\mu_0 \mu^\phi_{\ \phi}} = \frac{1}{\mu_0 \mu^\phi_{\ \phi}} \frac{1}{i\omega} \frac{1}{r} \frac{\partial}{\partial r}(rE^\theta).$$

These components can now be reintegrated in Eq. (A.11). In the θ-direction, we obtain

$$\frac{1}{r \sin \theta} \frac{\partial}{\partial \phi} \left[\frac{1}{\mu_0 \mu^r_{\ r}} \frac{1}{i\omega} \frac{1}{r \sin \theta} \left(\frac{\partial}{\partial \theta}(\sin \theta E^\phi) - \frac{\partial E^\theta}{\partial \phi} \right) \right] - \frac{1}{r} \frac{\partial}{\partial r} \left(r \frac{1}{\mu_0 \mu^\phi_{\ \phi}} \frac{1}{i\omega} \frac{1}{r} \frac{\partial}{\partial r}(rE^\theta) \right) = -i\omega \epsilon_0 \epsilon_\theta E^\theta. \tag{A.13}$$

Since $\mu^r{}_r$ is only a function of r, Eq. (A.7), this can be rewritten as

$$\frac{1}{r^2\sin^2\theta}\frac{1}{\mu^r{}_r}\frac{\partial}{\partial\theta}\frac{\partial}{\partial\phi}(\sin\theta E^\phi) - \frac{1}{r^2\sin^2\theta}\frac{1}{\mu^r{}_r}\frac{\partial^2 E^\theta}{\partial\phi^2} - \frac{1}{r}\frac{\partial}{\partial r}\left(\frac{1}{\mu^\phi{}_\phi}\frac{\partial}{\partial r}(rE^\theta)\right) = k_0^2\epsilon^\theta{}_\theta E^\theta. \tag{A.14}$$

We introduce $\nabla\cdot\mathbf{D} = 0$, yielding

$$\frac{\partial}{\partial\theta}(\sin\theta E^\theta) = -\frac{\partial E^\phi}{\partial\phi}. \tag{A.15}$$

When we insert this equation in Eq. (A.14), we can eliminate E^ϕ and find

$$-\frac{1}{r^2\sin^2\theta}\frac{1}{\mu^r{}_r}\frac{\partial}{\partial\theta}\left(\sin\theta\frac{\partial}{\partial\theta}(\sin\theta E^\theta)\right) - \frac{1}{r^2\sin^2\theta}\frac{1}{\mu^r{}_r}\frac{\partial^2 E^\theta}{\partial\phi^2} - \frac{1}{r}\frac{\partial}{\partial r}\left(\frac{1}{\mu^\phi{}_\phi}\frac{\partial}{\partial r}(rE^\theta)\right) = k_0^2\epsilon^\theta{}_\theta E^\theta. \tag{A.16}$$

It is important to notice that this last equation is valid for every coordinate transformation as defined by Eq. (A.1). By introducing the new variable $E^{s\theta} = \sin\theta E^\theta$, this equation can be transformed to a more familiar one:

$$\frac{1}{r}\frac{\partial}{\partial r}\left(\frac{1}{\mu^\phi{}_\phi}\frac{\partial}{\partial r}(rE^{s\theta})\right) + \frac{1}{r^2\sin\theta}\frac{1}{\mu^r{}_r}\frac{\partial}{\partial\theta}\left(\sin\theta\frac{\partial}{\partial\theta}(E^{s\theta})\right) + \frac{1}{r^2\sin^2\theta}\frac{1}{\mu^r{}_r}\frac{\partial^2 E^{s\theta}}{\partial\phi^2} + k_0^2\epsilon^\theta{}_\theta E^{s\theta} = 0. \tag{A.17}$$

If ϵ and μ are isotropic and homogeneous, equation (A.17) simply tells us that

$$E^{s\theta} = [Aj_l(kr) + By_l(kr)]Y_{lm}(\theta,\phi), \tag{A.18}$$

where j_l and y_l are the spherical Bessel functions of the first and the second kind, respectively, and Y_{lm} are spherical harmonics. In the next step we will find similar solutions for the field inside the cloak, where ϵ and μ are given by (A.7),(A.8) and (A.9). By multiplying with $r^2\mu^r{}_r$, we can seperate the radial from the angular part of the equation

$$r\mu^r{}_r\frac{\partial}{\partial r}\left(\frac{1}{\mu^\phi{}_\phi}\frac{\partial}{\partial r}(rE^{s\theta})\right) + \frac{1}{\sin\theta}\frac{\partial}{\partial\theta}\left(\sin\theta\frac{\partial}{\partial\theta}(E^{s\theta})\right) + \frac{1}{\sin^2\theta}\frac{\partial^2 E^{s\theta}}{\partial\phi^2} + r^2\mu^r{}_r k_0^2\epsilon^\theta{}_\theta E^{s\theta} = 0. \tag{A.19}$$

Let us write $E^{s\theta}(r,\phi,\theta) = R^{s\theta}(r)\Psi^{s\theta}(\phi,\theta)$. Inside the metamaterial-shell, the angular equation for $\Psi^{s\theta}$ will result in spherical harmonics: $Y_{lm}(\theta,\phi)$. Taking this into account, the radial equation becomes:

$$r\mu^r{}_r\frac{\partial}{\partial r}\left(\frac{1}{\mu^\phi{}_\phi}\frac{\partial}{\partial r}(rR^{s\theta})\right) + \left(r^2\mu^r{}_r k_0^2\epsilon^\theta{}_\theta - l(l+1)\right)R^{s\theta} = 0. \tag{A.20}$$

Now let us introduce $r' = f(r)$, as defined in Eq. (A.1). Eq. (A.20) then transforms into:

$$\frac{r'^2}{r}\frac{\partial^2}{\partial r'^2}(rR^{s\theta}) + \left(k_0^2 r'^2 - l(l+1)\right)R^{s\theta} = 0. \tag{A.21}$$

We now define a second new variable

$$R^{fs\theta} = \frac{r}{r'}R^{s\theta}. \tag{A.22}$$

When we finally insert this new variable into equation (A.21), we derive that

$$r' \frac{\partial^2}{\partial r'^2}(r' R^{fs\theta}) + \left(k_0^2 r'^2 - l(l+1)\right) R^{fs\theta} = 0. \tag{A.23}$$

We can thus conclude that inside the shell $R^{fs\theta}$ is a linear combination of Bessel functions, or

$$E^{s\theta} = \frac{f(r)}{r}[A j_l(k_0 f(r)) + B y_l(k_0 f(r))]Y_{lm}(\theta, \phi). \tag{A.24}$$

A.3 The Perfect Spherical Cavity

Equation (A.24) gives us an expression for one—modified—component of the electric field inside the shell, (A.18) does the same for the free space electric fields (inside and outside the cavity). We can derive the modes of this system by expressing the proper boundary conditions:

$$\Delta E_t = 0, \tag{A.25}$$
$$\Delta H_t = 0, \tag{A.26}$$
$$\Delta D_n = 0, \tag{A.27}$$
$$\Delta B_n = 0. \tag{A.28}$$

Conditions (A.27) and (A.28) do not offer any information, since $D_n = 0$ and the radial dependency of E^θ equals the radial dependency of E^ϕ (equation(A.15)). For the same reason, it is apparent that (A.25) is guaranteed if $\Delta E^{s\theta} = 0$. Furthermore, it can be seen from (A.12) that (A.26) implies $\Delta H^\phi = 0$. Therefore, let us start by expliciting H^ϕ. In this calculations we will use the abbreviation $A j_l(k_0 f(r)) + B y_l(k_0 f(r)) = B_l(k_0 f(r))$:

$$H^\phi = \frac{1}{\mu_0 \mu^\phi{}_\phi} \frac{1}{i\omega} \frac{1}{r} \frac{\partial}{\partial r}(rE^\theta), \tag{A.29}$$

$$H^\phi = \frac{1}{\sin\theta} \frac{1}{\mu_0} \frac{1}{i\omega} \left[\frac{1}{r} B_l(k_0 f(r)) + \frac{k_0 f(r)}{r} B_l'(k_0 f(r))\right] Y_{lm}(\theta, \phi), \tag{A.30}$$

where the prime (′) denotes a differentiation with respect to the radial coordinate r. Using this equation, in combination with (A.24), we can conclude that inside the cavity, we get:

$$E^{s\theta} = A j_l(k_0 r) Y_{lm}(\theta, \phi), \tag{A.31}$$

$$H^\phi = \frac{1}{\sin\theta} \frac{1}{\mu_0} \frac{1}{i\omega} \left[\frac{1}{r} A j_l(k_0 r) + A k_0 j_l'(k_0 r)\right] Y_{lm}(\theta, \phi). \tag{A.32}$$

Inside the metamaterial-shell:

$$E^{s\theta} = \frac{f(r)}{r} \left[B j_l(k_0 f(r)) + C y_l(k_0 f(r))\right] Y_{lm}(\theta, \phi), \tag{A.33}$$

$$H^\phi = \frac{1}{\sin\theta} \frac{1}{\mu_0} \frac{1}{i\omega} \left\{\frac{1}{r} \left[B j_l(k_0 f(r)) + C y_l(k_0 f(r))\right] + \frac{k_0 f(r)}{r} \left[B j_l'(k_0 f(r)) + C y_l'(k_0 f(r))\right]\right\} Y_{lm}(\theta, \phi). \tag{A.34}$$

Outside the cavity:

$$E^{s\theta} = Dh_l(k_0 r)Y_{lm}(\theta, \phi), \tag{A.35}$$

$$H^{\phi} = \frac{1}{\sin\theta}\frac{1}{\mu_0}\frac{1}{i\omega}\left[\frac{1}{r}Dh_l(k_0 r) + Dk_0 h_l'(k_0 r)\right]Y_{lm}(\theta, \phi). \tag{A.36}$$

We are now ready to determine the explicit form of the remaining boundary conditions (A.25) and (A.26).

$$Aj_l(k_0 R_1) = \frac{f(R_1)}{R_1}[Bj_l(k_0 f(R_1)) + Cy_l(k_0 f(R_1))], \tag{A.37}$$

$$\frac{1}{R_1}Aj_l(k_0 R_1) + Ak_0 j_l''(k_0 R_1) = \frac{1}{R_1}[Bj_l(k_0 f(R_1)) + Cy_l(k_0 f(R_1))] + \frac{k_0 f(R_1)}{R_1}[Bj_l'(k_0 f(R_1)) + Cy_l'(k_0 f(R_1))], \tag{A.38}$$

$$\frac{f(R_2)}{R_2}[Bj_l(k_0 f(R_2)) + Cy_l(k_0 f(R_2))] = Dh_l(k_0 R_2), \tag{A.39}$$

$$\frac{1}{R_2}[Bj_l(k_0 f(R_2)) + Cy_l(k_0 f(R_2))] + \frac{k_0 f(R_2)}{R_2}[Bj_l'(k_0 f(R_2)) + Cy_l'(k_0 f(R_2))] = \frac{1}{R_2}Dh_l(k_0 R_2) + Dk_0 h_l'(k_0 R_2). \tag{A.40}$$

We can rewrite this set to:

$$Aj_l(k_0 R_1) = Bj_l(k_0 f(R_1)) + Cy_l(k_0 f(R_1)), \tag{A.41}$$

$$Ak_0 j_l'(k_0 R_1) = Bk_0 j_l'(k_0 f(R_1)) + Ck_0 y_l'(k_0 f(R_1)), \tag{A.42}$$

$$B\frac{f(R_2)}{R_2}j_l(f(R_2)) + C\frac{f(R_2)}{R_2}y_l(f(R_2)) = Dh_l(k_0 R_2), \tag{A.43}$$

$$B[\frac{1}{R_2}j_l(f(R_2)) + \frac{f(R_2)}{R_2}j_l'(f(R_2))] + C[\frac{1}{R_2}y_l(k_0 f(R_2)) + \frac{f(R_2)}{R_2}y_l'(f(R_2))] = D[\frac{1}{R_2}h_l(k_0 R_2) + k_0 h_l'(k_0 R_2)]. \tag{A.44}$$

We know that, independent of l, $f(R_2)j_l(f(R2)) = 0$. If $l \neq 0$, we know that $f(R_2)y_l(f(R_2)) = -\infty$, $j_l(f(R_2)) + f(R_2)j_l'(f(R2)) = 0$, and $y_l(f(R_2)) + f(R_2)y_l'(f(R_2)) = +\infty$. When we consider the solutions for which $l \neq 0$, we find:

$$Aj_l(k_0 R_1) = Bj_l(k_0 R_1) + Cy_l(k_0 R_1), \tag{A.45}$$

$$Ak_0 j_l'(k_0 R_1) = Bk_0 j_l'(k_0 R_1) + Ck_0 y_l'(k_0 R_1), \tag{A.46}$$

$$B \times 0 + C \times (-\infty) = Dh_l(k_0 R_2), \tag{A.47}$$

$$B \times 0 + C \times (+\infty) = D[\frac{1}{R_2}h_l(k_0 R_2) + k_0 h_l'(R_2)]. \tag{A.48}$$

We are looking for the solutions for which $C = 0$ and find that

$$Aj_l(k_0 R_1) = Bj_l(k_0 R_1), \tag{A.49}$$

$$Aj_l'(k_0 R_1) = Bj_l'(k_0 R_1). \tag{A.50}$$

This means that there is no constraint on k_0 and thus permits a continuum of solutions. When we additionally express the conservation of energy, we find that $k_0 \in \mathbb{R}$, implying an infinite quality factor.

APPENDIX B

Simulations Modified Cavity

In this Appendix, we compare the modes of the perfect 'modified' cavity of the Mathematica simulations with the results obtained using the finite element simulation program Comsol Multiphysics.

B.1 Comsol Simulations

In the Comsol simulations, we define a finite simulation domain, in which we introduce the cylindrical, modified cavity with parameters given by Fig. B.2. Such a setup is shown in Fig. B.1. The simulation domain thus contains three regions. A vacuum region inside the cavity, the cavity region, specified by an anisotropic permittivity and permeability, and a third region that corresponds to the surrounding vacuum. In this setup, we also have to define the boundary conditions at the interface between two regions. At the inner boundaries we impose the continuity condition, and at the outer rim, which limits the simulation domain, we apply a scattering boundary condition for cylindrical waves. This condition gives the best results when we are searching for the confined modes of a radiating cavity. Finally, we also define the mesh of the simulation, whose elements should be much smaller than the wavelength under consideration. There is, however, an upper limit in the number of mesh elements due to the finite processing power. The best results are obtained when the number of mesh elements is much bigger at the interfaces between two regions.
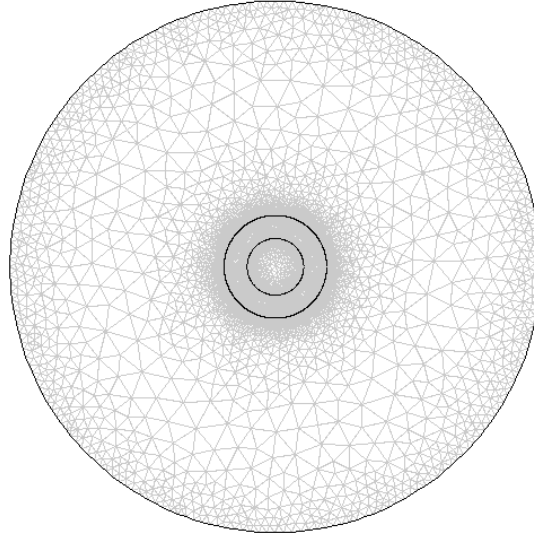
Figure B.1: The setup of the simulations.

B.2 Results

Below, we have listed three examples of confined modes within the modified cavity.

In the left column, we plot the solutions of our calculations in Mathematica. In these calculations, we have used the parameters: $R_1 = 3, R_2 = 6, \Delta R_1 = 0.2, \Delta R_2 = 0.2$. The right column contains the corresponding Comsol results. Here, we have defined the parameters $R_1 = 3 \cdot 10^{-4}, R_2 = 6 \cdot 10^{-4}$, $\Delta R_1 = 0.2 \cdot 10^{-4}, \Delta R_2 = 0.2 \cdot 10^{-4}$. Furthermore, Comsol returns the angular frequency ω_0, while we calculate $k_0 = \omega_0/c$ in Mathematica. The solutions of Comsol and Mathematica should thus be proportional by a factor $3.00 \cdot 10^{12}$.
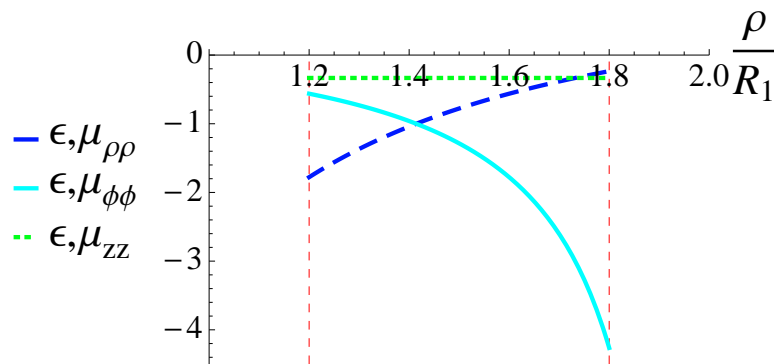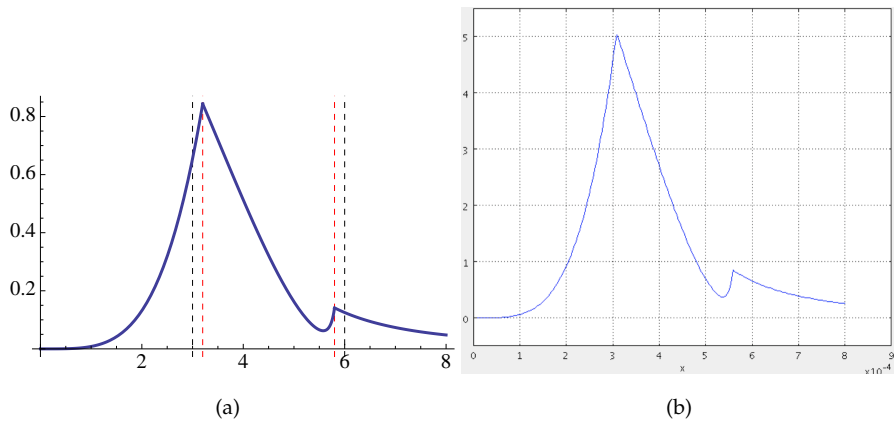

Figure B.2: Material parameters of the cavity under consideration. We notice that every component is negative, bounded between -0.333 and -4.263.
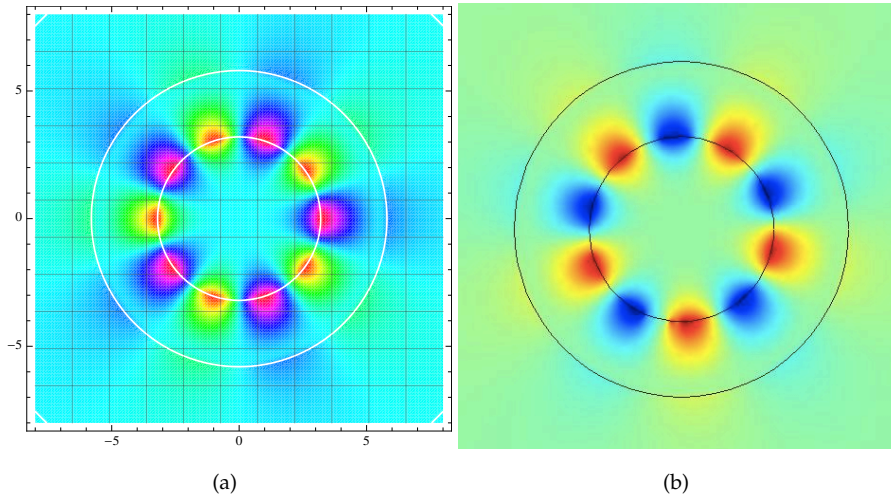
(a)

(b)
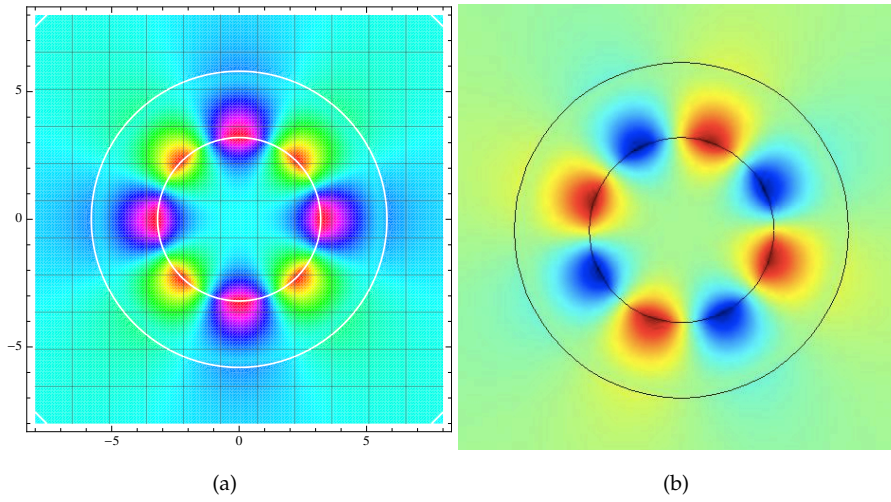
Figure B.3: Comparison of the mode with angular mode number $m = 4$. (a) Mathematica simulation having a solution $k_0 = 2.57 \cdot 10^{-1} - 1.72 \cdot 10^{-3} \, i$, (b) Comsol simulation finding a solution at $\omega_0 = 7.70 \cdot 10^{11} - 6.08 \cdot 10^{9} \, i$.
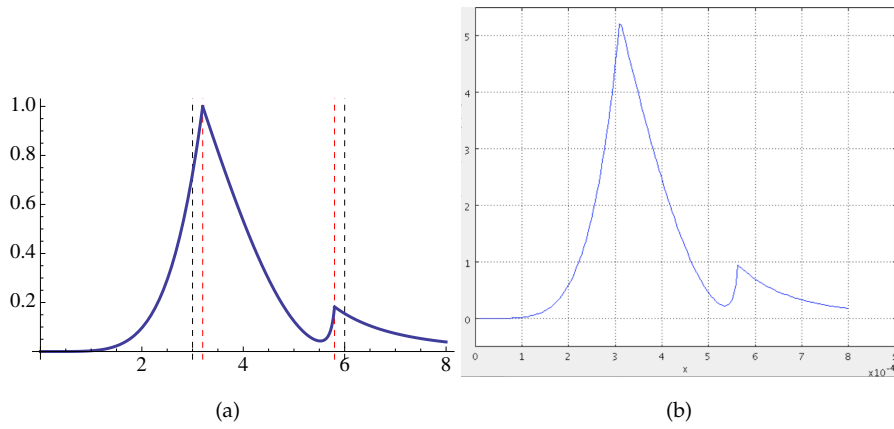

(a)

(b)

Figure B.4: The radial field distribution of the electric field E^z corresponding to the solutions shown in Fig. B.3.
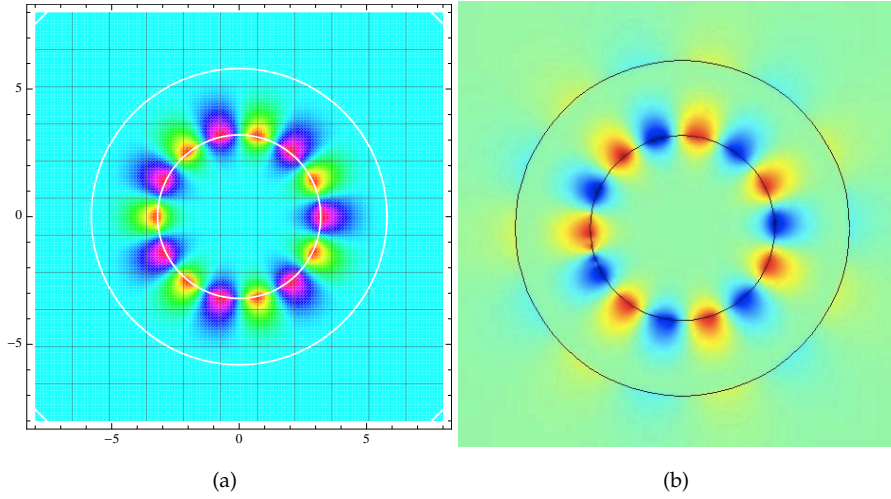
(a)

(b)

Figure B.5: Comparison of the mode with angular mode number $m = 5$. (a) Mathematica simulation having a solution $k_0 = 1.83 \cdot 10^{-1} - 5.37 \cdot 10^{-6}\,i$, (b) Comsol simulation finding a solution at $\omega_0 = 5.48 \cdot 10^{11} - 1.55 \cdot 10^{7}\,i$.
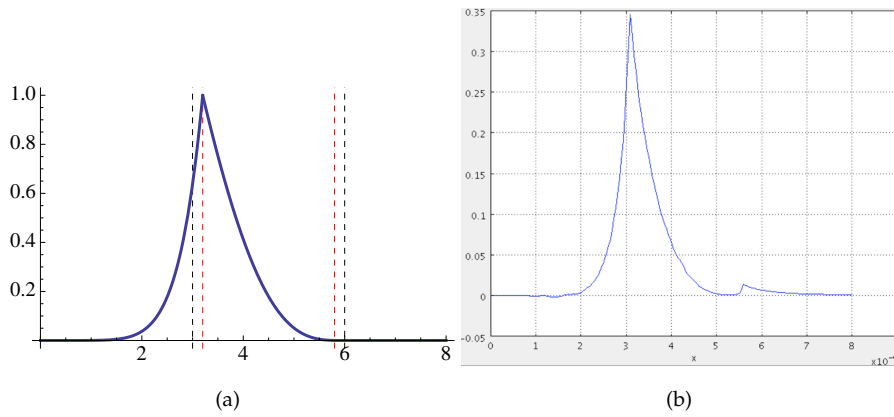

(a)

(b)

Figure B.6: The radial field distribution of the electric field E^z corresponding to the solutions shown in Fig. B.5.

(a)
(b)

Figure B.7: Comparison of the mode with angular mode number $m = 7$. (a) Mathematica simulation having a solution $k_0 = 7.83 \cdot 10^{-2} - 1.34 \cdot 10^{-14}$ i , (b) Comsol simulation finding a solution at $\omega_0 = 2.21 \cdot 10^{11} - 4.24 \cdot 10^3$ i.

(a)
(b)

Figure B.8: The radial field distribution of the electric field E^z corresponding to the solutions shown in Fig. B.8.

B.3 Discussion

The real parts of the mode solutions correspond very well:

$$\frac{7.70 \cdot 10^{11}}{2.57 \cdot 10^{-1}} = 3.00 \cdot 10^{12}, \tag{B.1}$$

$$\frac{5.48 \cdot 10^{11}}{1.83 \cdot 10^{-1}} = 3.04 \cdot 10^{12}, \tag{B.2}$$

$$\frac{2.21 \cdot 10^{11}}{7.83 \cdot 10^{-2}} = 2.82 \cdot 10^{12}. \tag{B.3}$$

The agreement between the imaginary parts is given by

$$\frac{6.08 \cdot 10^{9}}{1.72 \cdot 10^{-3}} = 3.53 \cdot 10^{12}, \tag{B.4}$$

$$\frac{1.55 \cdot 10^{7}}{5.37 \cdot 10^{-6}} = 2.89 \cdot 10^{12}, \tag{B.5}$$

$$\frac{4.24 \cdot 10^{3}}{1.34 \cdot 10^{-14}} = 3.16 \cdot 10^{17}. \tag{B.6}$$

The correspondence is not very good for the last solution, which has a very high quality factor. This could indicate the higher sensitivity of the very high Q modes with respect to perturbations, such as the introduction of a finite mesh in the numerical simulations.